ARMY RESEARCH LABORATORY

Final Report (2001-2006)

**U.S. Army Research Laboratory
Material Center of Excellence**

**Advanced Metals and Ceramics for Armor and Anti-Armor
Applications**

**High-Fidelity Design and Processing of Advanced Armor
Ceramics**

by D. E. Niesz and J. W. McCauley

ARL-CR-594 **June 2007**

prepared by

D. E. Niesz
Recipient Program Manager
Rutgers, The State University of New Jersey
Piscataway, NJ 08854-8065

J. W. McCauley
Cooperative Agreement Manager
Senior Research Engineer (ST) Ceramic Materials
Weapons and Materials Research Directorate
U.S. Army Research Laboratory
Aberdeen Proving Ground, MD 21005-5066

NOTICES

Disclaimers

The findings in this report are not to be construed as an official Department of the Army position unless so designated by other authorized documents.

Citation of manufacturer's or trade names does not constitute an official endorsement or approval of the use thereof.

Destroy this report when it is no longer needed. Do not return it to the originator.

Army Research Laboratory
Aberdeen Proving Ground, MD 21005-5066

ARL-CR-594   June 2007

Final Report (2001-2006)

U.S. Army Research Laboratory
Material Center of Excellence

Advanced Metals and Ceramics for Armor and Anti-Armor Applications

High-Fidelity Design and Processing of Advanced Armor Ceramics

D. E. Niesz
Rutgers, The State University of New Jersey

J. W. McCauley
Weapons and Materials Research Directorate, ARL

prepared by

D. E. Niesz
Recipient Program Manager
Rutgers, The State University of New Jersey
Piscataway, NJ 08854-8065

J. W. McCauley
Cooperative Agreement Manager
Senior Research Engineer (ST) Ceramic Materials
Weapons and Materials Research Directorate
U.S. Army Research Laboratory
Aberdeen Proving Ground, MD 21005-5066

under contract

DAAD19-01-2-0004

REPORT DOCUMENTATION PAGE

Form Approved
OMB No. 0704-0188

1. REPORT DATE *(DD-MM-YYYY)*	2. REPORT TYPE	3. DATES COVERED (From - To)
June 2007	Final	January 2001–December 2005

4. TITLE AND SUBTITLE

Final Report (2001-2006), U.S. Army Research Laboratory Material Center of Excellence, Advanced Metals and Ceramics for Armor and Anti-Armor Applications, High-Fidelity Design and Processing of Advanced Armor Ceramics

5a. CONTRACT NUMBER
DAAD19-01-2-0004

5b. GRANT NUMBER

5c. PROGRAM ELEMENT NUMBER

6. AUTHOR(S)
D. E. Niesz[*] and J. W. McCauley

5d. PROJECT NUMBER
BH64

5e. TASK NUMBER

5f. WORK UNIT NUMBER

7. PERFORMING ORGANIZATION NAME(S) AND ADDRESS(ES)

Rutgers
The State Univ. of New Jersey
607 Taylor Road
Piscataway, NJ 08854-8065

U.S. Army Research Laboratory
ATTN: AMSRD-ARL-WM
Aberdeen Proving Ground, MD
21005-5066

8. PERFORMING ORGANIZATION REPORT NUMBER

9. SPONSORING/MONITORING AGENCY NAME(S) AND ADDRESS(ES)

U.S. Army Research Laboratory
ATTN: AMSRD-ARL-WM
Aberdeen Proving Ground, MD 21005-5066

10. SPONSOR/MONITOR'S ACRONYM(S)
ARL-CR-594

11. SPONSOR/MONITOR'S REPORT NUMBER(S)

12. DISTRIBUTION/AVAILABILITY STATEMENT

Approved for public release; distribution is unlimited.

13. SUPPLEMENTARY NOTES

[*] Rutgers, The State University of New Jersey, Piscataway, NJ 08854-8065

14. ABSTRACT

This is the final summary report of a 5-year (2001–2005) collaborative research program on advanced metals and ceramics for armor and anti-armor applications carried out in the U.S. Army Research Laboratory Material Center of Excellence at Rutgers and Johns Hopkins Universities under a cooperative-agreement contractual relationship. The focus of this center is on high-fidelity design and processing of advanced armor ceramics. The overarching goal has been to develop an improved understanding of selected key areas of the materials and processing science of ceramic armor materials. The areas investigated were selected jointly by the participating organizations with significant input from the ceramic armor community through a ceramic armor working group (CAWG) that included over 20 industrial organizations. They were selected as the most relevant, unclassified basic-research areas for improving the scientific understanding of the materials and processing science critical to the ballistic performance of ceramic armor materials. Length scales from the atomic to the macro were included in the investigation. The areas that were selected for investigation included the following: (1) development of nanograin-size ceramic materials to investigate their response in ballistic impact, (2) investigation of high strain-rate behavior of ceramic armor materials, (3) investigation of designed macrostructures for shock-wave management, (4) statistical analysis of inclusions in silicon-carbide (SiC) armor ceramics, (5) micromechanical modeling of advanced armor ceramics—focus on plastic behavior of polycrystalline nanograined ceramics, (6) development of improved SiC microstructures through advanced powder processing, (7) nondestructive evaluation of ceramic armor, (8) investigation of the relation between quasi-static properties and ballistic performance, and (9) evaluation of the effect of grain texturing on the ballistic performance of B_4C. Areas 7, 8, and 9 were jointly funded by the CAWG.

15. SUBJECT TERMS

ceramics, armor, NDT, characterization, nanoceramics, defects

16. SECURITY CLASSIFICATION OF:			17. LIMITATION OF ABSTRACT	18. NUMBER OF PAGES	19a. NAME OF RESPONSIBLE PERSON
a. REPORT	**b. ABSTRACT**	**c. THIS PAGE**	UL	124	J. W. McCauley
UNCLASSIFIED	UNCLASSIFIED	UNCLASSIFIED			**19b. TELEPHONE NUMBER** *(Include area code)* 410-306-0711

Standard Form 298 (Rev. 8/98)
Prescribed by ANSI Std. Z39.18

Contents

List of Figures

List of Tables

Acknowledgments

1. Introduction

Armor ceramics are critical for weight reduction in current and future U.S. Army systems, including personnel protection. The realization of the full potential of armor ceramics requires a basic understanding of how the structure of armor-ceramic materials, at several length scales, affects the inherent ballistic performance and the variability of ballistic performance among nominally identical components. Key aspects of ceramic armor materials at the atomic, nano, micro, and macro scales that are significant to ceramic armor performance must be identified and understood. This report summarizes the key accomplishments of a 5-year cooperative research program to develop this fundamental understanding. The organizations involved in the cooperative research program were the Malcolm G. McLaren Center for Ceramic Research at Rutgers University, the Center for Advanced Metal and Ceramic Systems at Johns Hopkins University and the Weapons and Materials Directorate at the U.S. Army Research Laboratory (ARL).

Nine research areas were jointly selected for investigation by the participating organizations with significant input from the ceramic armor community through the ceramic armor working group (CAWG), established by the Malcolm G. McLaren Center for Ceramic Research in the Ceramic and Composite Material Center (CCMC), a National Science Foundation Multi-University Industry/University Cooperative Research Center. The research areas were selected as the most relevant unclassified basic-research areas for improving the scientific understanding of the materials and processing science critical to the ballistic performance of ceramic armor materials.

The nine research areas selected for investigation are:

- nanoceramics
- high strain-rate behavior and dynamic failure of armor ceramics
- designed macrostructures for shock-wave management
- statistical analysis of inclusions in silicon-carbide (SiC) armor ceramics
- micromechanical modeling of advanced armor ceramics: plastic behavior of polycrystalline nanograined ceramics
- silicon-carbide process improvements for improved homogeneity and reproducibility
- nondestructive evaluation (NDE) of ceramic armor
- relation of quasi-static properties to ballistic performance of armor ceramics
- directionally textured boron carbide by controlled-shear processing

The last three of the research areas were jointly funded by the CAWG through the CCMC. The key accomplishments of each research area are summarized in separate sections of this report, and the final section describes the Education and Outreach area of the program, including the CAWG.

1.1 Summary of Key Accomplishments

Research conducted under this cooperative agreement (CA) significantly enhanced the understanding of the role in ballistic performance of the structure of ceramic armor materials at the atomic, nano, micro, and macrolength scales. Alumina-spinel nanocomposite materials were developed using a novel fabrication process that is scalable and cost-effective. This material has exceptional hardness for an oxide material—2000 Vickers at a 2-kg load, which is well above the rule of mixtures hardness for the component oxides. In addition, a Kolsky-bar strength of 6.8 GPa was measured, although most samples measured to date have shown strengths of 5.3–5.8 GPa. This material also has excellent polishability and a scratch behavior far superior to ceramic armor materials with conventional microstructures. Remarkably, one sample exhibited a completely ductile scratch when scratched with a diamond stylus. A provisional patent has been filed on this technology, and the patent was licensed to a company that is funding scale-up work to fabricate tiles for ballistic testing. This testing should provide information on whether nanocomposite ceramics have improved ballistic performance as a result of true plastic deformation under the triaxial compression of a ballistic impact.

The microstructural defects in silicon carbon nitride (SiC-N) were quantitatively evaluated for a "good" and a "bad" V-50 target by examining fragments removed from the targets after ballistic testing. Fracture surfaces were used for this evaluation in order to identify large, very low frequency defects that may play a role in the variability of ballistic performance. The fragments were examined with a field emission-scanning electron microscope and an optical microscope. The defect frequency was plotted against defect size, and the distribution curves were fitted to a distribution. The distribution function for the tails of the distribution curves provides a mathematical description of the defect distribution that can be used as input in advanced computer codes for modeling the effect of microstructural defects on the ballistic performance of ceramic armor materials.

Research on NDE of ceramic armor that is jointly funded by the current CA and the ceramic armor subgroup (CAS) in the CCMC demonstrated that high-frequency ultrasound has the potential for quickly providing the defect distribution in an armor tile on a nondestructive basis, and it can eliminate the need for time-consuming microscopic examination after destructive ballistic testing. This NDE research has also demonstrated that a frequency greater than 50 MHz is required to locate defects that were known to cause poor ballistic performance. Also, progress was made in establishing that the breadth of the frequency-of-occurrence vs. transmitted amplitude plot is a useful approach to determining the quality of a ceramic armor tile. This

information will provide the microstructural defect distributions needed for use in advanced computer codes for evaluating the role of defects in ballistic performance.

Research on the current CA also developed SiC that was theoretically dense with a 2–3-µgr size. This was accomplished by working with a starting powder that was processed to remove all particles greater than 2 µm using colloidal filtration followed by wet-pressing to produce a green compact for hot pressing that was free of large pores. In addition, aqueous-based boron and carbon additives were made using a novel surfactant that gives perfect mixing, in stark contrast to the use of phenolic resin as the carbon additive and particulate B_4C as the boron additive. This SiC had higher hardness than SiC-N and is expected to give superior ballistic performance, much like Strassburger and Krell (*1*) showed for alumina. In future research, this material will be used to develop standards for ultrasonic inspection by incorporating known defects into the parent material.

Using phononic band-gap macrostructures, the ability to mitigate the elastic shock wave was demonstrated using WC/Co spheres in alumina materials.

Significant advancements were made in the modeling of dynamic failure in ceramic materials. The efforts focused on the discrete approach to cracking, e.g., cohesive elements, which represent cracks explicitly. Weibull-distributed cohesive strength models were developed to achieve faster numerical convergence and capture size effects. These models have naturally led to a shift of the modeling emphasis to the analysis of the stochastic response of ceramics and the influence of defects at the microstructural level on macroscopic mechanical properties (*2*). The improvements in the method's robustness enabled large-scale simulations of fragmentation. Fragmentation critically affects the mechanics of ballistic impact, and fragment size estimates are often used as input in codes to assess armor-ceramics performance. Numerical investigations focused on the statistics of fragmentation of ceramic materials, including dependence of fragment size distributions on strain rate, elastic and fracture properties, and defect distributions. The numerical results revealed notable differences from established analytical models, which do not take into account wave interactions arising in fragmentation events. In particular, simulations revealed that at high strain rates, smaller fragments than estimated with the Grady model (*3*) should be expected.

High-resolution electron-microscope observations of shock-loaded boron carbide have revealed the formation of nanoscale intragranular amorphous bands that occur parallel to specific crystallographic planes and contiguously with apparent cleaved fracture surfaces. This damage mechanism explains the measured, but not previously understood, decrease in the ballistic performance of boron carbide at high-impact velocities and pressures (*4*).

Techniques were developed to measure the dynamic strength of ceramics and to observe the dynamic failure process in situ. These techniques were applied to hot-pressed SiC (SiC-N) and B_4C, as well as to a number of sintered materials. The dynamic strength and dynamic fragmentation of a recently developed hot-pressed silicon carbide, SiC–N, was measured using a

modified Kolsky-bar technique together with an MTS servo-controlled hydraulic test machine. The effect of loading rate on the uniaxial compressive strength was measured and analyzed through the wing crack array approach. It was confirmed that the inertia effect is primarily responsible for the rate effect in the high loading rate regime, while subcritical crack growth dominates the effect of loading rate in the low strain-rate regime. High-speed photography was employed to observe and characterize in real-time the evolution of the failure mode and fragmentation during the test. Finally, quantitative analysis of the fragments was coupled with theoretical models to investigate the mechanism involved with fragmentation over loading rates from 10^{-4} to 10^3 MPa/μs.

Subsequently, these techniques were used to examine the dynamic failure process in transparent AlON. The dynamic activation, growth, and coalescence of cracks and the resulting damage zones from spatially separated internal defects were directly observed and correlated to the macroscopic loss of load-carrying capacity and ultimate catastrophic failure of transparent AlON specimens. The high-speed photographs of the coated (and hence opaque) AlON specimens showed the dynamic progressive failure on the specimen surface. This technique showed how a single failure mode appears to be dramatically different for the coated (opaque) and uncoated (transparent) specimens. Such fundamental studies of the dynamic failure process are key to developing an understanding of the complex phenomena involved in the ballistic event (5).

A very successful CAS was established. This group was set up within the CCMC with the following three purposes:

- To establish a forum for the ceramic armor community to hold workshops on topics selected by the member organizations as the most relevant for improving their mutual understanding of key issues in ceramic armor materials

- To conduct precompetitive research on ceramic armor materials that is selected by the member organizations as the most relevant research needed to improve the fundamental understanding of the relation of ceramic armor materials science to armor performance

- To provide a mechanism to distribute quickly the results of the CA to the ceramic armor community

This CAS grew to over 20 member organizations. Ten very productive workshops were held. In addition to the NDE and research discussed previously, the CAS supported three other projects. Under joint funding of the current CA and the CAS, research was conducted to identify quasi-static property measurements that provide initial screening that is relevant to ceramic armor performance. Another project investigated the effect of low levels of porosity and its associated pore distribution on armor performance. A fourth project investigated the fundamental reason for the poor ballistic performance of B_4C above a threshold impact pressure. Research in this project focused on investigating the amorphous planes that develop in B_4C above the threshold pressure as reported by Chen et al. (4). This research identified the B_4C polytype with C-C-C

chains as the probable cause of the threshold pressure, since this polytype has much lower activation energy for collapse into B_{12} and amorphous carbon than the polytype with C-B-C chains. While the C-C-C polytype becomes metastable at 7 GPa, the C-B-C polytypes do not become metastable until above 40 GPa. The C-C-C polytype is a minor polytype in hot-pressed B_4C, which points a direction for overcoming the poor performance of B_4C above the currently observed threshold pressure.

In addition, the CA linked ARL researchers with the researchers at Rutgers and Johns Hopkins. At Rutgers, three graduate students completed Ph.D.s with ARL researchers as outside thesis advisors. Four additional students are completing their Ph.D. studies with ARL researchers as thesis committee members for each of these students. This collaboration has extended to the CAS where the two graduate students currently working on ceramic-armor programs have ARL researchers on their thesis committees, and the two postdoctoral fellows have ARL scientists in their technical advisory groups. Twenty-nine publications (five joint with ARL researchers), one patent, and 44 presentations (10 joint with ARL researchers) resulted from this program. Six students have held summer internships at ARL, and Professor Niesz spent a 6-month sabbatical at ARL, further contributing to the joint collaboration.

1.2   References

1. Strassburger, E.; Krell, A. Paper PAC6-B-04-2001. Presented at Pac Rim 4, Maui, HI, 4–8 November 2001.

2. Zhou, F.; Molinari, J.-F. Three Dimensional Dynamic Crack Propagation Using Cohesive Elements: A Methodology to Address Mesh Dependency. *International Journal for Numerical Methods in Engineering* **2004**, *59* (1),1–24.

3. Zhou, F.; Molinari, J.-F.; Ramesh, K. T. A Cohesive-Model Based Fragmentation Analysis: Effects of Strain Rate and Initial Defects Distribution. *Int. Journal of Solids and Structures* **2005**, *42* (18–19), 5181–5207.

4. Chen, W.; McCauley, J. W.; Hemker, K. J. Shock-Induced Localized Amorphization in Boron Carbide. *Science* **2003**, *299*, 1563.

5. Paliwal, B.; Ramesh, K. T.; McCauley, J. W. Direct Observation of the Dynamic Compressive Failure of a Transparent Polycrystalline Ceramic (AlON). *J. Am. Ceram. Soc.* **2006**, *89* (7), 2128–2133.

2. Nanoceramics

Core Faculty: B. Kear, D. Niesz, V. Greenhut

ARL Collaborators: J. McCauley, J. Adams, G. Gilde

Research Associates: R. Sadangi, V. Shukla

Graduate Student/Postdoctoral Associate: B. McEnerney

2.1 Objectives

- Characterize the behavior of nanoceramics in ballistic impact

- Demonstrate nanoceramic fabrication techniques that are scalable and cost-effective

2.2 Key Accomplishments

- Demonstrated a new paradigm in ceramic fabrication technology that is a cost-effective process for obtaining fully dense micro/nanograin-size composites of $Al_2O_3/MgAl_2O_4$

- Achieved a Vickers hardness of 2000 at 19.6 N for alumina 60 volume-percent spinel

- Demonstrated high strain-rate strength (Kolsky bar) of 4.7–6.1 GPa

2.3 Introduction

Significant research has been conducted to develop fully dense ceramic materials for armor applications, since porosity has been shown to reduce ballistic performance. The effect of grain size on the strength and hardness of ceramics materials in static and quasi-static testing has also been known since the early 1950s (*1–4*). Most current, commercial armor ceramics sacrifice finer grain size to minimize porosity, resulting in grain sizes significantly larger than 1 μm. Because of this processing constraint, very little progress has been made towards fabricating fully dense ceramic materials with nanometer-sized grains for armor applications, even though available data suggest that such materials could show a significant improvement in the ballistic performance. Furthermore, empirical indications show that a highly favorable ballistic response regime may exist for ceramics with fine grain sizes. The Hall-Petch (*1, 2*) relation predicts increasing strength and hardness with decreasing grain size, and nanoscale structures also exhibit an increasing tendency towards localized, effective plasticity with decreasing grain size, which could improve dwell and result in improved ballistic performance (*5*). Therefore, nanometer grain size—a potentially important parameter for improving the performance of armor ceramics—needs further study.

This research was undertaken to investigate whether armor ceramics with nanometer grain size would exhibit limited plastic deformation under the confined compression experienced in a ballistic impact. In earlier work at Lawrence Livermore National Laboratories in the 1970s, several materials that could potentially exhibit limited plastic deformation in ballistic impact showed better ballistic performance than expected, based on their hardness, density, and elastic modulus (*6*). Furthermore, several nanograin-size ceramics have reportedly shown ductile scratch behavior (*7*). Therefore, the question of whether nanograin-size armor ceramics could also exhibit limited plastic deformation in ballistic impact was investigated. The research focused on determining the fabricability, hardness, structure, and high strain-rate behavior of Al_2O_3-$MgAl_2O_4$ composites. This materials system was selected based on its low areal density, high hardness and high elastic modulus, and for its low melting and fabrication temperatures compared to other armor ceramics. In addition, only materials that do not require atmospheric control during plasma melting could be considered, because of the lack of atmospheric control in the plasma-melting system available when the research was initiated.

2.4 Approach

The materials were fabricated by commercially available, scalable processing technologies using a new paradigm in ceramic processing. This new paradigm is based on forming a metastable powder by plasma melting to form a supersaturated solid solution of alumina and spinel that decomposes during densification by hot isostatic pressing (HIP) into the alumina and spinel equilibrium phases. The two phases mutually inhibit grain growth, which provides a larger time-temperature window for densification while maintaining a nanograin size in each phase. This processing technology enables dense, nanograin-size materials to be fabricated without the difficulty of producing and processing nanoparticle-size powders.

2.5 Procedure

The starting powders were Baikowski-Malakoff RC SPT-DBM 99.9% purity submicrometer aluminum oxide and Baikowski Baikalox S30CR 99.9% submicrometer magnesium aluminate. These powders were selected based upon particle size and purity. High-purity grades of powders were used to minimize potential complications from impurities. Certain contaminants, such as sodium and calcium, can cause the formation of undesired phases, such as β-Al_2O_3 (Na_2O-$11Al_2O_3$) and calcium hexaluminate (CaO-$6Al_2O_3$), which could significantly reduce the ballistic performance. Small particle sizes were selected to eliminate the need for particle size reduction to achieve the desired scale of mixing.

Spray-drying was used to produce the feedstock for plasma melting. Spray-drying had been previously demonstrated as an effective technique, since a significant portion of the granules were in the 38–53-μm size fraction, which Zhou (*8*) found to be optimal for complete melt homogenization of Al_2O_3–ZrO_2. The granules were subsequently heat-treated at 1400 °C for 3 hr to provide a bisque sinter to improve the strength of the granules, so that they would survive

7

the turbulent plasma-melting process without granule-granule bonding. The granules were then sieved to obtain the size fraction desired for plasma melting.

Spray-dried and heat-treated granules were effectively melted in the 38–53-μm size fraction using a Sulzer-Metco 9 MB DC-Arc plasma torch using an Ar-10% H_2 gas. Two passes were required to ensure complete melt homogenization, as it was determined that the first pass primarily densified the granules, and the second pass resulted in complete homogenization, as confirmed by x-ray diffraction. Granules greater than 53 μm could not be completely melted using this system.

The powders were collected using a deionized water bath. Based upon previous work by Zhou (*8*), the torch was positioned within 22 cm of the water bath, to ensure that the rapid quenching would take place within the water. It was also important to maintain a minimum distance from the water, as the turbulent flow of the plasma would result in increased levels of water and powder loss, thus reducing efficiency. The powders were subsequently dried at 100 °C.

The plasma-melted powders were transparent spheres that were a single metastable phase, with varying degrees of segregation. Initial studies resulted in melted spheres with significant segregation, as the surface structures were dendritic. Process improvements resulted in structures that either exhibited cellular or planar segregation or remained featureless. Typically, only the finest fraction of powders were featureless.

The powders were subsequently attrition-milled in a high-purity aluminum oxide bowl, using high-purity (99.9%) 3-mm Al_2O_3 milling media. Ethyl alcohol was found to be an acceptable fluid medium, as it did not react with the powder and left minimal residual carbon upon drying. Water was found to be an undesirable fluid media; some of the magnesium ions would go into solution during milling and during the drying process would form a hydrated phase that acted as a cement, creating hard agglomerates. Ball milling in a high-density polyethylene jugs was also found to be an efficient process and would likely be used for scale-up research. The milling processes resulted in powders with average particle sizes between 1–2 μm.

The green powders were uniaxially pressed in 2.54-cm-diameter stainless steel dies. No binder was used. The pressing pressures were nominally 20 MPa. Subsequent cold isostatic pressing at 260 MPa was necessary to achieve green densities between 55%–65% of theoretical green. Density measurements were somewhat complicated, as the density of the metastable phase significantly varied from that of the stable composition. Helium pycnometry was necessary to determine the true density of the metastable powders.

The fine powders showed a significant hydrophilic behavior, and as such, post-green-pressing heat treatment was required. This was performed at 1100 °C for 3 hr, which was sufficient to eliminate hydrated phases but was a low enough temperature to prevent the onset of transformation to the stable phases. Insufficient degassing resulted in spherical porosity within

the samples and incomplete densification. The heat treatment was performed in either argon and vacuum, which gave comparable results.

The samples were densified using HIP and were canned in AISI 1018 mild steel or niobium, although the latter was deemed too expensive and was only used in initial work. The steel cans were coated with an aerosolized boron nitride spray prior to the samples being loaded and were then backfilled with argon until they were degassed and sealed.

Upon the completion of HIP, the samples were extracted from the cans, using a hydrochloric acid and nitric acid bath to chemically remove the cans without damaging the samples. The samples were then sectioned using a diamond wafering blade. Thermal etching of the samples was a difficult task, as there was a great propensity for surface growth. Typical conditions commonly discussed in the literature were ineffective and resulted in uncontrolled surface growth, which effectively concealed the true structure of the samples. The acceptable etching conditions were zero hold at 200–250 °C below the HIP temperature. This resulted in minimal surface growth that allowed for more accurate evaluation of the microstructure.

The density, hardness, and microstructures were examined using several techniques. The high strain-rate behavior was determined using split-Hopkinson pressure bar (SHPB) testing. The grindability of the materials was measured using a technique developed by the Chand Khar Corporation and the U.S. National Institute of Standards and Technology (NIST). The crystallographic structure was determined using x-ray diffraction.

2.6 Preliminary Processing Results

Initial research was conducted concurrently on Al_2O_3–AlON and AlN–TiB_2. It was not feasible to achieve complete plasma melting for either system, and it was further concluded that controlled-atmosphere processing was required to maintain the appropriate stoichiometry. These results and the lack of a high-enthalpy, controlled-atmosphere plasma torch resulted in the selection of the Al_2O_3-Al_2MgO_4 system for further study.

The following two initial densification techniques were evaluated: high-pressure hot pressing and uniaxial hot pressing. The high-pressure hot pressing technique utilized two dies, 3- and 50-mm diameter. Pressures between 1 and 10 GPa with temperatures up to 1800 °C were used for the 3-mm dies, and pressures of 100–1000 MPa and temperatures up to 1400 °C were used for the 50-mm dies. A pseudo-isostatic state was created using deformable toroidal rings of lava stone encasing a graphite sheath. Initial work demonstrated the possibility of densification using the small die; however, the larger die suffered from frictional problems that were never satisfactorily overcome, resulting in incomplete densification. This technique was ineffective and cost-inefficient and was thus abandoned.

Uniaxial hot pressing, which uses lower pressures than high-pressure hot pressing or HIP, was also evaluated. Graphite dies with a 50-mm diameter were fabricated, and samples were pressed at pressures of 15–30 MPa and temperatures of 1400–1600 °C. Densities of 90%–95% of

9

theoretical values were achieved, but the temperatures resulted in unacceptable grain growth. It was determined that the pressures were not sufficient to achieve complete densification at temperatures below 1400 °C, so hot uniaxial pressing was discontinued, and all further densification was done by HIP.

2.7 Accomplishments

Fully dense samples with submicrometer to nanometer scale features were produced using HIP at 207 MPa with temperatures ≤1400 °C. The HIP cycles were designed based upon pressureless time-temperature-transformation studies. The results indicated that complete transformation from metastable to stable occurred after 30 min at 1300 °C, 60 min at 1275 °C, and over 90 min at 1250 °C. Holds in excess of 120 min did not result in complete transformation at 1200 °C; however, 1200 °C was too low for complete densification of the material by HIP. These data resulted in the cycle design to incorporate rapid heating to 1000 °C, where full pressure was applied, followed by slowly heating (100 °C/hr) through the transformation temperature range, to minimize the possibility of uncontrolled transformation.

The microstructure of the samples varied with processing conditions. The samples that underwent HIP at 1260, 1310, and 1350 °C exhibited similar microstructures when viewed using a scanning electron microscope (figure 1). Thermal etching revealed the clear presence of the prior grain boundaries of the supersaturated cubic phase. However, closer examination revealed that each prior grain of the metastable supersaturated phase contained a mixture of the stable hexagonal Al_2O_3 and cubic $MgAl_2O_4$. The hold time and high temperature of the 1400 °C HIP cycle resulted in significant long-range diffusion. The aluminum oxide and magnesium aluminate phases segregated to the scale of the prior grains (~2 μm) in a bicontinuous three-dimensional (3-D) network, as shown in figure 1. Control samples, fabricated by pressureless sintering at 1600 °C for 3 hr and then post-HIP at 1375 °C, were also examined. There was significant grain growth in these samples, and thermal etching revealed that the two phases had completely segregated into the individual grains during processing.

(a)   (b)
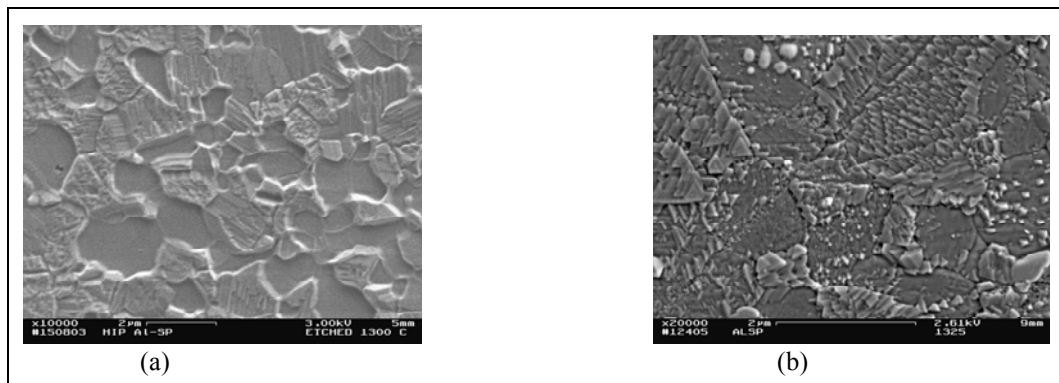
Figure 1. Al_2O_3–40 volume-percent $MgAl_2O_4$ that underwent HIP at (a) 1400 °C and (b) 1310 °C.

All the HIP temperatures evaluated resulted in complete transformation from the metastable to the stable phases, and no evidence of amorphous material was found. The grain boundaries between the aluminum oxide and the magnesium aluminate were also found to be low-angle grain boundaries with no evidence of extraneous phases or porosity. Some very limited amounts of nanopores were detected along the prior grain boundary interfaces of rubble that had been subjected to SHPB testing.

Vickers hardness testing revealed that the control samples had the lowest hardness, which was comparable to the rule of mixtures. Hardness was found to improve with decreasing HIP temperature. The only exceptions found were for the Al_2O_3–60 volume-percent $MgAl_2O_4$ samples that underwent HIP at 1260 and 1310 °C, which had minor amounts (less than 1%) of retained porosity, which was likely caused by incomplete removal of hydrate material during heat treatment. However, the lower hardness values were primarily observed in the 1- and 2-kg tests, as those indents had the largest area tested and were statistically more likely to encounter pores.

The overall hardness was expected to trend with the aluminum oxide content, as the hardness for aluminum oxide is normally reported as 400–500 HV harder than magnesium aluminate. However, the Al_2O_3–20 volume-percent $MgAl_2O_4$ samples exhibited the lowest overall hardness, and their hardnesses were not significantly better than the rule of mixtures. The Al_2O_3–40 volume-percent $MgAl_2O_4$ samples exhibited the best hardness—2000 HV at a load of 19.6 N, as shown in figure 2. The Al_2O_3–60 volume-percent $MgAl_2O_4$ samples had comparable hardness, except that the hardness values of the 1260 and 1310 °C HIP runs were skewed by residual porosity. The structure of the Al_2O_3–20 volume-percent $MgAl_2O_4$ samples indicated that the magnesium aluminate content was insufficient to provide a true fine-scale, bimodal microstructure, so that the final structure was a matrix of aluminum oxide with inclusions of spinel grains. As the scale of mixing for this structure was on the micrometer scale, rather than the nanometer scale, there was insignificant improvement in mechanical properties. The other two compositions retained the fine-scale micro/nanostructure, which resulted in hardness values greater than anticipated from rule-of-mixtures values.

The high strain-rate strength was evaluated for a series of samples that underwent HIP at 1375 °C. The samples were core-drilled, and surface finishes and parallelism of 1 μm were specified. SHPB (Kolsky) testing was used to evaluate the high strain-rate strength. Samples of all three compositions showed strengths from 4.5 to 6.7 GPa, while values of 3–4 GPa were reported in literature for conventional microstructures (figure 3). These values are more impressive, since the samples had serious surface damage, which should have degraded the strength. Initial fractography of the rubble showed that failure occurred primarily along the prior grain boundaries, rather than the stronger grain boundaries created during the transformation

11
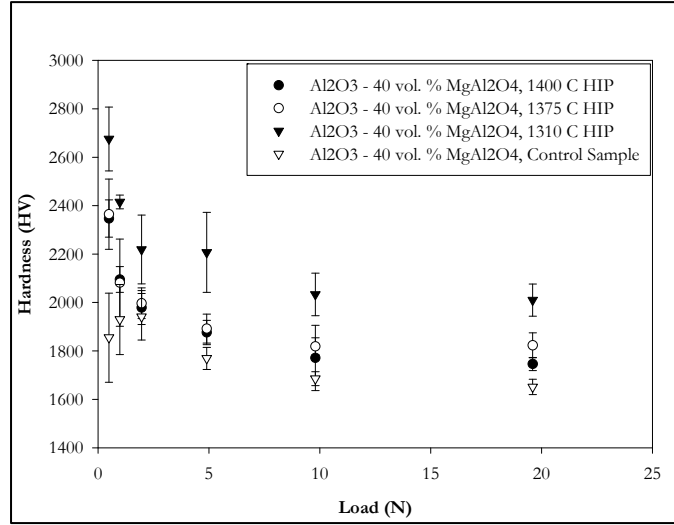
Figure 2. Hardness curves for Al_2O_3–40 volume-percent $MgAl_2O_4$ that underwent HIP at various temperatures.

process (figure 3). There was some amount of cleavage in the prior grain boundaries, but it was not significant. The rubble also highlighted the presence of plastic deformation and what has been initially deemed a pressure-induced phase transformation in the magnesium aluminate (figure 4). After examining the fragments, the root cause of the higher strength and hardness is believed to be related to low-angle, high-strength grain boundaries within the prior grains and limited dislocation motion due to the fine grain size. This mechanism is the basis for the Hall-Petch (*1*, *2*) relation that predicts increasing hardness with decreasing grain size in metals.

(a)

(b)
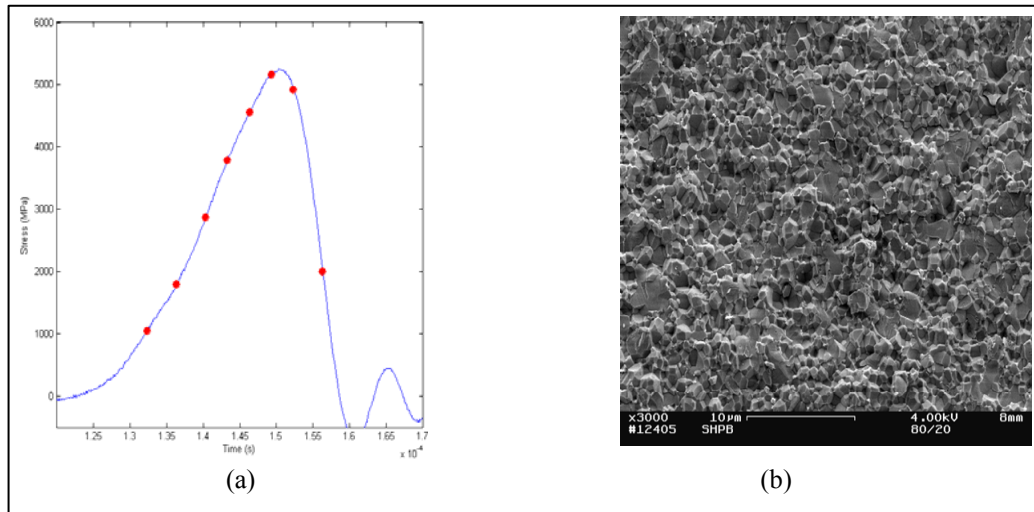
Figure 3. SHPB curve (a) and fracture surface of rubble (b).
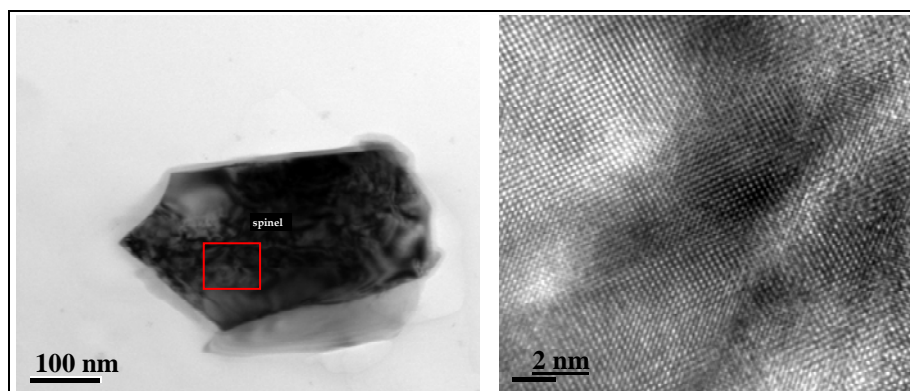
Figure 4. Above right shows high-magnification image of the region and above left,
where dislocations within the magnesium-aluminate rubble are visible.

The grinding behavior of the material was also examined using a testing technique developed at Chand Khar technical ceramics and NIST. The samples were machined into rectangular solids and then ground with 70-µm grit for 10 s with a fixed load of 9.8 N. The resulting material removal behavior appeared to be mostly ductile, which was unexpected, as the ductile grinding regime for these materials normally requires much higher grinding speeds, much smaller depths of cut, and much smaller grit size than used in these tests. The ground surfaces did not exhibit the classic brittle fracture removal mechanism normally seen for ceramics; therefore, the removal rates were slower than for commercial alumina.

2.8 References

1. Petch, N. J. Cleavage Strength of Polycrystals. *J. Iron Steel Inst.* **1953,** *174* (1), 25–28.

2. Hall, E. O. Deformation and Ageing of Mild Steels: Parts II and III. *Proc. Phys. Soc.* **1951,** *64* (9), 742–53.

3. Ryshkewitch, E. Compression Strength of Porous Sintered Alumina and Zirconia. *J. Am. Ceram. Soc.* **1953,** *36* (2), 65–68.

4. Knudsen, F. P. Dependence of Mechanical Strength of Brittle Polycrystalline Specimens on Porosity and Grain Size. *J. Am. Ceram. Soc.* **1959,** *42* (8), 376–87.

5. McCauley, J. W. U.S. Army Research Laboratory: Aberdeen Proving Ground, MD. Private communication, 2001.

6. Wilkins, M.; Honodel, C.; Sawle, D. An Approach to the Study of Light Armor; UCRL-50284; Lawrence Livermore National Laboratory: Livermore, CA, 1967.

7. Ortiz-Merino, J. L.; Todd, R. I. Relationship Between Wear Rate, Surface Pullout and Microstructure During Abrasive Wear of Alumina and Alumina/SiC Nanocomposites. *Acta Mat.* **2005,** *53*, 3345–3357.

8. Zhou, X. Metastable ZrO_2-Y203-Al_2O_3 Ceramics: Structure, Processing and Properties. Ph. D. Thesis, Rutgers University, Piscataway, NJ, 2002.

9. McEnerney, B. W.; Sadangi, R. K.; Niesz, D. E.; Kear, B. H. Novel Processing Approach to Create Improved Ceramic Nanocomposites for Anti-Ballistic Applications. Filed May 2005, docketed through Rutgers University.

3. High Strain-Rate Behavior and Dynamic Failure of Armor Ceramics

Core Faculty: K. T. Ramesh, J.-F. Molinari

ARL Collaborators: J. McCauley, E. S. C. Chin, T. W. Wright, S. Schoenfeld, A. Wereszscak (ORNL), E. Rapacki, R. J. Dowding, T. Weerasooriya, P. Patel, G. Gazonas

Graduate Students: B. Paliwal, R. Raghupathy

Research Scientist: F. Zhou

3.1 Objectives

The primary long-range objectives are to characterize and understand the failure mechanisms of ceramics under impact loading and to seek the factors that control these failure mechanisms at the macro, meso, and microstructure levels through experiments and simulations. This effort will help design ceramic composite armor structures that have optimized ballistic performance.

3.2 Key Accomplishments

- Developed Weibull-distributed cohesive strength models for modeling of the stochastic response of ceramics and the influence of defects

- Developed computational models that use dynamic insertion of cohesive elements to simulate brittle failure

- Developed a model for fragmentation of brittle materials that accounts for dynamic communication between cracks

- Demonstrated that the loss of ballistic performance of boron carbide at high impact velocities is correlated with the development of amorphous zones within this material

- Developed experimental techniques to measure the strength of armor ceramics at high strain rates

- Developed experimental techniques to observe the dynamic failure processes in armor ceramics under compressive loading

- Developed dynamic visualization of the dynamic Brazilian test for tensile loading of armor ceramics

- Used observation of the dynamic failure of a transparent ceramic (AlON) to demonstrate the importance of defect activation and damage growth in the interior of dynamically loaded ceramics

3.3 Selected Accomplishments

Significant advancements have been made on modeling of dynamic failure in ceramic materials. The efforts have focused on the discrete approach to cracking, e.g., cohesive elements, which represent cracks explicitly. We have developed Weibull-distributed cohesive strength models to achieve faster numerical convergence and capture size effects. These models have naturally led to a shift from the modeling emphasis to the analysis of the stochastic response of ceramics and the influence of defects at the microstructural level on macroscopic mechanical properties (*1*).

The improvements in the method's robustness have now enabled large-scale simulations of fragmentation. Fragmentation critically affects the mechanics of ballistic impact and fragment size estimates are often used as input in codes to assess armor ceramics performance. Our numerical investigations have focused on the statistics of fragmentation of ceramic materials, including the following: dependence of fragment size distributions on strain rate, elastic and fracture properties, and defect distributions (*2*).

High-resolution electron microscope observations of shock-loaded boron carbide have revealed the formation of nanoscale intragranular amorphous bands that occur parallel to specific crystallographic planes and contiguously with apparent cleaved fracture surfaces. This damage mechanism explains the measured (but not previously understood) decrease in the ballistic performance of boron carbide at high impact velocities and pressures (*3*). These results are now heavily cited in the literature on armor ceramics in general and boron carbide in particular, and they have been of great interest to armor ceramics manufacturers.

We have developed techniques to measure the dynamic strength of ceramics, and to observe the dynamic failure process in situ. These techniques have been applied to hot-pressed SiC (SiC-N) and B_4C, as well as to a number of sintered materials. The dynamic strength and dynamic fragmentation of a recently developed hot-pressed silicon carbide, SiC–N, was measured using a modified Kolsky-bar technique together with an MTS servo-controlled hydraulic test machine. The effect of loading rate on the uniaxial compressive strength was measured and analyzed through the wing crack array approach. It was confirmed that the inertia effect is primarily responsible for the rate effect in the high loading rate regime while subcritical crack growth dominates the effect of loading rate in the low strain-rate regime. High-speed photography was employed to observe and characterize in real-time the evolution of the failure mode and fragmentation during the test. Finally, quantitative analysis of the fragments was coupled with theoretical models to investigate the mechanism involved with fragmentation over loading rates from 10^{-4} to 10^3 MPa/μs. Similar observations were made with hot-pressed B_4C (figure 5).
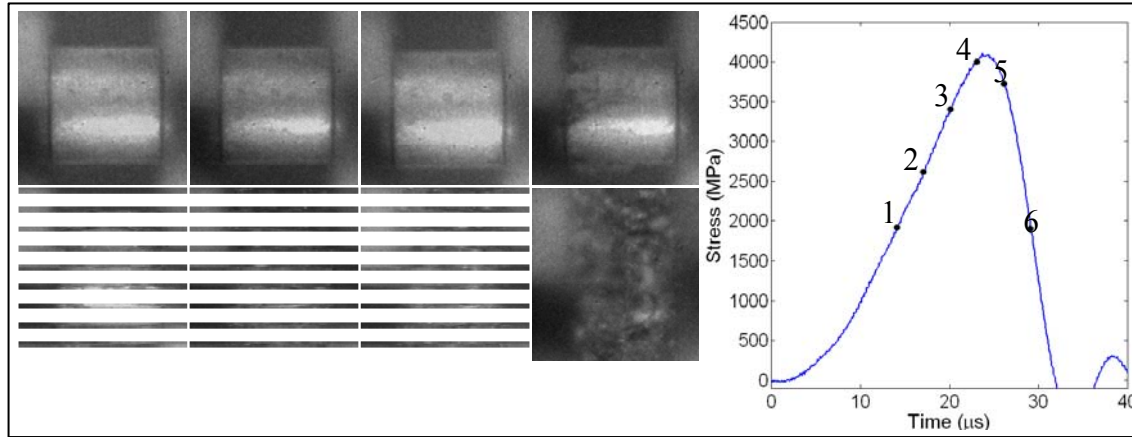
Figure 5. High-speed photographs of the dynamic failure of a hot-pressed B$_4$C specimen.

Subsequently, these techniques were used to examine the dynamic failure process in transparent AlON. The dynamic activation, growth, and coalescence of cracks and the resulting damage zones from spatially separated internal defects was directly observed and correlated to the macroscopic loss of load-carrying capacity and ultimate catastrophic failure of transparent AlON specimens. The high-speed photographs of the coated (and hence opaque) AlON specimens show the dynamic progressive failure on the specimen surface. This technique shows how a single failure mode appears to be dramatically different for the coated (opaque) and uncoated (transparent) specimens. Such fundamental studies of the dynamic failure process are key to developing an understanding of the complex phenomena involved in the ballistic event (*4, 5*).

Ceramics generally contain distributions of flaws such as microcracks or microvoids that cause stress concentration when loaded, and, hence, serve as possible crack nucleation sites. Once nucleated, these microcracks are believed to grow, interact and, coalesce, causing macroscopic failure of the ceramic. We have used high-speed photography (see figure 6) to study the dynamic failure of transparent AlON specimens undergoing uniaxial, high strain-rate compression (achieved through a modified Kolsky-bar technique). The high-speed photographs are correlated in time with direct measurements of the stresses in the specimen. The dynamic activation, growth, and coalescence of cracks and the resulting damage zones from spatially separated internal-processing defects have been directly observed and correlated to the macroscopic loss of load-carrying capacity and the ultimate failure of AlON. A scalar damage parameter (see green dotted curve in figure 6) was estimated from image analysis as the ratio of the area of the damaged region to the area of the specimen in the photographs. The observations suggest that the cause of the final failure for AlON under dynamic loading was the formation of a damage zone of a critical size that propagated in unstable fashion.

Ramesh Raghupathy, a graduate student who completed an M.S. degree, has begun to study the influence of defects on fragmentation. He has completed an analysis for the ideal case of a uniform distribution of defects. The results in figure 7 demonstrate that very simple scaling laws may be found for uniform distributions. These laws may be extended to account for more

17
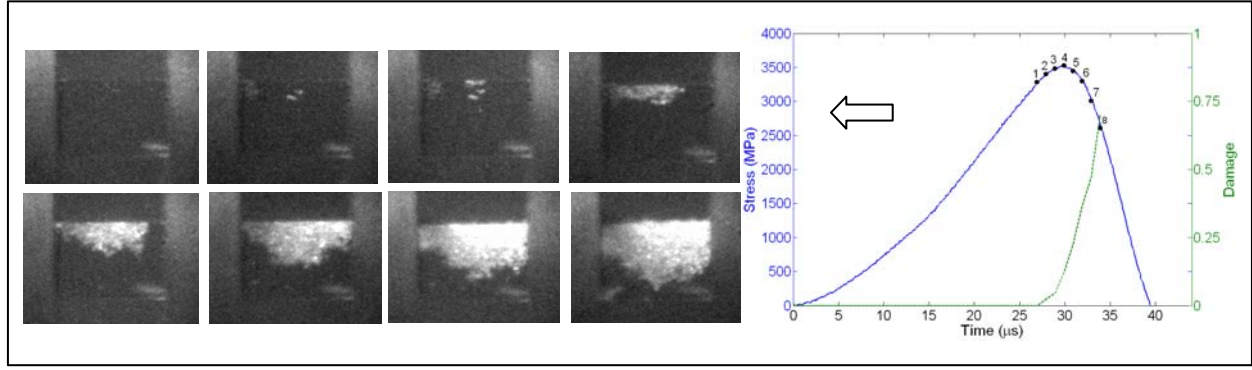
Figure 6. Photographs taken by the high-speed camera (interframe times of 1 μs, exposure times of 100 ns) of the dynamic failure process in transparent AlON. Stress and damage vs. time curves correspond to the photographs on the left.

diverse defect strength distributions, as any curve can be approximated by a superposition of uniform distributions. In addition, interesting results emerged from convergence studies conducted in collaboration with G. Gazonas (ARL). For the first time, we have been able to show that cohesive element results converge in an energetic sense. In other words, for a given strain rate there exists a mesh size below which the number of fragments becomes independent of mesh refinement. Cohesive energy convergence was identified as a key issue in the literature, and although achieving mesh independence is a computationally demanding task, our results give hope for the future of cohesive approaches.
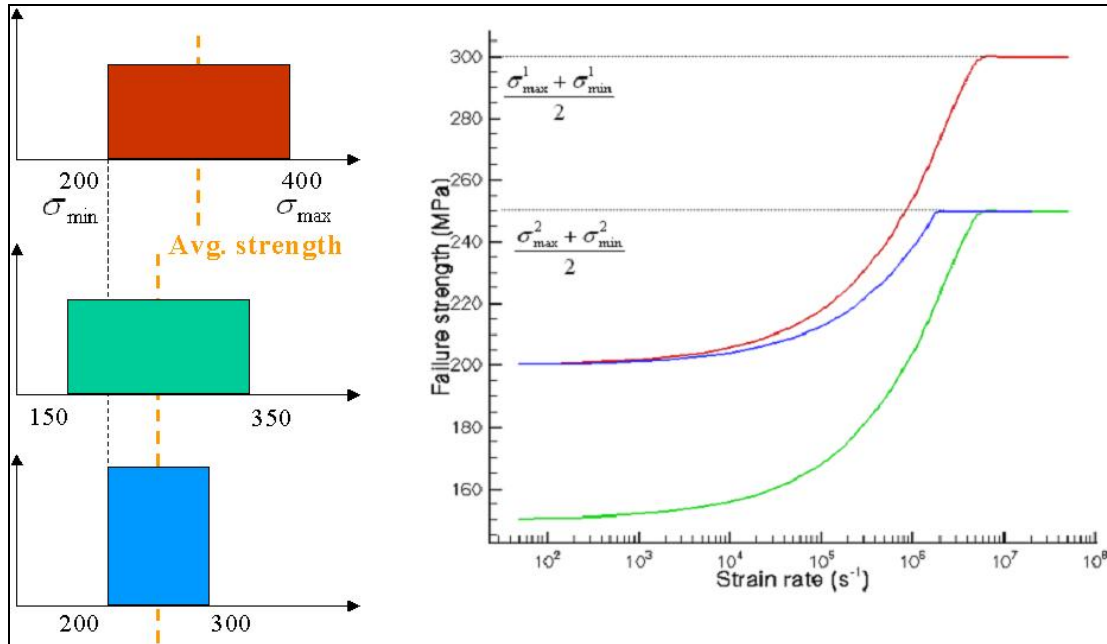
Figure 7. Influence of uniform defect distributions on ceramic macroscopic failure strength.

18

3.4   Collaborative Interactions

We have had extensive interactions with ARL scientists during meetings with and without the Rutgers collaborators. The discussions have helped increase the quality of the submitted papers and presentations at national and international conferences.

3.5   References

1. Zhou, F.; Molinari, J.-F. Three Dimensional Dynamic Crack Propagation Using Cohesive Elements: A Methodology to Address Mesh Dependency. *International Journal for Numerical Methods in Engineering* **2004**, *59* (1), 1–24.

2. Zhou, F.; Molinari, J.-F.; Ramesh, K. T. A Cohesive-Model Based Fragmentation Analysis: Effects of Strain Rate and Initial Defects Distribution. *Int. Journal of Solids and Structures* **2005**, *42* (18–9), 5181–5207.

3. Chen, W.; McCauley, J. W.; Hemker, K. J. Shock-Induced Localized Amorphization in Boron Carbide. *Science* **2003,** *299*, 1563.

4. Wang, H.; Ramesh, K. T. Dynamic Strength and Fragmentation of Hot-Pressed Silicon Carbide Under Uniaxial Compression. *Acta Materialia* **2004**, *52* (2), 355–367.

5. Paliwal, B.; Ramesh, K. T.; McCauley, J. W. Direct Observation of the Dynamic Compressive Failure of a Transparent Polycrystalline Ceramic (AlON). *J. Am. Ceram. Soc.* **2006**, *89* (7), 2128–2133.

4. Designed Macrostructures for Shock-Wave Management

Core Faculty: R. A. Haber, S. C. Danforth, V. A. Greenhut, D. E. Niesz

ARL Collaborators: J. McCauley, J. Adams

JHU Collaborators: F. Zhou, J.-F. Molinari, K. T. Ramesh

Graduate Student: R. McCuiston

Undergraduate Students: J. Cutrera, E. Azriel

4.1 Objectives

- To develop an understanding of the important factors in the design, fabrication, and testing of multimaterial macrostructured composites for reduced shock-wave transmission

- Using the concepts of phononic band gaps, design, fabricate, and test random and periodic macrostructured composites for reduced shock-wave transmission

4.2 Key Accomplishments

- Demonstrated, using numerical simulation, several Al_2O_3/WC-Co macrostructures that significantly reduced stress-wave propagation compared to monolithic Al_2O_3

- Demonstrated that the desired heterogeneous response to stress-wave propagation was observed when the scale of the macrostructure matched the pulse length of the stress wave and gradually transitioned to the response of a monolithic material when the pulse length was 5× the diameter of the WC-Co inclusions

- Demonstrated, through acoustic characterization of green (porous) Al_2O_3 containing WC-Co spherical inclusions, that the experimental results compared favorably with numeric simulation results

- Developed a procedure for fabricating periodic and random macrostructures of Al_2O_3 containing WC-Co spheres

4.3 Introduction

Grady (*1, 2*) has theorized that wave-scattering is a possible mechanism responsible for the creation of structured, steady shock waves during propagation in a heterogeneous material. Scattering would lead to dispersion of the shock wave, which could directly counteract the tendency of the shock front to steepen as it propagates. Scattering would also create a limited spectrum of nonequilibrium acoustic phonon energy behind the shock front, which could be

responsible for the excess stress between the Rayleigh line on which the shock wave travels, and the equilibrium thermodynamic path.

To verify Grady's wave-scattering-mechanism theory, research on shock-wave propagation in periodically layered composites was undertaken by Zhuang et al. (*3–6*). The research looked at the effect of acoustic impedance mismatch, interface density, and shock amplitude on shock-wave propagation. The effect of increasing acoustic impedance mismatch was to decrease the slope of the shock front. An increase in interface density and shock amplitude resulted in an increase in the slope of the shock front. It was found that the periodically layered composites could support steady, structured shock waves, and that the shock wave velocity could be lower than either of its components. It was concluded that wave scattering in the periodically layered composites was responsible for an increase in shock viscosity when compared with a homogenous material.

Hauver et al. (*7, 8*) used periodically layered composites as shock-wave attenuators to lessen the shock-wave-induced damage in ceramic targets during confined impact tests. To our knowledge, the material from which the shock-wave attenuator was fabricated has not been reported in the open literature. Our assumption is that it would have a large acoustic impedance mismatch and would likely be a combination of a ceramic/plastic, ceramic/metal, or a metal/plastic. Hauver et al. also did not address in the open literature how the design of the layered shock-wave attenuator was devised, be it purposefully designed or randomly selected.

The design of shock-wave attenuators evolved from semiconductor theory. In semiconductors, there exist certain energy levels that electrons are forbidden to occupy. These forbidden energy levels are referred to as a band gap. From this concept, Yablonovitch (*9, 10*) developed the idea of the photonic band-gap material. Yablonovitch theorized that if semiconductors could contain a band gap for certain electron energies (frequencies), then a material could exist with a band gap for other electromagnetic frequencies. Years of research resulted in a structure that blocked the propagation of all electromagnetic frequencies from 13–16 GHz.

Inspired in part by the research of Yablonovitch, it did not take long for other researchers to realize that the photonic band gap theory could be applied to other waveforms besides electromagnetic, as the laws of physics hold for all waveforms. Soon several research groups were at work to create structures containing acoustic band gaps or phononic band gaps, i.e., regions where no acoustic frequencies could be transmitted in a material (*11–14*). This is not a new field of research, but one that has been extensively studied in the past (*15*).

It is the recent work on phononic band-gap structures that was the motivation for this research. It is hypothesized that if a structure were fabricated properly, using the design tools of phononic band-gap research, a shock wave in part or in whole could be forbidden from propagating. This would yield a reduction in shock-wave-induced damage to materials underlying the site of a ballistic impact. This research focused on the design, fabrication, and characterization of such a structure.

4.4 Approach

Research was divided into two main areas: experimental simulation and numerical simulation. The goal of the experimental research was to fabricate random and periodic structures from ballistically important materials. It was decided to focus on the design and fabrication of 3-D phononic band-gap structures containing discrete scattering phase, as they are known to exhibit the widest band gaps. Figure 8 shows examples of 1-D, two-dimensional (2-D) and 3-D phononic band-gap structures.
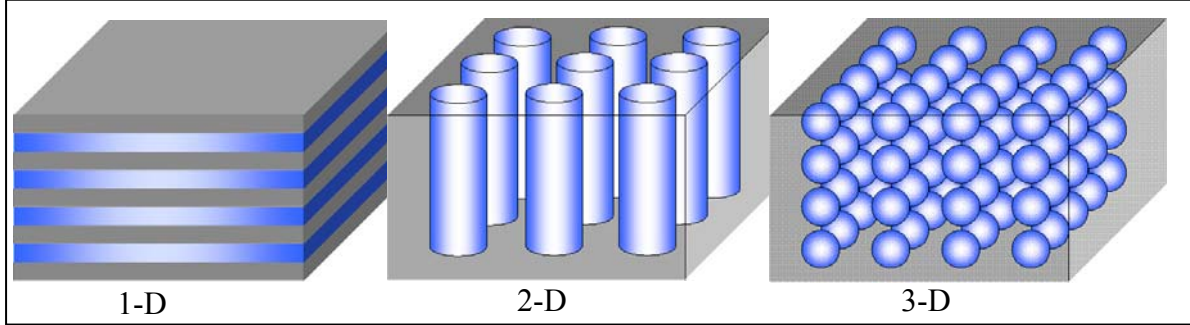
Figure 8. Examples of 1-D, 2-D, and 3-D phononic band-gap structures.

A phononic structure creates a band gap through a combination of Bragg diffraction (destructive interference) and Mie scattering. The Bragg equation (1) for diffraction is given by

$$n\lambda = 2L\sin\phi, \tag{1}$$

where n is an integer, λ is the wavelength, and L is the spacing between spheres. Mie scattering will occur when the diameter of the spheres is an integer multiple of the wavelength, allowing for a linear combination of resonances. A simple equation (2) for this is:

$$m\lambda = d, \tag{2}$$

where m is an integer multiple of the wavelength λ and d is the diameter of the scatterer. Once a wavelength of interest is determined, these two equations are the starting point for a phononic band-gap structure design. The wavelength of the shock wave in the material can be roughly estimated by multiplying the rise time of the loading by the longitudinal speed of sound (C_L), in the specific materials. The rise time is typically 20–100 ns and can be tailored for testing purposes. The C_L for ceramic materials is typically 10 km/s, though one could also assume the bulk velocity, which is typically 7–8 km/s. The estimate would yield a wavelength in the 1-mm region (assuming slower rise times and faster velocities) or 0.1-mm region (assuming faster rise times and slower velocities).

Fabrication was performed using a tape-casting and lamination scheme from a model material system of Al_2O_3 and WC-Co. To negate the need for experimentally fabricating and characterizing the multitude of possible structures, the design aspects of the research were handled using computer simulations. The computer simulations were done using the finite element method in collaboration with Professor J.-F. Molinari of the Johns Hopkins University. The selection of the model material system, the fabrication method, and the numerical simulations are discussed next.

4.5 Model Material System

The model material system selected for the research had to satisfy three important criteria. First, given the correct structural design, the materials must function together as a phononic unit. Second, the materials must be coprocessed at a temperature sufficiently high enough to cause densification. Third, the materials must be ballistically important to be of interest for impact studies.

To select an appropriate model system, the wide variety of possible material combinations was reduced to only those that are of interest ballistically, satisfying the third criterion. Table 1 lists a select few ballistically important materials. In order to have a model system that will function as a photonic unit, it first must be co-processed. Requirements for coprocessing include similar densification temperatures as well as similar coefficients of thermal expansion. From Table 1, several pairs of co-processable materials can be selected. The pairs include SiC/B_4C, TiB_2/AlN, TiB_2/B_4C, and Al_2O_3/WC-Co. Among these four pairs, only Al_2O_3/WC-Co has an acoustic impedance mismatch large enough to be of interest in regards to functioning as a phononic unit.

Besides its satisfaction of the three important criteria, the selection of Al_2O_3/WC-Co as a model material system has other benefits. There is a wealth of open literature on the ballistic behavior and characterization of aluminum oxide. Also, because tungsten carbide cobalt is a liquid phase sintered material, it can readily have its coefficient of thermal expansion tailored by additions or subtractions of the cobalt binder phase.

Table 1. List of material candidates for the model system (*16, 17*).

Material	E (GPa)	ρ (g/cm^3)	H (kg/mm^2)	C_{long} (km/s)	α ($\times 10^{-6}/°C$)	Sintering (ºC)	Z (kg/m^{2}s)
Al_2O_3	390	3.9	1900	10.5	7–8	1500 ±100	40.95×10^6
SiC	410	3.2	2500	12	4	1900 ±100	38.4×10^6
B4C	450	2.5	3200	13	4.5–6	2000 ±100	32.5×10^6
TiB_2	530	4.5	2900	10.75	5–8	1900 ±100	48.38×10^6
AlN	320	3.2	1100	10.75	4.4–5.7	1700 ±100	34.4×10^6
WC-Co	630	14.9	2100	7	5	1400 ±100	105×10^6

23

4.6   Experimental Fabrication and Characterization

There are many potential methods by which 3-D macrostructures can be fabricated. Among the easiest is simply to mix the two constituents and then uniaxially dry press them. This is the method by which random macrostructures were created for sintering studies in this research. The creation of periodic macrostructures is particularly challenging when the periodic macrostructure has a discontinuous phase. Ideally, whichever method is selected should be robust enough to allow the fabrication of multiple designs without the need for expensive tooling or machining it, and it should be precise enough to ensure the proper placement of the scattering phase.

In this work, fabrication was done using a tape-casting and lamination scheme. Thick alumina tapes (+1 mm) were cast, and periodic arrays of holes were punched in the tape. The holes were punched using plastic jigs with a predetermined, periodic array of drilled holes. The holes in the tape were filled with WC-Co inclusions and laminated together with blank tapes to create the 3-D periodic structures.

4.7   Numerical Simulation

The design aspects of the research were handled using numerical simulations to negate the need for experimentally fabricating and characterizing the multitude of possible macrostructures. Due to the difficultly in creating a 3-D finite element mesh (FEM) containing discrete internal inclusions, a decision was made to simulate 2-D cross sections. To observe the stress-wave propagation in the absence of fracture or other permanent deformations, the simulations only incorporated elasticity. Therefore, the only energies present within the model are in the form of kinetic energy (KE) and strain energy (SE). A series of simulations were run that studied the effect of WC-Co diameter, area-percent, and stacking order. The macrostructures were characterized by studying the rear face displacement, partitioned kinetic and strain energy, and equivalent stress fields.

4.8   Experimental Results

The effect of sintering temperature on the model system was studied using die-pressed Al_2O_3 (Malakoff RC-HP-MAR grade) samples containing randomly placed inclusions of WC-Co (Valenite). The inclusions were 300–500 μm in diameter. Pellets 3.8 cm in diameter and containing 10, 20, 30, 40, and 50 volume-percent WC-Co inclusions were pressed. The pellets were set in a borennitride powder bed in a graphite crucible and sintered under a dynamic vacuum of 100 mTorr in a graphite resistance furnace at 1350, 1450, and 1500 ºC for 2 hr. Figure 9 shows the as-cut cross sections of samples sintered at the three temperatures.
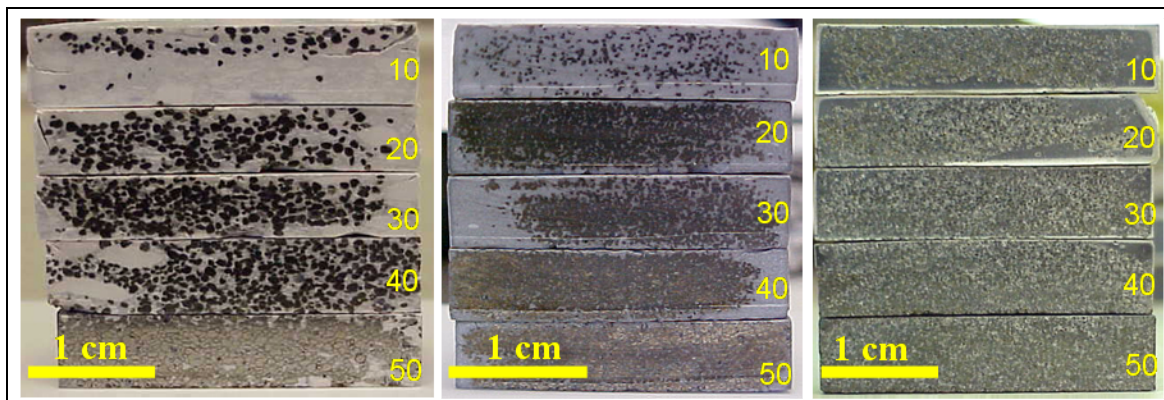
Figure 9. As-cut cross sections of (left to right) set 1 sintered at 1350 ºC, set 2 sintered at 1450 ºC, and set 3 sintered at 1500 ºC. The 10–50 labels on all sets denote the volume-percent of WC-Co granules present.

The cross sections of samples sintered at 1350 ºC showed processing flaws and pull-out of the WC-Co granules. The cross sections of samples sintered at 1450 ºC showed a reduction of processing flaws (due to improved processing) as well as a reduction in pull-out of the WC-Co granules. The cross sections of samples sintered at 1500 ºC show the alumina phase to be black, most likely due to cobalt contamination. This would also be indicated by an increase in weight loss after firing over the 1450 ºC samples. There was also an increase in WC-Co granule pull-out during sectioning, which indicates a decrease in bond strength compared to samples sintered at 1450 ºC.

Vickers hardness at the interface was measured in order to quantify the Al_2O_3/WC-Co bonding differences between the three sintering temperatures. Cross sections of the three sets containing 10 volume-percent WC-Co were mounted in epoxy and polished to a 0.5-μm surface finish using a combination of SiC grit paper and diamond slurry. Hardness was measured with a Leco M-400-G3 hardness tester using a 2-kg load with a 10-s hold. Fifteen measurements were taken in the Al_2O_3, WC-Co, and at the interface. The average hardness and deviation is shown in table 2.

Table 2. Vickers hardness of three sets containing 10 volume-percent WC-Co. Units are kilograms per square millimeter.

Temp (ºC)	Alumina Hv	WC-Co Hv	Interface Hv
1350	727 ± 25	867 ± 93	650 ± 143
1450	1866 ± 69	1726 ± 97	1685 ± 169
1500	1842 ± 113	1494 ± 180	1043 ± 254

The samples sintered at 1350 ºC had extremely low hardness in the Al_2O_3 and WC-Co and even lower hardness at the interface; however, this is to be expected because 1350 ºC is below the sintering temperature for both materials. Samples sintered at 1450 ºC had high hardness in the Al_2O_3 and WC-Co. The interface between the two had a composite hardness of 1685 ± 169, which is still high and indicates good bonding. Samples sintered at 1500 ºC showed no statistical

difference in hardness for Al_2O_3 and WC-Co, but the interfacial hardness decreased drastically, indicating a decrease in bond strength.

Green Al_2O_3 samples containing periodic and random inclusions of WC-Co (Ceratizit) were fabricated by a tape-casting and lamination technique. Al_2O_3 tapes of various thicknesses were cast based upon the diameter of the WC-Co inclusions. Periodic arrays of holes were punched in the Al_2O_3 tapes, and the holes were filled with the WC-Co inclusions. Figure 10 shows examples of the as-punched layers of tape containing periodic arrays of holes. Alternating layers of tapes filled with WC-Co inclusions were laminated together. Figure 11 shows an example of an as-laminated structure containing periodically placed WC-Co. An Al_2O_3 sample containing no WC-Co was also fabricated as a baseline. The fabricated samples were ~50 mm (12–15 mm) in diameter and 12–15 mm thick. The periodic and random macrostructures contained four layers of WC-Co inclusions, either 1 or 2 mm in diameter.
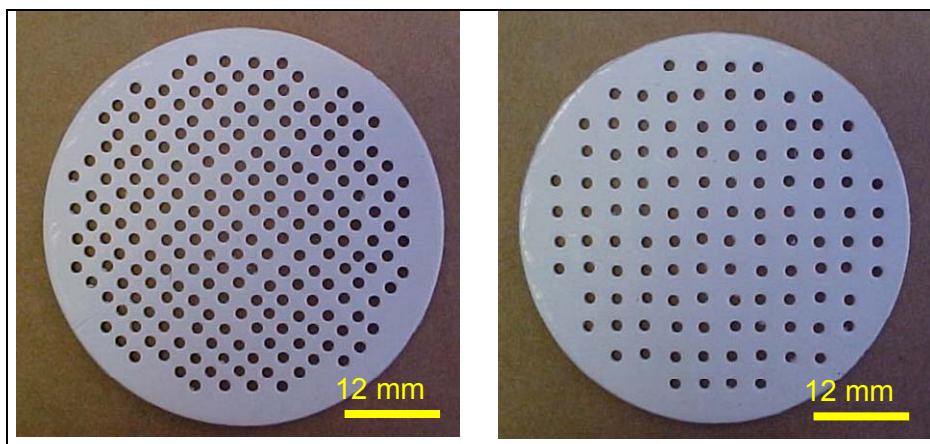
Figure 10. The 50- × 1.5-mm tape-cast blanks with periodic arrays of 1.5-mm-diameter holes.

Figure 11. The 50-mm-diameter sample containing periodically placed WC-Co.

A series of 13 samples were acoustically tested using noncontact transducers and through transmission at a center frequency of 0.5 MHz. The diameters of the transducer crystals were 12.5 mm. Time-of-flight measurements were made at five different locations on the samples (resembling an X-shaped pattern), and the results were averaged in order to calculate the wave velocity. Unfortunately, four of the samples did not allow a strong enough signal to transmit and resulted in only one measurement each.

The baseline alumina monolith had the fastest returned sonic velocity at 1688 m/s. The slowest returned sonic velocity, 1169 m/s, was measured for a sample containing 20 area-percent of 2-mm-diameter inclusions in body-centered tetragonal arrangement. Velocity scans for these two samples are shown in figure 12. The 20% 2-mm body-centered tetragonal sample is equivalent to a 20% 2-mm hexagonal structure in cross section. From 2-D FEM wave propagation simulations, the 20% 2-mm hexagonal structure was shown to behave similarly to a 40% 2-mm hexagonal structure. The 40% 2-mm hexagonal structure was judged to have the best simulated performance.
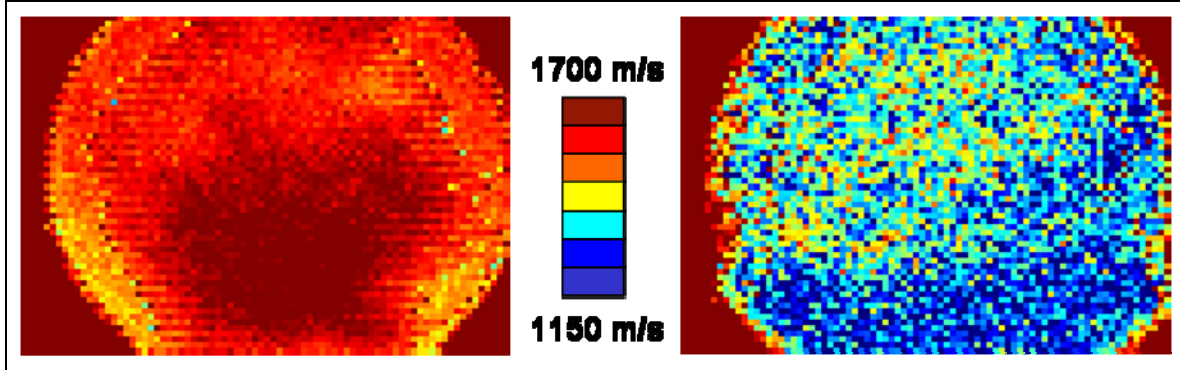
Figure 12. Through transmission of green baseline Al_2O_3 monolith (left) and 20% 2-mm body-centered tetragonal composite (right).

4.9   Numerical Results

Two-dimensional elastic FEM simulations were performed on 77-mm-wide × 13-mm-thick cross sections. Structures were meshed containing 20 and 40 area-percent of 0.5-, 1-, and 2-mm-diameter WC-Co inclusions. They were arrayed in simple cubic, hexagonal, and random arrangements. A 5-GPa load was applied in a trapezoidal manner, with rise and fall times of 1 ns and three plateau durations of 20, 60, and 100 ns. The load was applied in the center of the top surface with a radius of 2.5 mm.

Figure 13 shows two equivalent stress contour plots for the baseline Al_2O_3 monolith and the 40% 2-mm hexagonal composite, both loaded with a 20-ns plateau. The plots are at 1.1 µs, which is just before the shock pulse reflects from the rear surface. In figure 13 (left), it is seen for the baseline that just before the shock pulse reflection, the majority of the high stress is located near the rear face. The shear wave is also clearly visible. In figure 13 (right), the opposite is true. The majority of the high stress is still located near the top. The shear wave and longitudinal wave are no longer resolvable. It is apparent that the 40% 2-mm hexagonal composite is a having a large influence on the shock pulse propagation.

The location of the KE and SE in the model during the loading event was monitored using a partitioning scheme. A schematic of the partitioning scheme is shown in figure 14. The partitioning scheme first divides the model axisymetrically along the vertical axis. The right half
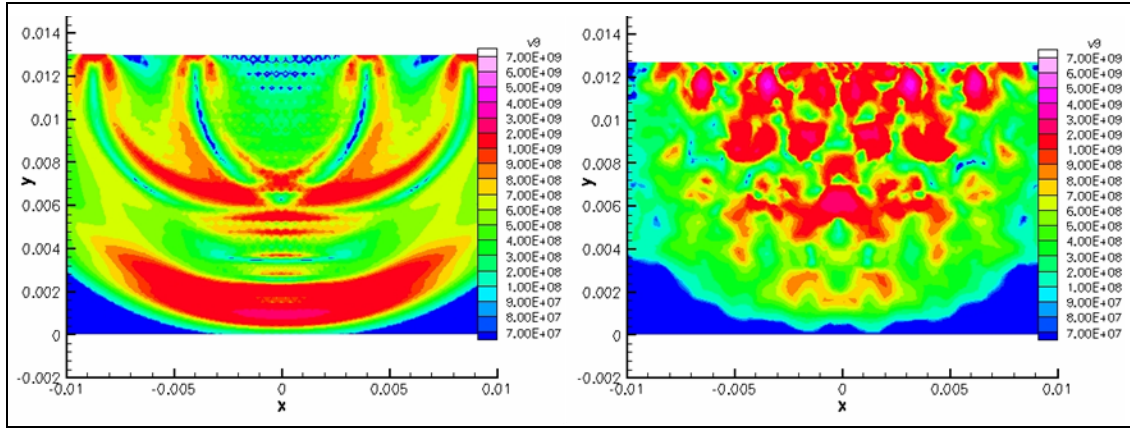
Figure 13. Equivalent stress contour plot for 20-ns load plateau for baseline Al_2O_3 monolith (left) and 40% 2-mm hexagonal composite (right). The stress scale is in gigapascals and the x-y scales are in meters. Both plots were captured at 1.1 μs.
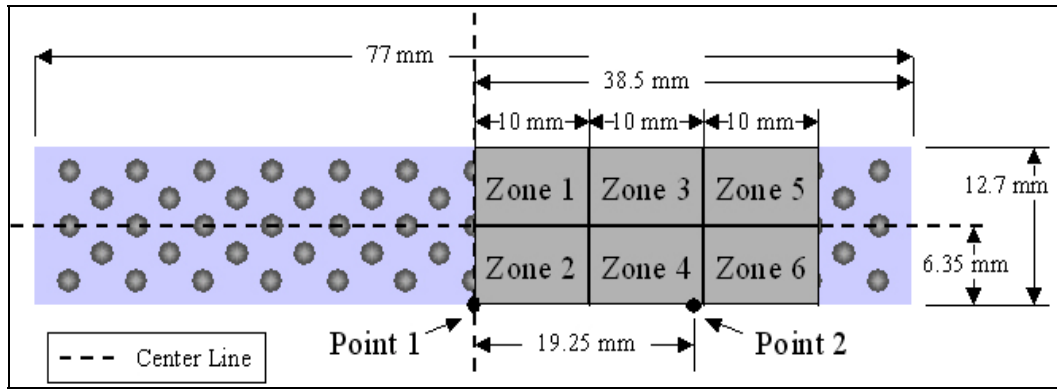
Figure 14. Schematic of the partitioning scheme. The partitions are labeled as zones 1–6.

of the model is then partitioned into six zones. The zones do not extend to the horizontal edge of the model to avoid any potential problems arising from the boundary conditions.

Results for partitioned KE and SE for the baseline Al_2O_3 monolith and the 40% 2-mm hexagonal composite are shown in figure 14. The load plateau was 20 ns. The plot of KE for the alumina monolith, shown in figure 15 (top left), initially shows the level of KE in zone 1 increase and reach a maximum for a short duration. The KE in zone 1 decreases as it is transferred into zone 2. The KE level in zone 2 then increases and reaches a maximum, at which point the shock pulse is reflected from the rear face and travels back towards zone 1. The process of KE transfer between zone 1 and zone 2 continues for the duration of the simulation with the maximum KE levels in zone 1 and 2 decaying as the KE is spread laterally into the remaining four zones. It is clear from the plot of SE for the baseline Al_2O_3 monolith, shown in figure 15 (bottom left), that there are two distinct groupings of SE. The upper zones 1, 3, and 5 contain the majority of SE. The bottom zones 2, 4, 6 contain the least amount of SE. As the loading occurs on the top surface, it will experience the most elastic deformation and should have the bulk of the SE. Zones 5 and 6 exhibit spikes in the SE, most likely due to wave reflections from the sides.

28
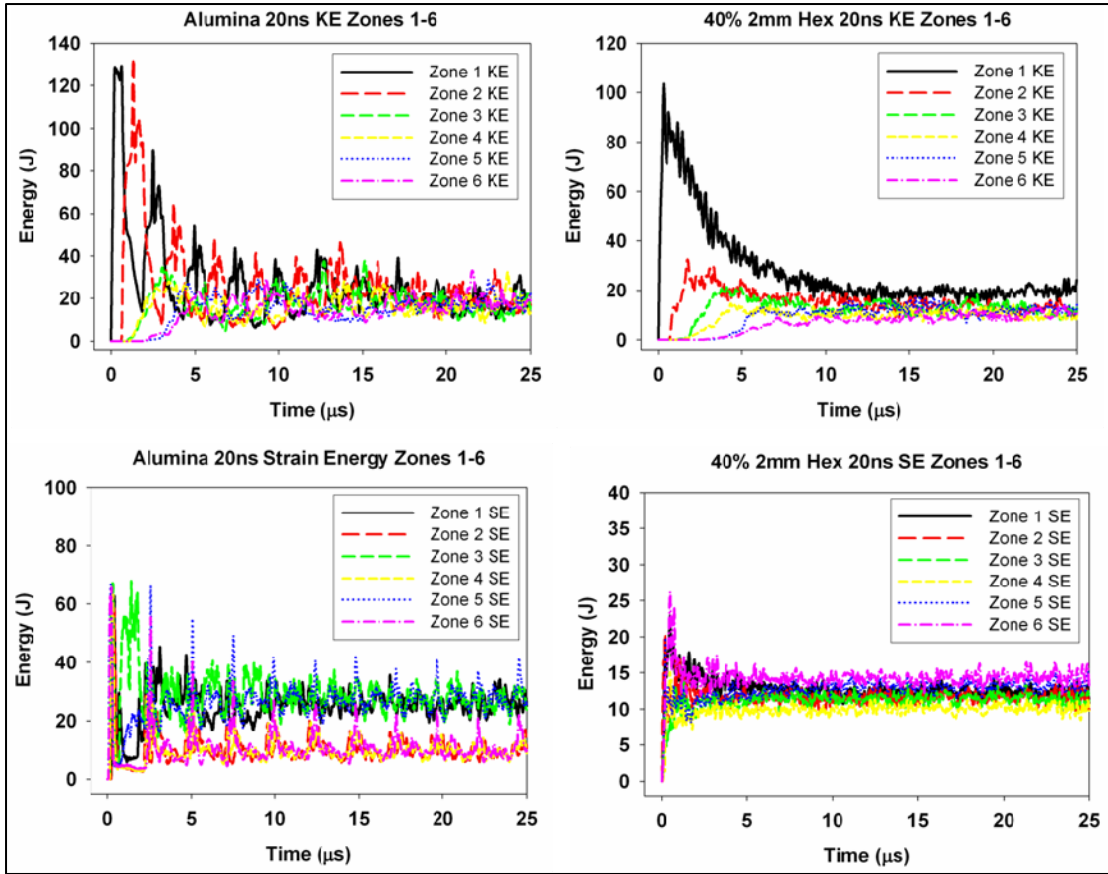
Figure 15. Partitioned KE and SE for zones 1–6 of the alumina monolith and 40% 2-mm hexagonal macrostructure—monolith KE zones 1–6 (top left), monolith SE zones 1–6 (bottom left), 40% 2-mm hexagonal KE zones 1–6 (top right), and 40% 2-mm hexagonal SE zones 1–6 (bottom right).

Plots of KE and SE for the 40% 2-mm hexagonal composite are also shown in figure 15. It is immediately seen in figure 15 (top right) that the shape of KE curves for the composite are vastly different from the baseline Al_2O_3 monolith. Like in the baseline, the KE in zone 1 increases to a maximum. But rather than transfer immediately into zone 2, the KE in zone 1 instead begins a gradual decay. There are no large amplitude oscillations of the KE as in the baseline, which corresponded to shock pulse reflections from the top and bottom surfaces. Instead, there were a series of smaller amplitude oscillations superimposed on the decaying curve. These smaller oscillations are most likely attributed to reflections from the WC-Co inclusions. There is still KE transfer to the remaining four zones. The plot of SE for the composite, shown in figure 15 (right bottom), also shows a vastly different behavior when compared with the baseline Al_2O_3 monolith. There is an immediate increase of SE in all six zones that is attributed to rigid body motion, but rather than segregating into two distinct SE groupings as with baseline, the SE curves all converge toward a single cluster. There are no large amplitude SE oscillations, like in zones 5–6 of the baseline, but, again, a series of smaller amplitude oscillations most likely attributed to shock pulse reflections for the WC-Co inclusions. It is clear from figure 15 that the

40% 2-mm hexagonal structure is immediately trapping a large portion of the shock energy near the loading site.

4.10 Accomplishments and Conclusions

4.10.1 Experimental

1. A tape-casting and lamination scheme was used to create periodic and random Al_2O_3/WC-Co composites. Using the proper jig, closely spaced holes can be punched through 1+ mm-thick tapes without cracking. It was found that the diameter of the punched holes should be slightly larger than the diameter of the WC-Co inclusions to allow for easy insertion. The thickness of the Al_2O_3 tape should be slightly larger than the diameter of the WC-Co inclusions to allow for proper lamination.

2. Glycerin and cellosolve acetate were used successfully as lamination aides for Al_2O_3 tapes that contain 7 weight-percent B-1000 binder. Only cellosolve acetate was used successfully to laminate Al_2O_3 tapes containing 15 weight-percent B-1000 binder. The optimal laminating conditions for Al_2O_3 containing WC-Co inclusions were determined to be a confined lamination at a temperature of 80 ºC with a multistep pressure cycle that peaked at just over 15 MPa.

3. Transmission acoustic characterization of tape-cast and laminated green tape samples showed that the incorporation of a small volume-percent of 1–1.5-mm WC-Co inclusions significantly reduced acoustic wave velocity in comparison to an Al_2O_3 monolith. While the average acoustic velocity was approximately the same for samples containing WC-Co in a random or body-centered tetragonal arrangement, the velocity map for the random sample was very nonuniform in comparison to the body-centered tetragonal sample. Samples containing WC-Co in a tetragonal arrangement generally had faster acoustic velocities in comparison to the other samples containing WC-Co. Periodically spaced regions of high velocity corresponding to areas devoid of WC-Co were seen from the velocity map.

4. The use of hydrogen in the form of either ammonia or forming gas was a poor choice for residual carbon removal from 12+ mm-thick high green density specimens. In a reduced-pressure atmosphere of forming gas or ammonia, the kinetics of carbon removal were extremely slow. It was found that the carbon removal rate was faster with ammonia than with forming gas.

5. Al_2O_3/WC-Co was successfully co-fired to form a viable composite system. Up to 50 volume-percent of WC-Co granules was incorporated in Al_2O_3. The optimal sintering conditions as determined by hardness indentation and microscopy were a maximum temperature of 1450 ºC for 2 hr under a dynamic vacuum atmosphere of ~100 mTorr. It was also concluded that the individual green densities of the Al_2O_3 and WC-Co should be as close as possible in order to minimize cracking.

6. There was no chemical bond formed between the Al_2O_3 matrix and WC-Co inclusions. Fracture surfaces reveal that the crack path deviates around the WC-Co inclusions along the Al_2O_3/WC-Co interface. Examination of craters in the Al_2O_3 where WC-Co inclusions were pulled out reveals areas of micrometer-scale spheres of cobalt exhibiting nonwetting behavior.

4.10.2 Numerical Simulation

1. The Al_2O_3/WC-Co macrostructures have one of three responses to the propagating stress wave—homogeneous, heterogeneous, or mixed mode. The homogeneous response occurred when the scale of the macrostructure was smaller than the wavelength of the propagating stress wave. The structure essentially responds as a monolithic material. (The homogenous response can also occur when the size scale of the structure is much larger than the propagating wave, but this was not studied.) The heterogeneous response occurred when the scale of the macrostructure was very near the wavelength of the propagating stress wave. The mixed-mode response occurred when the scale of the macrostructure was somewhat larger or smaller than the wavelength of the propagating stress wave. The mixed-mode is sparse was a combination of the homogeneous and heterogeneous responses.

2. The response of an Al_2O_3/WC-Co structure was primarily determined by the diameter of the WC-Co inclusion. The response was reinforced by increasing the content from 20 area-percent to 40 area-percent. The characteristic pulse length of the stress wave is ~2, 5, and 10 mm for the load durations of 20, 60, and 100 ns, respectively. The 0.5-mm WC-Co inclusions responded homogenously for all durations. The 1-mm WC-Co inclusions initially responded mixed mode and then transitioned to a homogeneous response. The 2-mm WC-Co inclusion responded heterogeneously and transitioned through the mixed-mode response to a homogeneous response. When the pulse length was equal to the inclusion diameter, wave scattering was amplified which resulted in the heterogeneous response. For pulse lengths that are within ~4–5× the inclusions diameter, the response is mixed mode. For pulse lengths that were greater than ~5× the inclusions diameter, the response was homogeneous.

3. The stacking arrangement of the WC-Co did not have a large effect in determining response. This was due to the 2-D nature of the simulations. The random and hexagonal structures show similar performance. The tetragonal structures were not the optimal structure in any simulation. This is due to the vertical columns of Al_2O_3 present in the tetragonal structure. The simulation results compare favorably with the findings of the acoustic characterization of green samples.

4. In order to reduce stress wave propagation, the heterogeneous response is the desired response for a structure to have. The heterogeneous response is characterized by the following: indistinguishable longitudinal and shear wave components in the stress wave,

reduced bulk stress wave velocity, the emergence of an inverted triangular-shaped high-stress region with the bulk of the high stress located near the loading surface, the entrapment and slow release of KE near the loading surface, and the emergence of large-amplitude scattering-induced oscillations on the displacement curves.

5. Several Al_2O_3/WC-Co structures were identified that significantly reduce stress wave propagation when compared to monolithic Al_2O_3.

4.11 Proposed Future Work

4.11.1 Improved Processing

Due to the need to protect WC-Co from oxidation, binder removal had to be performed under vacuum. The lack of oxygen, therefore, resulted in an appreciable amount of residual carbon char that necessitated removal before sintering could be performed. This carbon removal step added time to an already long binder-removal cycle. It also required the use of noxious gases (such as ammonia) or potentially explosive gas mixtures (such as nitrogen + hydrogen). The through-put and safety of the binder-removal cycle would greatly improve by reformulating the tape-casting slip to use a binder producing little or no char under inert atmosphere conditions. A poly (alkylene carbonate) binder, manufactured by Empower Materials under the name QPAC,[*] has become available and is noted for its extremely low residual carbon content after binder removal, even under inert conditions.

Another area where improvements can be made is in punching of holes to create periodic arrays. Jigs were fabricated for hole-punching, and while they worked quite well, they still required manual operation. After several thousand holes, manual operation becomes an onerous task. The creation of cylinderical channels in tape-cast materials is a standard industry practice, but, typically, expensive specialized machines are used. Schneider and Marquard, Inc. specialize in microhole-punching of various materials. They sell hole-punching machines as well as offer toll services for hole punching.

4.11.2 Additional Macrostructures

A large gain may be realized in studying the so-called broad-band structures. Broad-band structures typically incorporate multiple size inclusions or multiple inclusion unit cells. This enables the structure to interact with a broader spectrum of wave lengths and, thus, to have a broader band gap. While structures incorporating one inclusion size with multiple inclusion unit cells would be cheaper and easier to fabricate, it probably would not function as well as a structure incorporating multiple inclusions sizes.

---

[*]QPAC is a registered trademark of Empower Materials, Inc.

4.11.3 Refined Numerical Simulations

Finite element simulations performed in this thesis research were done in the absence of material inelasticity and projectile interactions. Further finite element simulations should incorporate cracking and/or plastic deformations to study the evolution of wave interactions with damaged structures. Incorporation of a projectile would allow for the study of structure—projectile interactions as well as wave interactions arising from reflections within the projectile itself.

Another area of that deserves study is the effect of bond strength between the Al_2O_3 and WC-Co. Simulations in this research assume a perfect interface, but this is not the case in real samples. Obviously, if the interface separates early on during an impact, the wave-scattering ability of the structure will be affected.

Relatively advanced simulations, like those just discussed, would best be studied using commercially established FEM software. LS-DYNA, offered by the Livermore Software Technology Corp. and originally developed by Lawrence Livermore National Laboratory, is well-suited for dynamic simulations involving deformations and penetration (*18*, *19*).

4.11.4 Ballistic Characterization

An important area of research that was not able to be included in this thesis is ballistic characterization. Numerical simulations can go only so far before it becomes important to directly observe the impact behavior of the structures. Determination of failure mechanisms would be invaluable not only for design and fabrication of subsequent structures, but also for incorporating the data into numerical simulation models. Plate impact studies, using diagnostic tools such as strain gauges and VISAR, would likely be the method of choice.

4.12 References

1. Grady, D. E. Physics and Modeling of Shock-Wave Dispersion in Heterogeneous Composites. *Journal de Physique IV*, Colloque C3, **1997**, 669–674.

2. Grady, D. E. Scattering as a Mechanism for Structured Shock Waves in Metals. *Journal of the Mechanics and Physics of Solids* **1998**, *46*, 2017–2032.

3. Grady, D. E.; Ravichandran, G.; Zhuang, S. Continuum and Subscale Modeling of Heterogeneous Media in the Dynamic Environment. *Science and Technology of High Pressure – Proceedings of AIRAPT-17*; Manghnani, M. H., Nellis, W. J., Nicol, M. F., Eds., 2000, 189–193.

4. Zhuang, S. Shock Wave Propagation in Periodically Layered Composites. Ph.D. Thesis, California Institute of Technology: Pasadena, CA, 2002.

5. Zhuang, S.; Ravichandran, G.; Grady, D. E. Influence of Interface Scattering on Shock Waves in Heterogeneous Solids. *Shock Compression of Condensed Matter*; Furnish, M. D., Thadhani, N. N., Horie, Y, Eds., 2001, 709–712.

6. Zhuang, S.; Ravichandran, G.; Grady, D. E. An Experimental Investigation of Shock Wave Propagation in Periodically Layered Composites. *Journal of the Mechanics and Physics of Solids* **2003**, *51*, 245–265.

7. Hauver, G.; Dehn, J. Interface Defeat Mechanisms in Delayed Penetration. *Proceedings of the 1995 US-GE Armor/Anti-Armor Workshop*, 13–16 June 1995, 217–229.

8. Hauver, G.; Netherwood, P.; Benck, R.; Kecskes, L. Ballistic Performance of Ceramic Targets. *Proceedings of the 13th U.S. Army Symposium on Mechanics*, Plymouth, MA, 17–19 August 1993.

9. Yablonovitch, E. Inhibited Spontaneous Emission in Solid-State Physics and Electronics. *Physical Review Letters* **1987**, *58*, 2059.

10. Yablonovitch, E. Photonic Crystals: Semiconductors of Light. *Scientific American* **2001**, *285* (6), 46–55.

11. Kushwaha, M. S.; Halevi, P.; Dobrzynski, L.; Djafari-Rouhani, B. Acoustic Band Structure of Periodic Elastic Composites. *Physical Review Letters* **1993**, *71* (13), 2022–2025.

12. Vasseur, J. O.; Djafari-Rouhani, B.; Dobrzynski, L.; Kushwaha, M. S.; Halevi, P. Complete Acoustic Band Gaps in Periodic Fibre Reinforced Composite Materials: The Carbon/Epoxy Composite and Some Metallic Systems. *J. Phys. Condens. Matter* **1994**, *6*, 8759–8770.

13. Sigalas, M. M.; Soukoulis, C. M. Elastic-Wave Propagation Through Disordered and/or Absorptive Layered Systems. *Phys. Rev. B*, **1995**, *51* (5), 2780–9.

14. Kafesaki, M. M.; Sigalas, M.; Economou, E. N. Elastic Wave Bad Gaps in 3-D Periodic Polymer Matrix Composites. *Sol. State Comm.* **1995**, *96* (5), 285–289.

15. Brillouin, L. *Wave Propagation in Periodic Structures*; Dover Publications, Inc.: New York, NY, 1953.

16. Holmquist, T. J.; Rajendran, A. M.; Templeton, D. W.; Bishnoi, K. D. *A Ceramic Armor Materials Database*; technical report number 13754; U.S. Army Tank Automotive Research Development and Engineering Center (TARDEC): Warren, MI, 1999.

17. ASM International. *Engineered Materials Handbook*; *Vol. 4, Ceramics and Glasses*; ASM International: Cleveland, OH, 1991.

18. Her, S.; Liang, Y. The Finite Element Analysis of Composite Laminates and Shell Structures Subjected to Low Velocity Impact. *Composite Structures* **2004**, *66*, 277–285.

19. Lopatnikov, S. L.; Gama, B. A.; Haque, J., M. D.; Krauthauser, C.; Gillespie, J. W. High-Velocity Plate Impact of Metal Foams. *International Journal of Impact Engineering* **2004**, *30*, 421–445.

5. Statistical Analysis of Inclusions in Silicon-Carbide Armor Ceramics

Core Faculty: V. A. Greenhut, R. Haber, D. E. Niesz

ARL Collaborators: J. Adams, J. McCauley

NIST Collaborators: G. Quinn

Graduate Student: M. Bakas

5.1 Long-Range Objectives

- Identify unique material characteristics of poor-performing commercial SiC samples

- Model processing of SiC to identify conditions that lead to microstructural/structural differences that cause variation in ballistic performance

5.2 Introduction

Variability in ballistic performance among nominally identical ceramic armor tiles compromises ceramic armor design. One possible explanation of this variability is defects in the ceramic. A defect for a ceramic could take numerous forms, e. g., scratches from machining, porosity, and inclusions of another material (*1, 2*). Under quasi-static loading conditions, these defects concentrate applied stresses (*3, 4*). These stress concentrations can initiate fracture, and as ceramics are brittle materials, this fracture leads to catastrophic failure. Since the worst defect will initiate fracture under the lowest stress, the strength of a ceramic under quasi-static conditions is determined by the most severe defect (*5*). The most severe defect will vary from sample to sample. As a result, variation is observed in the quasi-static strengths of ceramics, which can be statistically defined using Weibull Theory (*5, 6*).

With defects playing such a critical role in the quasi-static failure of ceramics, it is probable that they also contribute to ballistic failure. However, the dynamic loading which occurs from a ballistic impact creates different conditions. It has been hypothesized in previous work that fracture initiates from preexisting defects under dynamic conditions (*7–9*). However, the rapid loading from a ballistic impact means that fracture from one specific defect will not propagate enough to cause failure by itself before the load increases. In a highly dynamic event, fracture is likely to be initiated from multiple defects. The assumption that the weakest link controls the failure necessary to apply Weibull statistics does not apply in this case, so the methods used to define the variability under quasi-static conditions are not to be directly applicable to ballistic performance. Therefore, is currently undefined what influence this fracture from preexisting defects has on the ballistic performance of a ceramic.

The purpose of this research is to obtain a better understanding of the relationship between defects and ballistic performance. Given the role of defects in determining the quasi-static strength of ceramics, it seems probable they influence ballistic failure. By better defining this relationship, it is hoped that the variability in armor ceramics can better understood, and ceramic armor design improves to produce more efficient systems.

5.3 Approach

A single armor ceramic (SiC-N) was chosen as the focus of this study. In order to determine the prominent processing defects of the material, the failure origins of quasi-static samples and the rubble from ballistic tests were examined. Once these primary defect populations were identified, two ballistic targets tested under identical conditions with significant differences in performance were selected for detailed study. The rubble from these targets was examined, and size data regarding the defects on the surface of this rubble were collected. The data were fit to distribution functions, and the distributions found on each target were compared. In addition, polished surfaces were prepared to contrast the rubble surface with a random cross section of the material. The distribution functions provided useful insights into the role of microstructural defects in ballistic failure. These insights can be used to advance knowledge of the fundamental dynamic failure mechanisms of armor ceramics.

5.4 Procedure

The quasi-static samples provided to Rutgers by the U.S. Army Research Laboratory (ARL) came in two types, size B bend bars and ring-on-ring plates. In addition, rubble from several depth of penetration (DOP) targets was provided, along with two V50 targets tested under identical conditions. One V50 target resisted the penetrator and was termed the good target. The other target was completely penetrated and was referred to as the bad target. The polished surfaces were created from fragments of both V50 targets. The surfaces of these fragments were diamond-ground and then highly polished.

Each sample was examined with a stereo optical microscope and a field emission scanning electron microscope (FESEM). The optical microscope was attached to a digital camera with software that could image any defect found and directly measure the area of the defect from that image. This microscope was used to find the largest defects and to find the critical flaws on quasi-static samples. The FESEM was used to examine closely the defects found with the optical scope and to find smaller defects difficult to see with an optical scope. The FESEM also had an attached energy dispersive spectroscopy system capable of analyzing the composition of defects found, imaging defects, and directly measuring the area of each defect. The defects found at the failure origins of the quasi-static test specimens were compared with defects found on the rubble surface of the DOP fragments using the same microscopes.

Once the primary defect types were identified, size data regarding the defects were obtained from the rubble of the good target and the bad target. These data were fit to a distribution function found in previous work (*10*) with the following general form:

$$f(a) = \left(\frac{c^{n-1}}{\Gamma(n-1)} \right) a^{-n} e^{\frac{-c}{a}} \text{ ,}$$

(3)

where *c* is a scale parameter, *n* is a shape parameter, and *a* is the radius of the defect as if it were circular. The parameters *c* and *n* were calculated from the data using the maximum likelihood estimation, and *a* was calculated from the area of the defects as measured on the rubble. As most defects are irregular in shape, it was necessary to normalize the data in order to ease fitting them to the distribution function. This was done by calculating the diameter of a circle of equivalent area to the measured defect, then using this diameter to calculate *a*. Once the distribution functions were created, it was possible to measure the strength of the fits and compare the two distributions using the chi-square goodness-of-fit test.

5.5   Results of Preliminary Examination

Two types of inclusions were observed at the failure origins of the quasi-static samples. Many quasi-static samples failed from surface scratches or machining damage, but these were disregarded because interest was on the internal defects produced from processing. An inclusion is a piece of a foreign material imbedded within the host material (*1*, *2*). Inclusions concentrate stresses when there is an elastic modulus mismatch with the host (*2*, *11*, *12*). Significant stresses can also occur when there is a thermal expansion mismatch (*11*, *12*). Generally, an inclusion with a higher thermal expansion than the host will experience circumferential cracking around itself as it attempts to detach from the matrix, while an inclusion with a lower thermal expansion can cause cracks propagating away from the inclusion (*12*). These cracks can then cause failure in subsequent loading. Whether or not this cracking from thermal expansion mismatch occurs is dependent on the size of the inclusion (*12*, *13*). Despite the existence of the stresses, inclusions have to be larger than a critical size before this cracking will occur (*12*, *13*).

One type of inclusion was carbonaceous, and the second type was alumina with iron contamination. The carbon inclusions were often charging in the FESEM, and it was difficult to observe their surface. When they could be imaged without charging, they appeared to have a dark appearance and a powdery, crumbling texture. The alumina inclusions had a rust-like color when viewed optically, but in the FESEM they appeared to be a large-grained ceramic with significant cracking around and within the inclusion. Both of these inclusions are likely caused by sintering aids used to produce dense silicon carbide. Excess carbon is commonly added to remove the silica layer of SiC powder (*14*, *15*), and aluminum-based compounds can be used as sintering aids for SiC (*16*). It was found that the larger ring-on-ring plates had more failures from alumina inclusions than the bend bars, suggesting that a larger-stressed volume is needed

for a significant probability of their occurrence in the test specimen.   Similar types of inclusions were found on the rubble of the DOP targets. The appearance of these inclusions was consistent with the inclusions at the failure origins of the quasi-static samples. It was observed that the carbonaceous inclusions were more common than the alumina inclusions on the rubble, but, in general, the alumina inclusions appeared to be larger. Examples of both types of inclusions are shown in figure 16.

Based on their appearance and on the mechanical properties of graphite, the carbon inclusions would have a significantly lower elastic modulus than dense silicon carbide. This would cause them to act roughly similar to a void in SiC-N. The alumina inclusions should have an elastic modulus very similar to SiC-N, but alumina generally has a higher thermal expansion coefficient than silicon carbide. This thermal expansion mismatch would result in circumferential stresses or cracks forming around the largest inclusions, creating a crack as large as the inclusion. Both of these inclusions are significant defects in SiC-N.

5.6   Distribution of Inclusions on Good and Bad Targets

Having identified two distinct defect types, size data for both inclusions were gathered from the good and bad V50 fragments and fit to the general distribution function. The distributions of both types of inclusion were successfully plotted for each target. The alumina and the carbon distributions were very similar for the two targets. This makes sense, as both targets were produced from the same process. If a part of the process creates carbon inclusions, it makes sense for the overall carbon inclusion distribution coming from that source to be the same in each target. The same applies for the alumina inclusions. An estimate of roughly ~0.04 volume-percent for the carbon inclusion and ~0.24 volume-percent for the alumina inclusions was achieved for the volume fraction of the inclusions from the area fraction on the rubble surface. This indicates that the inclusions are a very small fraction of the material.

A 15% probability that any differences in the alumina inclusion distributions of the targets are only due to variability inherent in statistical sampling was found. This is too high a probability to conclude that the alumina distributions observed are different, based on these distributions. The carbon inclusion distributions are significantly different with a less than 0.4% chance that the two distributions are the same. This indicates that the differences observed in the carbon distributions are indicative of actual differences in the rubble surface distributions. Figure 17 shows the raw size data gathered from the rubble, while figure 18 shows the calculated distribution functions. The reason for the significant difference between the carbon distributions is quite evident in figure 17. On the rubble surface of the good target, twice as many carbon inclusions were found. These additional inclusions consist entirely of inclusions 40 μm or smaller. There are no noticeable differences between the carbon inclusions for the good and bad samples at the larger inclusion sizes.

Figure 16. Images of carbon inclusions viewed in the FESEM (a–d), alumina inclusions viewed in the optical scope (e–f), and the surface of an alumina inclusion viewed in the FESEM (g).

39
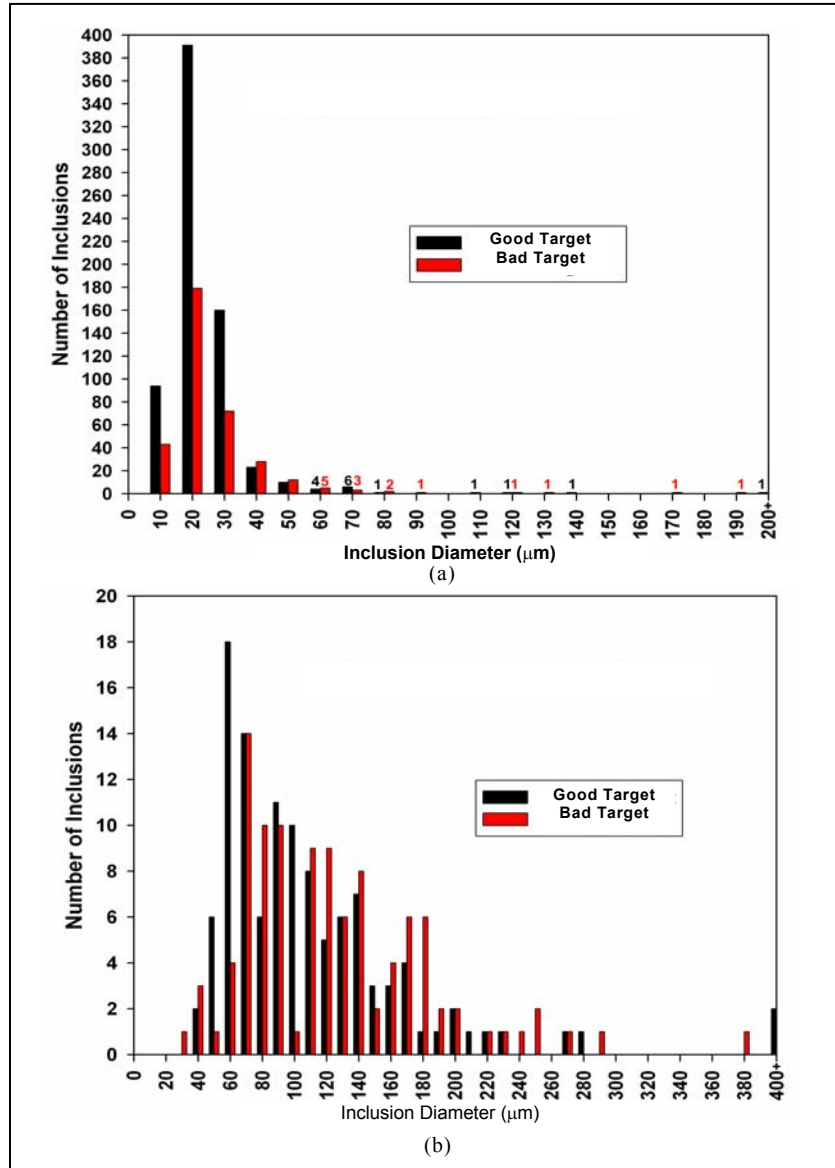
Figure 17.   Raw data of the (a) carbon inclusions and (b) alumina inclusions
found on the rubble surface of the two V50 targets.

Little significant difference between the two targets could be observed when looking at the polished surfaces of both targets. Only very small inclusions (about 1–5 μm) were found for both types. In addition, the area percent of carbon inclusions on the polished surface was ~0.1% for the carbon inclusions and ~0.25%–0.4% for the alumina inclusions, higher than on the rubble surface. This suggests that the smaller inclusions are evenly distributed throughout the material. It also indicates that the large inclusions found on the rubble are too small in volume fraction to have a reasonable probability of observing them on a random cross section. Furthermore, it indicates that fracture is preferentially initiated at the large defects, or the fracture path preferentially passes through the large defects as would be expected for large inclusions with a
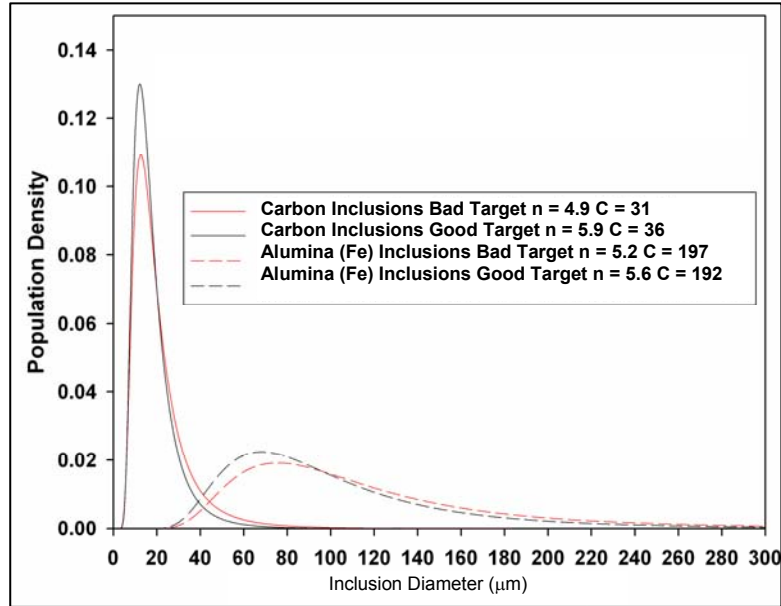
Figure 18. Distribution functions calculated from the raw data of the
inclusions on the rubble.

lower elastic modulus than the matrix. In previous work, it was theorized that a population of defects would serve as nucleation points for fracture during a dynamic event (*7–9*, *17*). The greater the stress and strain rate of the event, the greater the number of defects that will be "activated" during the event (*8*, *9*, *17*). Reviewing the distributions in regard to these ideas, an explanation for the observed distributions is apparent. According to these previous theories, if the good target were subjected to a higher stress than the bad target, there should be more defects at smaller sizes than on the bad target. The defects at the very largest inclusion sizes are so severe that nearly every inclusion of that size should be activated. Therefore, the distributions at the largest sizes should be the same, as both targets should have roughly the same base distributions of inclusions from processing.

This is why the alumina inclusion distributions on the rubble are so similar, but the carbon distributions are different. There are not significant numbers of alumina defects found below 40 μm, where differences become apparent in the carbon distribution. As stated earlier, these alumina inclusions are defects most likely due to cracking from thermal expansion mismatch. At smaller sizes, this cracking is less likely to occur (*12*, *13*). An alumina inclusion with the circumferential cracking should be roughly as severe a defect as an equivalent-sized carbon inclusion; however, but without this cracking they will not be so detrimental and will not initiate fracture. Without any significant data at these smaller flaw sizes, differences between the alumina distributions are too subtle to be detected with the methodology used.

Therefore, it seems that these inclusions are points of fracture during the ballistic event, and the distribution on the rubble surface will be determined by the stress and strain rate of the event. While this concept has been proposed before, this study has provided direct fractographic

41

evidence to support this theory. This concept is illustrated in figure 19. The defect distribution on the good target is indicative of failure at a higher stress because of the presence of numerous smaller defects. The question then is, if these targets were tested under identical conditions, why would they have been subjected to different stresses? The energy imparted into the target should be a function of the mass, velocity, and angle of the projectile.
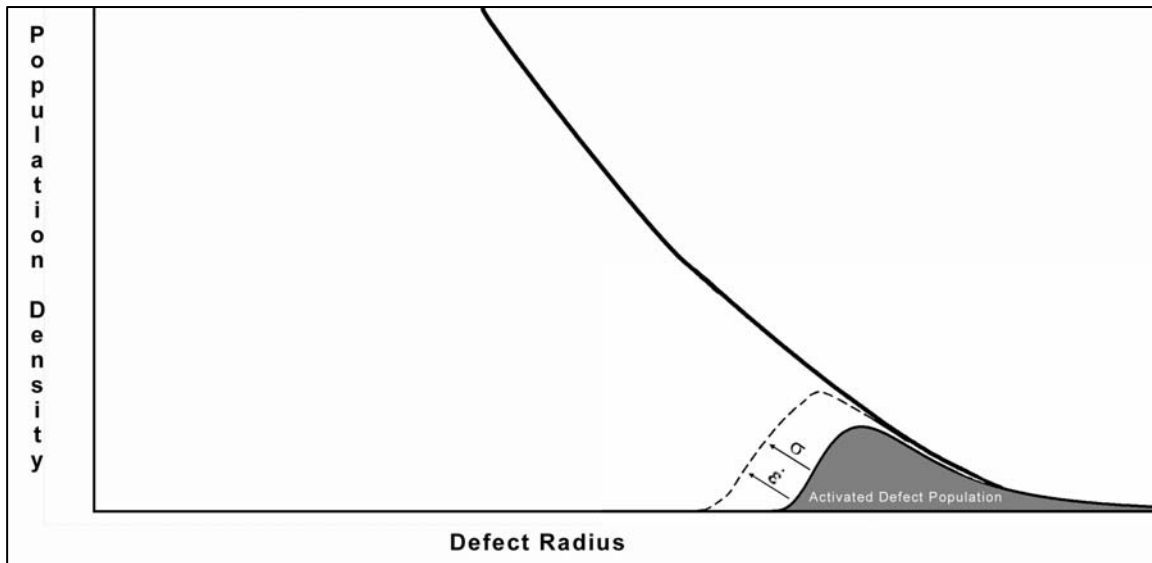
Figure 19. Possible relationship between the stress and strain rate of the impact and the defect population activated.

However, since the good target resisted penetration, it must have absorbed the entire energy of the impact. This should result in a difference in stresses, as the bad target was penetrated and failed to absorb the energy of the projectile. If there were a difference in the stresses reached, the fragmentation of the targets would indicate this. The mass distribution of the remaining fragments of each target was obtained. The good target failed into an overall smaller fragment size, which is consistent with failure at a higher stress. Even though the targets were nominally the same material, an inherent property of the targets caused different responses to identical tests.

It is very possible that the defects are responsible for this difference in performance. While the overall population of defects in the two targets may be very similar, the largest and most severe defects are very few in number. These defects will initiate fracture easily, because their rarity will not be present in the same physical locations in each target. It is possible that large defects in critical locations relative to the impact could influence the resistance of the target when they initiate fracture. In addition, it is possible that differences in the overall defect population between two materials could influence the response.

Unfortunately, how defects influence performance cannot be established with this study. This study has identified that defects are part of the ballistic failure process, and it has established a

probable relationship between the energy absorbed by the target and the defect population initiated. This study cannot claim to have established that defects are the cause of the different response of the targets. However, defects are very likely to be the cause, and with additional experiments and computer modeling it should be possible to define the influence of defects on ballistic performance of ceramics.

5.7 Accomplishments

This study has established that processing defects participate in the ballistic failure process. The distribution of defects that activate is dependent on the stress and strain rate induced in the target. While it is uncertain whether fracture from these defects influences the ballistic performance of the ceramic, it certainly seems plausible that defects may alter the response of the material by serving as fracture initiation points. The role of defects in the failure process must be accounted for if the variability in ceramic armor is to be understood. This will require computer modeling and further testing. Since this work has established that it is possible to plot the distribution of the defects, hopefully the data on defect distributions from this study can be used to assist in the addition of defect populations to computer models.

5.8 References

1. Rice, R. W. Processing Induced Sources of Mechanical Failure in Ceramics. *Processing of Crystalline Ceramics* **1978**, 303–319.

2. Evans, A. G. Structural Reliability: A Processing-Dependent Phenomenon. *Journal of the American Ceramic Society* **1982**, *65* (3), 127–137.

3. Griffith, A. A. The Phenomena of Rupture and Flow in Solids. *Philosophical Transactions of the Royal Society* **1920**, *221*.

4. Irwin, G. R. Onset of Fast Crack Propagation in High Strength Steel and Aluminum Alloys. *Sagamore Conference Proceedings*; Vol. II; Syracuse University Press: Syracuse, NY, 1956.

5. Weibull, W. A Survey of Statistical Effects in the Field of Material Failure. *Applied Mechanics Reviews* **1952**, *5*, 449–451.

6. Weibull, W. A Statistical Distribution Function of Wide Applicability. *ASME Journal of Applied Mechanics* **1951**, 293–297.

7. Grady, D. E. Shock-Wave Compression of Brittle Solids. *Mechanics of Materials* **1998**, *29*, 181–203.

8. Shockey, D. A.; Curran, D. R.; Seaman, L.; Rosenberg, J. T.; Petersen, C. F. Fragmentation of Rock under Dynamic Loads. *International Journal of Rock Mechanics and Mining Sciences, and Geomechanics Abstracts* **1974**, *11*, 303–317.

9. Grady, D. E.; Kipp, M. E. The Micromechanics of Impact Fracture of Rock. *International Journal of Rock Mechanics and Mining Sciences, and Geomechanics Abstracts* **1979**, *16*, 293–302.

10. De, S.; Jayatilaka, A.; Trustrum, K. Statistical Approach to Brittle Fracture. *Journal of Materials Science* **1977**, *12*, 1426–1430.

11. Eshelby, J. D. The Determination of the Elastic Field of an Ellipsoidal Inclusions, and Related Problems. *Proceedings of the Royal Society of London. Series A, Mathematical and Physical Sciences* **1957**, *241* (1226), 376–396.

12. Evans, A. G. The Role of Inclusions in the Fracture of Ceramic Materials. *Journal of Materials Science* **1974**, *9*, 1145–1152.

13. Ito, Y. M.; Rosenblatt, M.; Cheng, L. Y.; Lange, F. F.; Evans, A. G. Cracking in Particulate Composites Due to Thermalmechanical Stress. *International Journal of Fracture* **1981**, *17*, 483–491.

14. Rijswijk, W.; Shanefield, D. J. Effects of Carbon as a Sintering Aid in Silicon Carbide, *Journal of the American Ceramic Society* **1990**, *73* (1), 148–149.

15. Clegg, W. J. Role of Carbon in the Sintering of Boron-Doped Silicon Carbide. *Journal of the American Ceramics Society* **2000**, *83* (5), 1039–1043.

16. Negita, K. Effective Sintering Aids for Silicon Carbide Ceramics: Reactivities of Silicon Carbide with Various Additives. *Journal of the American Ceramic Society* **1986**, *69* (12), C-308–C-310.

17. Adams, M.; Sines, G. A Statistical, Micromechanical Theory of the Compressive Strength of Brittle Materials. *Journal of the American Ceramic Society* **1978**, *61* (3–4), 126–131.

6. Micromechanical Modeling of Advanced Armor Ceramics: Plastic Behavior of Polycrystalline Nanograined Ceramics

(Project initiated January 2001, project completed December 2002)

Core Faculty: G. J. Weng

ARL Collaborators: S. Schoenfeld, T. W. Wright

Johns Hopkins Collaborators: K. T. Ramesh, J.-F. Molinari

Post-Doctoral Associate: B. Jiang

6.1 Objectives

This project had two objectives. The first was to understand how the ductility and strength of ceramics can be enhanced with nanograined microstructures under ballistic impact conditions. The second objective was to identify the optimal grain size and other microstructure features that could ultimately give rise to a longer dwell time for materials used in armored vehicles.

6.2 Key Accomplishments

- Developed a micromechanics-based model of a two-phase composite to study the plastic behavior of nanograined materials

- Showed significant insight into the heterogeneous deformation of a polycrystalline material as the grain size decreased to the nanoscale

- Showed that plastic deformation in a grain and local effective strain in the grain boundary were highly dependent on grain orientation

6.3 Accomplishments

6.3.1 Ceramics

In the early period (1 September 2001–3 December 2001), we developed a micromechanics-based, two-phase composite model to elucidate the distinct features of plastic behavior of nanograined materials. This model was based on the observation that, in a nanograined material, the volume fraction of the grain boundary region is not negligible and, as such, a two-phase model with spherical inclusions representing the grains and a surrounding matrix representing the amorphous grain boundary could be introduced to mimic the heterogeneous microstructure of nanograined materials. The spherical inclusions would possess a grain-size-dependent plastic property, whereas the grain boundary—being amorphous—is a pressure-dependent phase. Then, as the grain size decreases from the traditional coarse-grain to the nanograin regime, the yield stress and the overall stress-strain relations of the material can be

45

calculated. Several important results have been uncovered from this two-phase model including the departure of the yield stress from the linear Hall-Petch equation, a negative slope in the Hall-Petch plot in the nanograined regime, and the tension-compression asymmetry of the plastic behavior. When the deformation of grains is purely elastic as it is in many ceramics, a continuously decreasing, negative slope was also found in the yield-strength dependence of the grain size, approaching asymptotically the yield strength of the grain-boundary phase.

During the period of 1 January 2002–31 June 2002, we developed a truly grain-based model for the polycrystal. A total of 108,000 grains with different orientations have been introduced in the polycrystal model. Their orientations are characterized by uniform rotations of the Euler angles in the 3-D space to generate an isotropic distribution. Each grain was embedded in the amorphous grain boundary, and its plastic behavior was calculated from the crystallographic slips of active slip systems. The plastic behavior and elastic behavior of each grain is anisotropic. In order to take into account such an anisotropy, an equivalent eigenstrain was determined for each grain, and then put into a generalized self-consistent (GSC) framework. The plastic state of the grain boundary associated with each grain is different because of the different plastic deformation in the oriented grains. As the effective medium of the GSC must represent the volume-averaged behavior of all constituent grains and their respective surrounding grain boundaries, a highly iterative numerical scheme is involved. When the plastic state varies from grain to grain in a self-consistent fashion, the computations are highly coupled and nonlinear. This calculated heterogeneous plastic state of the grain-boundary regions associated with all 108,000 grains served as input into the iterative scheme until the inputs and outputs were fully consistent with each other for the final solutions. A computer program has been successfully developed to handle this implicit, iterative procedure. Comparison between the theoretical and experimental results suggests that the theoretical model is able to capture the essential features of the stress-strain behaviors of a nanograined material. When the grain size is larger than 20 μm, the slope of the Hall-Petch obtained by this model is almost the same as that of the traditional Hall-Petch equation. Using this model, we also determined the distributions and evolutions of plastic deformation in the grains and in the grain boundary associated with each oriented grain. We also found that for nanograin-sized material, initial plastic deformation of the polycrystal is contributed mainly by the grain boundaries.

In this semiannual period (1 July 2002–31 December 2002), we developed a multiphase micromechanics composite model with pores to analyze the features of plastic behavior of nano-grained ceramics, and we used it to determine influence of second phase and porosity on the yield stress. The development was motivated by the observations that porosity is almost present even in nanograined ceramics (1), and that multiphase microstructure could be essential in order to develop high-ductility, superplastic nanoceramics (2). The influence of pores and other phases on the overall plastic properties of nanograined ceramics is significant. We have developed a multiphase generalized self-consistent scheme during this period that can account

46

for the influence of porosity and second phases on the plastic behavior of nanoceramics as the grain size decreases from the coarse grain to the nanograin regime. In this model, the ceramic grains of all phases are embedded in amorphous grain-boundary regions, and pores are further embedded in the effective medium. This approach can simulate the cases of pores being either in the grains or in the grain boundaries. The grain size may decrease from the traditional coarse-grain to the nanograin regime, and the yield stress and the overall stress-strain relations of the multiphase material with pores can be calculated. This model can consider the interactions among pores, phases, grains, and grain boundaries. Figure 20 shows the comparison between this developed theory and the experimental results of TiO_2 as obtained by this multiphase model. Excellent agreement between the two is observed. It is seen that the yield stress initially increases, and then decreases as the grain size decreases to the nanorange. The presence of pores lowered the yield strength of TiO_2 further. This comparison suggests that our model can capture the essential features of nanograined ceramics with pores. At a given porosity, the transition from a positive slope of Hall-Petch type to a negative one still exists in this nanograined ceramic. With increased porosity, the critical grain size that marks the transition is found to move to a larger grain size (moves to the left in figure 20). The effect of second phase on yield stress of ceramics is shown in figure 21. The following four cases were considered: (1) there is no second elastic phase, (2) there is a 10 volume-percent s elastic phase where the elastic modulus is the same as that of ceramic phase, (3) there is a 10 volume-percent s elastic phase where the elastic modulus is larger than that of grain boundary but smaller than that of ceramic phase, (4) there is a 10 volume-percent s elastic phase where the elastic modulus is larger than that of ceramic phase. All samples have 6 volume-percent pores and the elastic modulus of ceramic phase is larger than that of grain boundary. The elastic phase means that plastic deformation does not take place in that phase. These calculations point to the fact that, by adding other elastic grains, the compressive yield stress of the two-phase ceramic can be greatly affected. Before the grain size decreases to the critical value at which the yield strength is at its maximum and the transition occurs, soft and hard second-phase elastic grains can increase the compressive yield stress of the two-phase ceramic. However, after it decreases below this value, only softer second elastic phase can cause the yield stress to decrease. We also analyze the effect of grain-boundary thickness on the yield stress of the ceramics; the results are shown in figure 22. It was found that the grain-boundary thickness has very little effect on the yield stress prior to the attainment of the critical grain size, but after that greater grain-boundary thickness will significantly lower the yield stress of the nanograined ceramic.
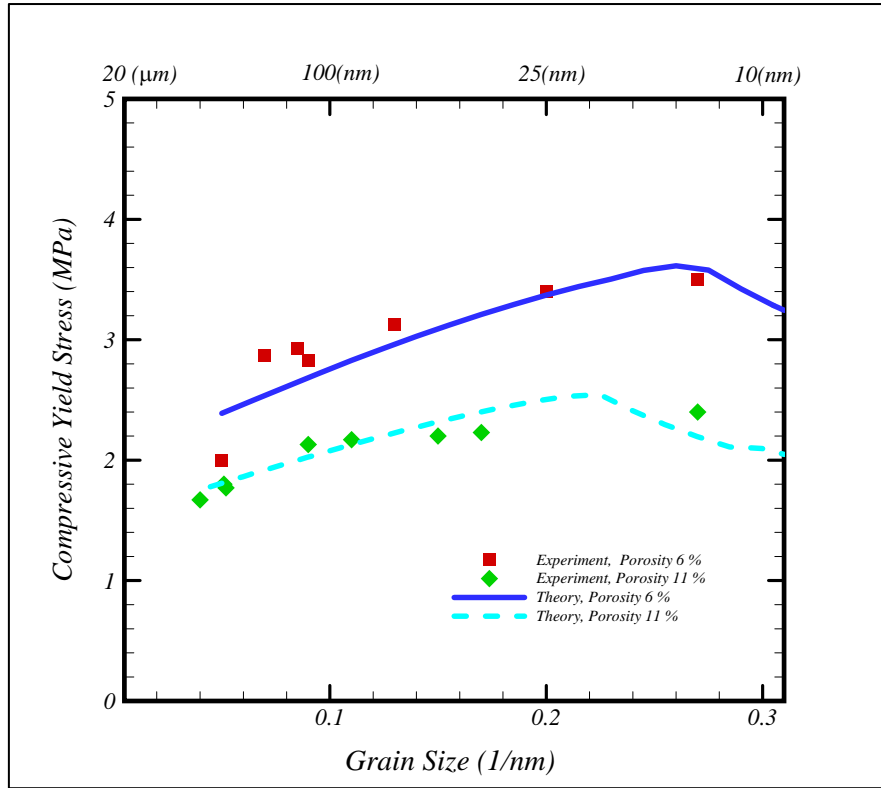
Figure 20. Experiment and theory: yield stress, grain size, and porosity.
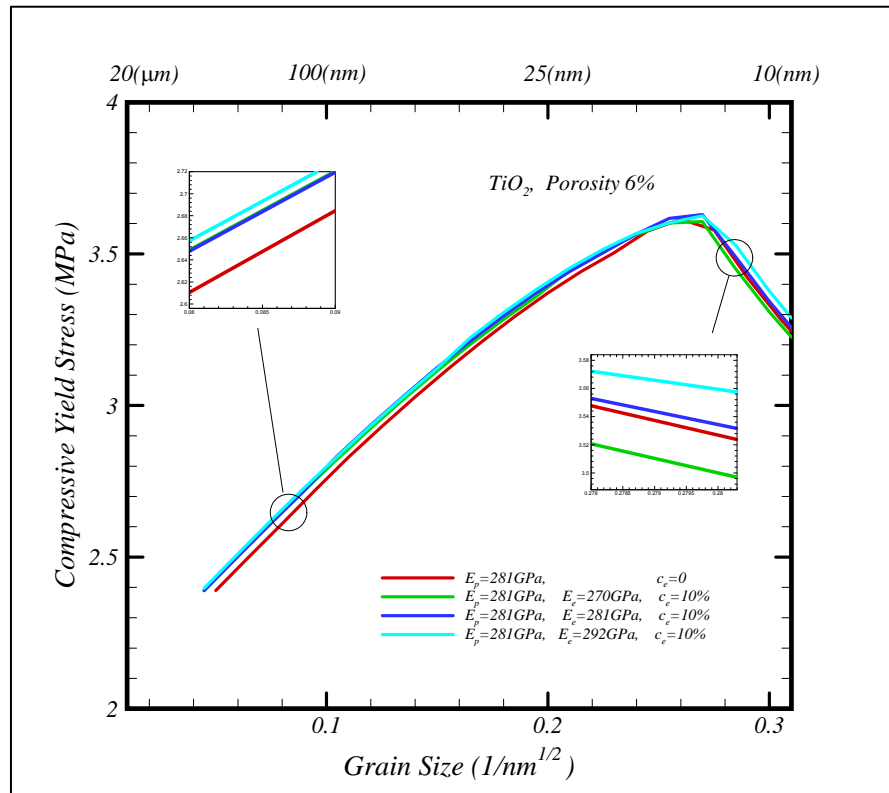
Figure 21. Effect of the elastic grain on compressive yield stress of TiO₂ ceramics.
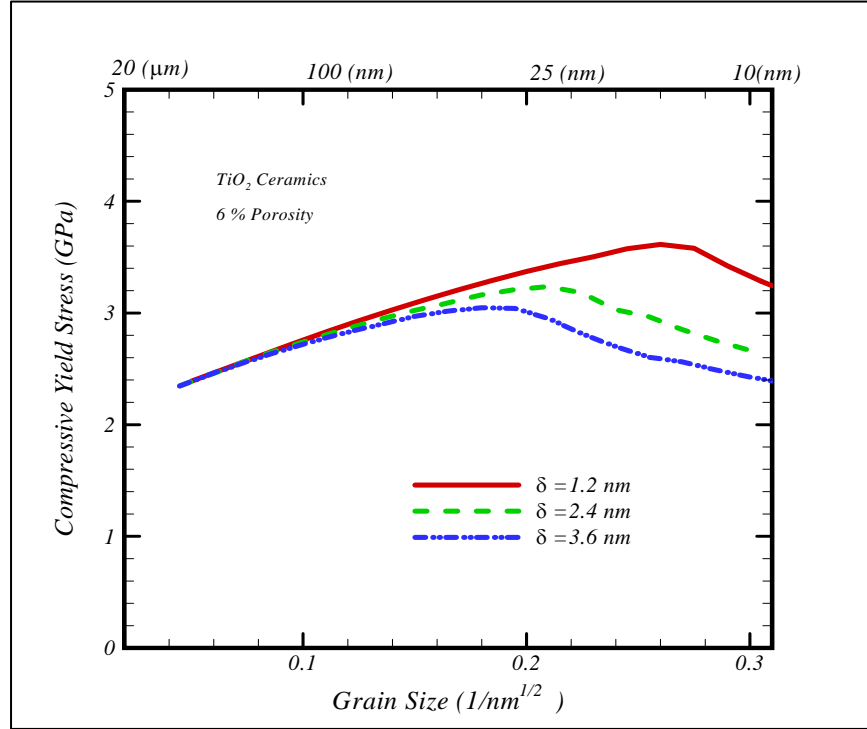
Figure 22. Effect of thickness of grain boundary on compressive yield stress
of TiO_2 ceramics.

6.3.2 Metals

A micromechanics-based, two-phase composite model was developed to elucidate the distinct
features of the plastic behavior of nanograined materials. This model was based on the
observation that, in a nanograined material, the volume fraction of the grain-boundary region is
not negligible. As such, a two-phase model with spherical inclusions representing the grains and
a surrounding matrix representing the amorphous grain boundary could be introduced to mimic
the heterogeneous microstructure of nanograined materials. The spherical inclusions would
possess a grain-size-dependent plastic property, whereas the grain boundary—being
amorphous—is a pressure-dependent phase. Then, as the grain size decreases from the
traditional coarse-grain to the nanograin regime, the yield stress and the overall stress-strain
relations of the material can be calculated. Several important results were uncovered from this
two-phase model, including the departure of the yield stress from the linear Hall-Petch equation,
a negative slope in the Hall-Petch plot in the nanograined regime, and the tension-compression
asymmetry of the plastic behavior. When the deformation of grains was purely elastic, as it is in
many ceramics, a continuously decreasing, negative slope was also found in the yield-strength
dependence of the grain size, approaching asymptotically the yield strength of the grain-
boundary phase.

49

A truly grain-based model was developed for polycrystals. Twenty-seven thousand gr with different orientations have been introduced in the polycrystal model. Their orientations were characterized by uniform rotations of the Euler angles in the 3-D space to generate an isotropic distribution. Each grain was embedded in the amorphous grain boundary, and its plastic behavior was calculated from the crystallographic slips of active slip systems. The plastic behavior and elastic behavior of each grain is anisotropic. To take into account such an anisotropy, an equivalent eigenstrain was determined for each grain and then was put into a GSC framework. The plastic state of the grain boundary associated with each grain was different because of the different plastic deformation in the oriented grains. As the effective medium of the GSC represented the volume-averaged behavior of all constituent grains and their respective surrounding grain boundaries, a highly iterative numerical scheme was involved. When the plastic state varies from grain to grain in a self-consistent fashion, the computations were highly coupled and nonlinear. This calculated heterogeneous plastic state of the grain-boundary regions associated with all 27,000 gr served as initial inputs into the iterative scheme until the inputs and outputs were fully consistent with each other for the final solutions. A computer program was successfully developed to handle this implicit, iterative procedure.

The developed theory can be used to study the plastic behavior of nanocrystalline polycrystal metals and nanocrystalline polycrystal ceramics as the grain size decreases from the coarse-grain to the nanometer range. To test the validity of the developed theory, it was applied to predict the tensile stress-strain relations of a copper as its grain size decreases from 20 μm to 26 nm. The results were compared with the experimental data of Sanders et al. (3). The test results at four grain sizes, d = 26, 49, and 110 nm and 20 μm, are reproduced in figure 23 (a) and the theoretical results are given in figure 23 (b). Comparison between the two suggests that the theoretical model was able to capture the essential features of the stress-strain behaviors of a nanograined material. During this range of grain size, it was particularly evident that the plastic strength of the material steadily increased as the grain size decreased to the nanometer scale. However, it was also noted that the increase in the later stage of grain-size reduction was not as prominent as in the early one with coarse grains. The calculations showed a smooth transition in the stress-strain curves of the nanograined polycrystals from the elastic to the plastic state. This was due to the gradual yielding process of the constituent grains, a feature that was not attainable in the simple two-phase model, where the spherical inclusions would either yield or not yield, and a sharp turn of the stress-strain curve was unavoidable.

The calculations yielded significant insights into the heterogeneous deformation of the polycrystal as the grain size decreased from coarse grain to the nanoscale. Figure 24 shows the distribution and evolution of effective plastic strain with oriented grains with sizes at 20 μm, 110 nm, and 26 nm. In each figure, the distributions of effective plastic strains are given when the overall plastic strain of the composite, ε_{33}^p, is 0.001, 0.002, 0.003, 0.005, 0.01, and 0.015, in turn. For a coarse-grain-size material, initial plastic deformation of polycrystal comes mainly from that in the grains. However, for a nanograined-size material, initial plastic deformation of
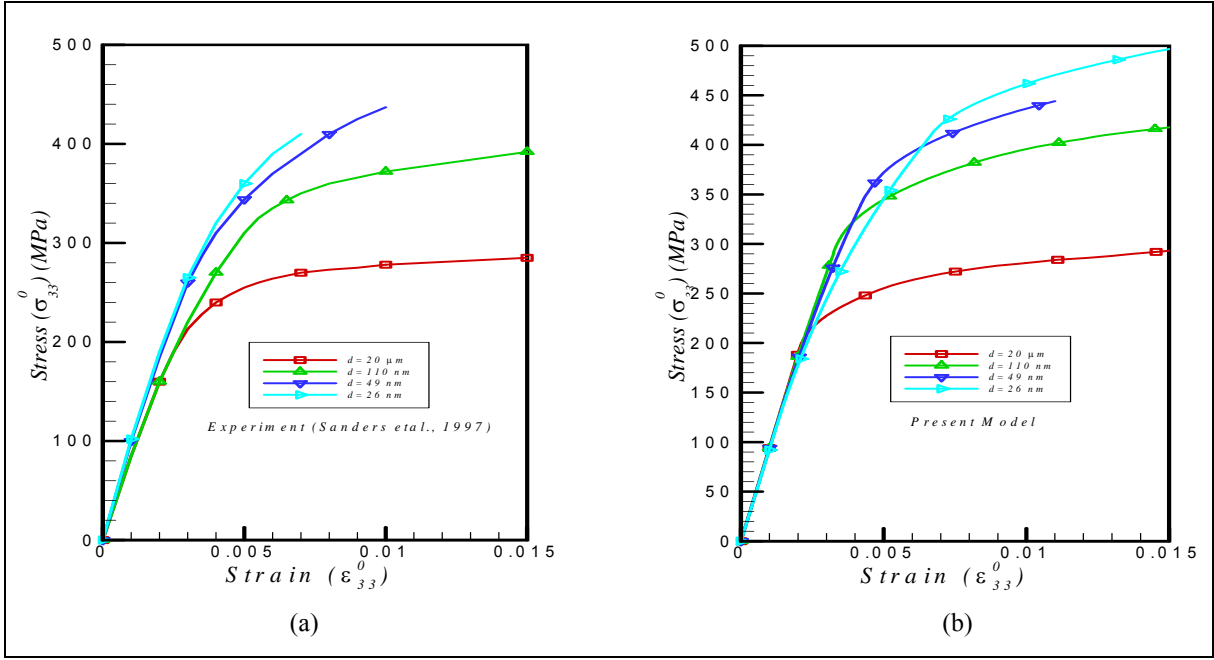
Figure 23. Tensile stress-strain relations of copper as function of grain size d: (a) experimental data of Sanders et al. (*3*) and (b) theoretical predictions.

the polycrystal is contributed mainly by the grain boundaries. We further used the theory to evaluate the effective stress of the surrounding matrix for each grain. Figure 25 shows the distributions and evolutions of the effective stress in grain boundaries associated with oriented grains. When some grains had no plastic deformation, the distribution of the effective stresses was uniform; otherwise, it became nonuniform. One of the most interesting features was that plastic deformation in a grain reduces the effective stress in the grain boundary surrounding it. The grain-boundary region associated with the 45° orientations of the two Euler angles under a uniaxial tension or compression was found to be in the most severe plastic state (figure 25). Such a plastic heterogeneity of the grain-boundary region surrounding a particular grain was also not available with the simple two-phase model.

The distribution and evolution was given for local effective strain in the grain boundaries associated with some specifically oriented grains at $\theta = \psi = 0^{0}$, $\theta = 45^{0}, \psi = 0^{0}$, and $\theta = \psi = 45^{0}$. It is seen from figure 26 (a) that the grain boundary associated with the grain at $\theta = \psi = 0^{0}$ possesses an effective strain that is independent of Ψ but dependent of Θ. The largest effective strain was in the grain boundary associated with $\Theta = 45°$ and $\Theta = 135°$. In the first two figures of figure 26, there was no plastic deformation in the grain. When plastic deformation takes place in the grain, the distribution of the local effective stain does not change except for its magnitude. This is because plastic deformation caused by the applied stress in the grain boundary is so large that it shields the effect of plastic deformation in the grain on the grain boundary. However, for the grain boundary associated with the grain at $\theta = 45°$, $\Psi = 0°$, the

51

situation was different. Figure 26 (b) shows that as plastic deformation became more pronounced in the grain, the local effective strain in the grain boundary also changed drastically. This implies that the effect of plastic deformation in the grain on the local effective strain of the grain boundary was very significant. However, the effect of plastic deformation in the grain on the distribution of effective strain in the grain boundary is not significant for the grain boundary associated with the grain at $\theta = \Psi = 45°$, as shown in figure 26 (c). These behaviors indicate that the effect of plastic deformation in the grain on the local effective strain in the grain boundary was highly dependent upon the orientation of the grain.
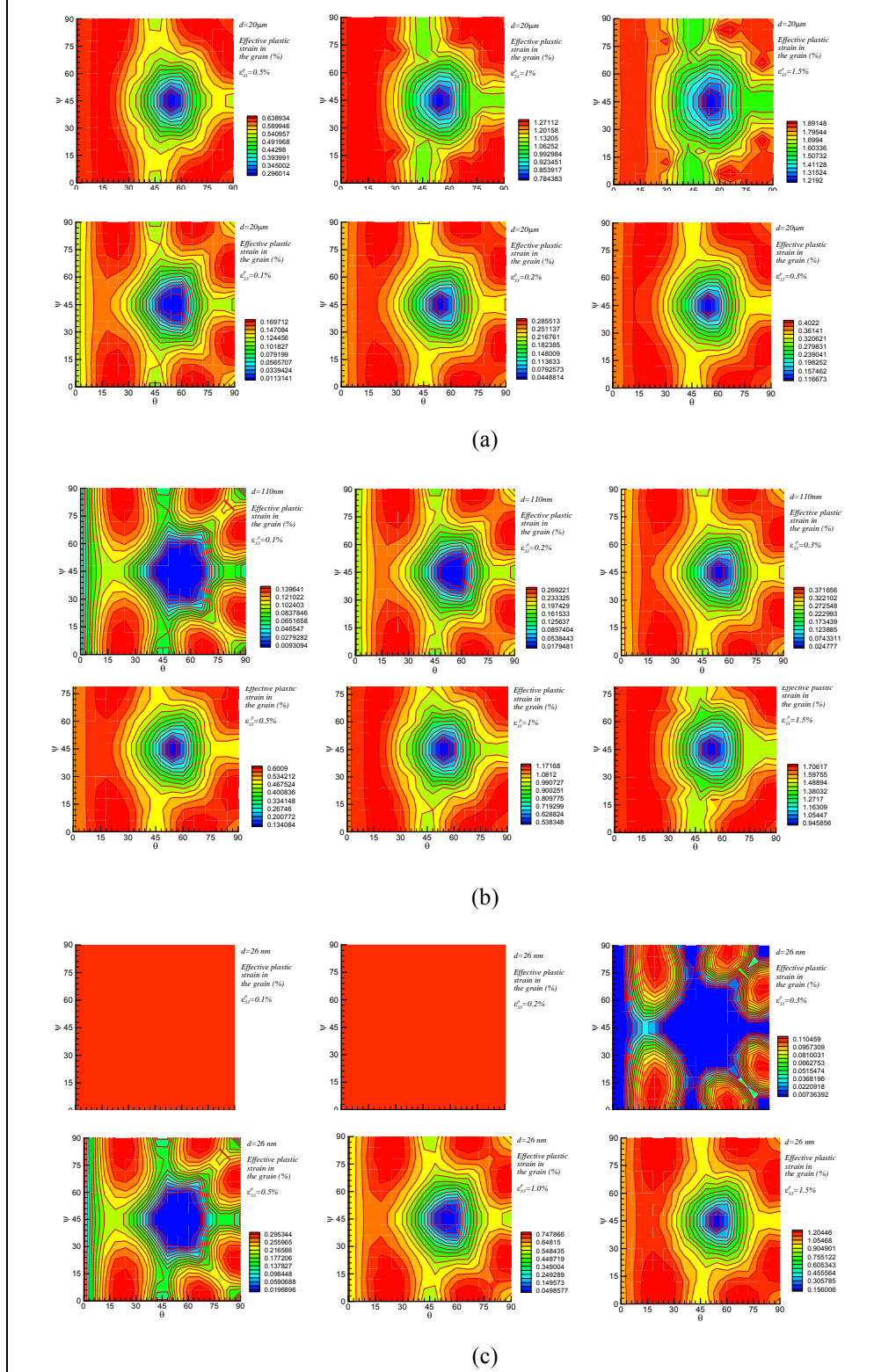
Figure 24. Distribution and evolution of effective plastic strain of oriented grains whose grain size is (a) 20 µm, (b) 110 nm, and (c) 26 nm.
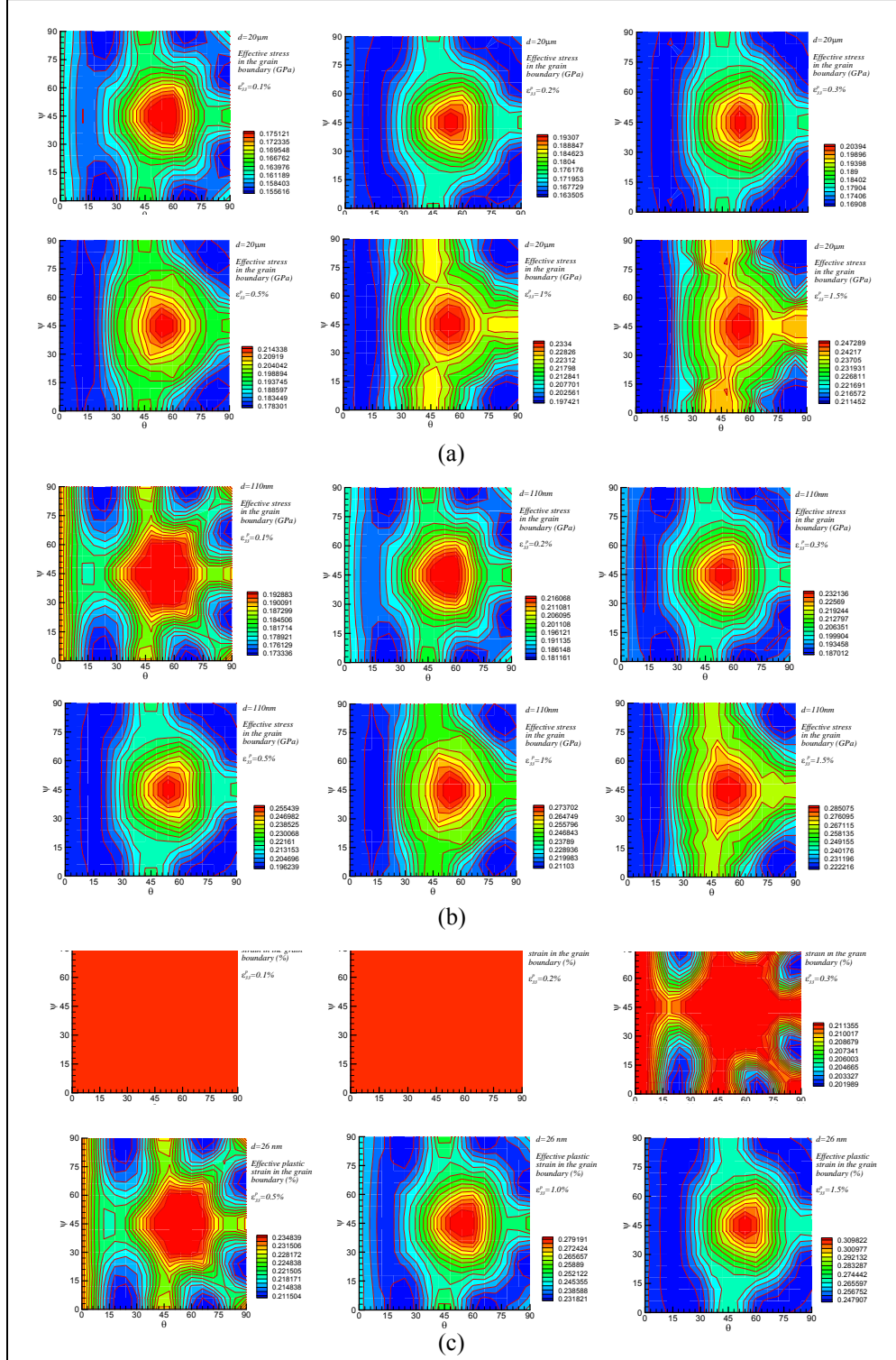
Figure 25. Distribution and evolution of effective stress in grain boundaries with oriented grains whose grain size is (a) 20 μm, (b) 110 nm, and (c) 26 nm.
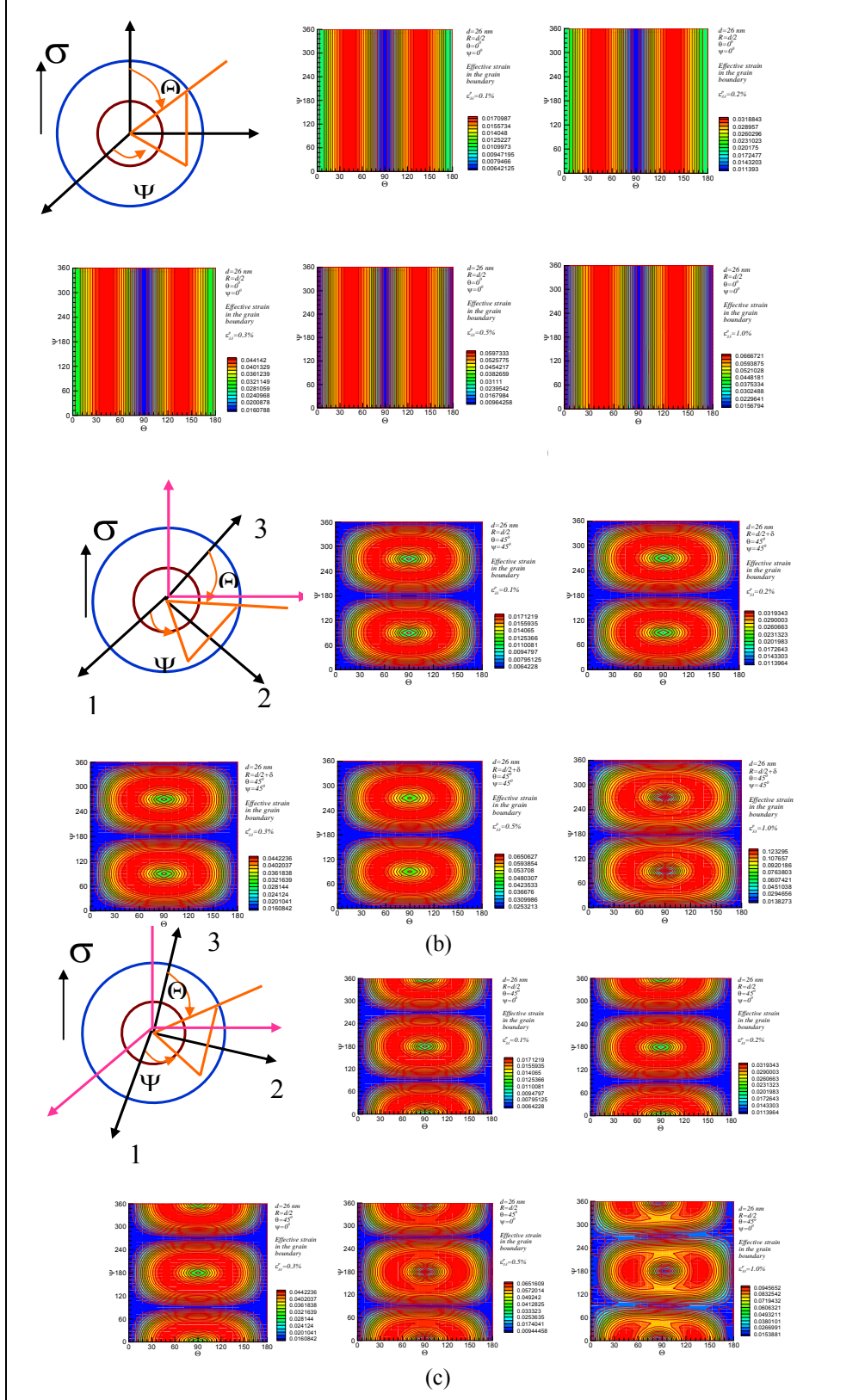
Figure 26. Local effective strain in the grain boundary associated with an oriented grain at
(a) $\theta = \Psi = 0°$, (b) $\theta = 45°$ and $\Psi = 45°$, and (c) $\theta = \Psi = 45°$. Grain size is 26 nm.

6.4 References

1. Averback, R. S.; Hofler, H. J.; Hahn, H.; Logas, J. C. Sintering and Grain Growth in Nanocrystalline Ceramics. *Nanostructured Materials* **1992**, *1*, 173–178.

2. Kim, B. N.; Hiraga, K.; Morita, K.; Sakka, Y. A High-Strain-Rate Superplastic Ceramic. *Nature* **2001**, *413*, 288–291.

3. Sanders, P. G.; Eastman, J. A.; Weertman, J. R. Elastic and Tensile Behavior of Nanocrystalline Copper and Palladium. *Acta Mater*. **1997**, *45*, 4019.

7. Silicon-Carbide Process Improvements for Improved Homogeneity and Reproducibility

(Project initiated June 2004, completed December 2005))

Core Faculty: R. Haber, D. Niesz

ARL Collaborators: J. McCauley, E. Chin, and J. Adams

Graduate Student: C. Ziccardi

Undergraduate Students: T. Terrell, J. Pantina

7.1 Objectives

- To develop a better understanding of the relationship between microstructural quality and ballistic performance for silicon-carbide armor

- To demonstrate that improved microstructural quality produces higher Weibull modulus on large SiC samples and results in improved ballistic performance

- To quantify the effect of coarse particle inclusions and anomalous porosity on the Weibull modulus and ballistic performance of fine-grain-size, hot-pressed SiC

7.2 Accomplishments

- Enhanced green density for SiC compacts

- Achieved >99% dense of hot-pressed SiC

- Improved fired microstructure with fine grain size

- Developed an aqueous additive approach to introduce B and C sintering aids

7.3 Introduction

Currently available commercial silicon-carbide armor materials exhibit a high variability in their ballistic performance. DOP variations as high as a factor of 8 on nominally identical tiles have been observed for SiC, typically with variations of a factor of 2.5. Although this high variability may be partially attributable to the ballistic test, most of it has been attributed to the silicon-carbide armor material. While the fundamental cause of this variability has not been identified, this variability may be caused by microstructural defects, plastic deformation mechanisms, or a combination of both.

Microstructural defects are known to be present in commercial silicon-carbide armor materials. These include isolated pores, porous areas, large grains, variation in grain-boundary composition from nonuniform distribution of impurities or hot-pressing aids, and inclusions of foreign material. These defects lead to a variation in quasi-static strength and may be related to variation in ballistic performance. Microstructural defects can be separated into two classes. The first class includes the normal distribution of high-frequency defects, such as small, isolated pores and large grains, which cause the strength variation that determines the Weibull modulus obtained from bending strength data from four-point bend tests on standard-size specimens (*1*).

The second class can be considered anomalous defects and includes pores that are much greater than the grain size, foreign inclusions, and a very low percentage of porous areas within a dense matrix. These anomalous defects are often present in such a low-volume percentage that they are often not detected in general microstructural examination on a random polished surface or the fracture surface of a standard four-point bend specimen. These low-probability critical defects are usually assumed to be insignificant in regard to ballistic penetration, since silicon carbide exhibits extensive cracking prior to ballistic penetration. However, this assumption has not been tested either experimentally or analytically. Thus, these anomalous defects may affect ballistic performance if, for example, they initiate macroscopic cracking early in the ballistic event.

Perhaps the best evidence of the importance of microstructural quality on ballistic performance is the results of Krell on alumina (*2*). He reported a 50% improvement in ballistic performance over Coors AD 995. The microstructural quality of his material is demonstrated by its transparency. Transparency requires a density of at least 99.99% of theoretical density and a grain size significantly less than 0.5 μm. The hardness of his material correlated with porosity and grain size, as would be expected, and also with ballistic performance. Similar improvements in the ballistic performance of silicon carbide would be expected with similar improvements in microstructural quality over current commercial materials.

7.4   Accomplishments

Initially, the particle size distributions of several commercial powders were evaluated. The results are shown in figure 27.

The Superior Graphite 490 powder was then beneficiated by settlings and decanting to remove the large particles. The results of these beneficiations are shown in figure 28.

Green powder compacts were prepared by filter-pressing at 0.41 MPa and repressing the wet compact in a die at 6.8 MPa with filter paper on the top and bottom of the sample. Repressing in the plastic state removes large pores formed by water flow channels, and it increases the green density by forcing excess water into the filter paper. Figure 29 shows a scanning electron micrograph (SEM) of a green microstructure of a compact prepared by this process using Superior Graphite 490 powder that had been twice beneficiated by settling and decantation.
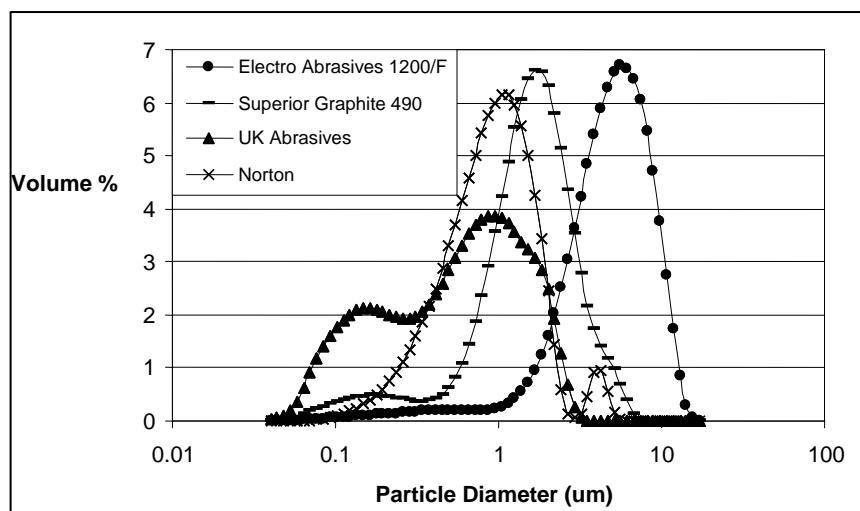
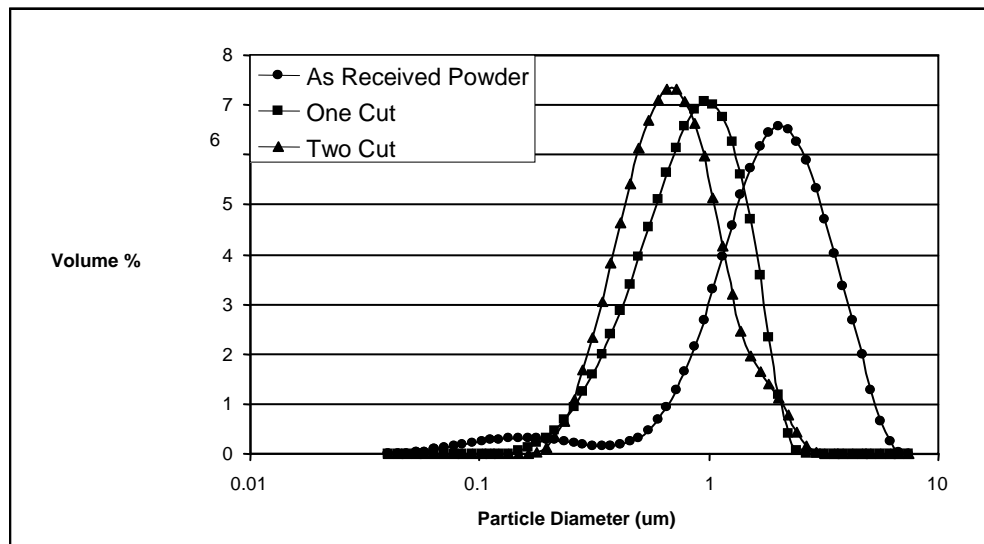Figure 27. Particle size plots for as-received powders.

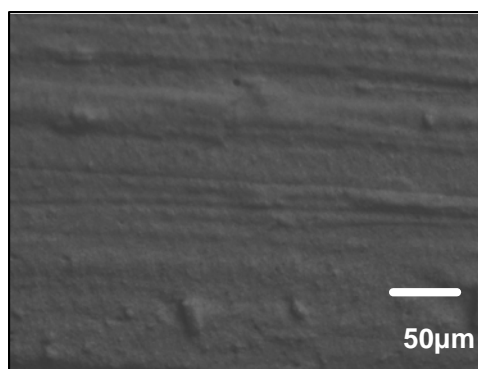Figure 28. Particle size distributions of Superior Graphite 490 powder after beneficiation.

Figure 29. SEM of a filter-pressed and
wet-pressed sample of SiC.

59

This sample has a higher green density and a much higher-quality green microstructure than compacts formed from the as-received powder by dry-pressing. Green compacts formed from beneficiated powder by this process have excellent reproducibility. The high-quality of green compacts made by this process enables pore free, fine-grained SiC to be prepared by hot-pressing. An aqueous-based B and C surfactant was developed that resulted in dense, fine-grained microstructures.

Hot-press runs have shown consistently dense SiC samples with densities ranging from 3.19 to 3.21 g/cm^3. Figure 30 shows an SEM micrograph of a fracture surface of a hot-pressed sample prepared using the Norton SIC powder (see figure 27) containing 3.5% Huntsman HX1 sintering aid. (The Huntsman HX series of additives were the boron- and carbon-based alkylene amines used in this study.) The green compact was formed by filter-pressing and wet-pressing prior to hot-pressing at 2300 °C for 15 min. This sample had a 2–4-μm grain size with no observable porosity. The final density was 3.20 g/cm^3.
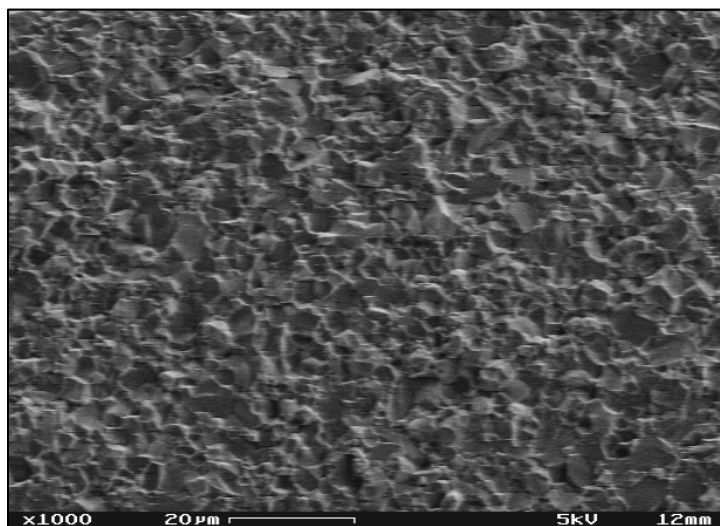
Figure 30.   Fracture surface of the processed SiC containing Norton SiC and Huntsman HX1 sintering aid. A 2–4-μm grain size is shown. No porosity is observed.

Table 3 shows the maximum densities for the various additives used. Samples were formed by either dry-pressing or filter-pressing and repressing (wet-pressing) before loading in a die for hot-pressing. The additives listed next—H3, H4, H5, H6, and H7—contain different boron percentages doped in an ethylene amine-based hydrocarbon surfactant. Additionally, H5, H6, and H7, while similar in B/C ratio to H3 and H4, had slightly different surfactant adsorption characteristics. These were chosen to determine whether higher percentages of B could be adsorbed on the SiC particles and remain in filter-pressed cakes. The percentage of B within the additives H3-H7 ranged from 2.8% to 3.7%.

Table 3. Densities of hot-pressed samples with various additives.

Dry or Filter	Additive	Density (g/cm^3)
Dry	0.077% boron and 1.56% carbon and 0.5% B4C	3.2
Dry	0.044% boron and 0.89% carbon	2.91
Dry	0.055% boron and 1.11% carbon	3.08
Dry	0.088% boron and 1.78% carbon	3.02
Dry	0.099% boron and 2% carbon	3.2
Dry	0.096% boron and 1.25% carbon	3.19
Dry	0.112% boron and 1.45% carbon	3.18
Dry	0.128% boron and 1.66% carbon	3.15
Dry	0.144% boron and 1.87% carbon	3.2
Dry	0.13% boron and 1.56% carbon	2.91
Dry	0.222% boron and 2.67% carbon	3.12
Dry	0.112% boron and 1.56% carbon	2.76
Dry	0.192% boron and 2.67% carbon	3.14
Dry	0.174% boron and 2.67% carbon	3.18
Filter	0.192% boron and 2.67% carbon	2.49
Filter	0.256% boron and 3.32% carbon	2.46
Filter	0.32% boron and 4.15% carbon	2.61
Filter	0.132% boron and 2.67% carbon	2.35
Filter	0.176% boron and 3.56% carbon	2.37
Filter	0.22% boron and 4.45% carbon	2.43
Filter	0.259% boron and 3.115% carbon	2.64
Filter	0.37% boron and 4.45% carbon	2.73
Filter	0.224% boron and 3.115% carbon	2.58
Filter	0.32% boron and 4.45% carbon	2.41
Filter	0.203% boron and 3.115% carbon	2.71
Filter	0.29% boron and 4.45% carbon	2.58

Knoop hardness measurements were made on some of the samples shown in table 3. Figure 31 shows the hardness values for applied loads from 100–2000 g. All values are from 10 indents; error bars are excluded to make reading the graph simpler. It should be noted that the maximum hardness values achieved are 20% higher than for a commercial armor material. Figure 32 shows the hardness values of samples exhibiting the highest Knoop hardness, as compared with SiC-N. H3 and H4 show a similar 20% improvement in the Knoop hardness.

Rutgers SiC Hardness Data
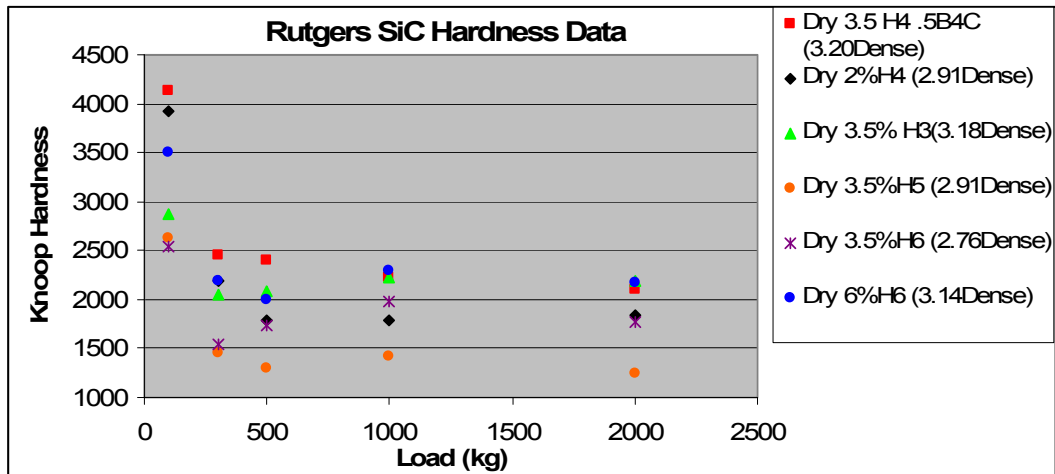
Figure 31. Hardness values for hot-pressed SiC samples.

A series of samples were prepared to study the effect of adding excess carbon to the SiC powder. In this study, 0% to 5% super additions of carbon were added the base composition that gave a hot-pressed density >99% of theoretical density. Knoop hardnesses of the hot-pressed samples were evaluated. Figure 33 shows the effect that these super additions had on hardness.

Knoop Hardness Plot
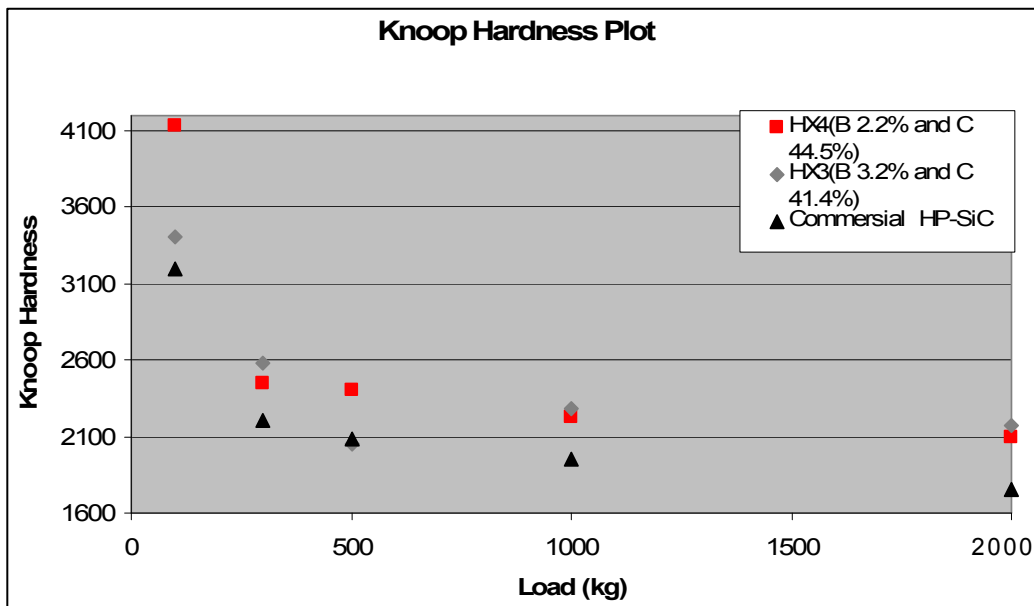
Figure 32. Knoop hardness for SiC material fabricated in this study compared to a commercially hot-pressed SiC armor material.

Samples with a larger grain size were also prepared. This was done to study the effect of grain size on density and microstructural uniformity. Initial data showed that the hardness drops with increasing grain size, which supports the work of Krell on alumina (*2*).

These micrographs show an increase in carbon inclusions with the increase in excess carbon. Figure 34 shows the "potato chip" defect reported in the ballistic rubble in SiC-N ballistic rubble. (Refer to section 5 of this report.) The defect shown for the 5% super addition of carbon in figure 35 looks very similar to the one reported for SiC-N.
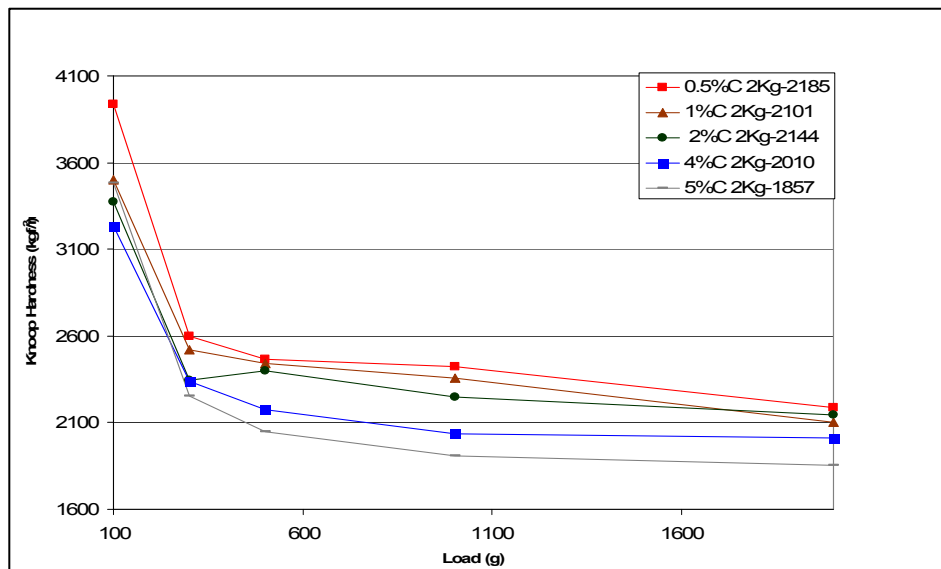
Figure 33. Hardnesses as a function of load for various super additions of carbon.

7.5 Recommendations for Future Work

1. The microstructures should be evaluated for samples hot-pressed with super additions of carbon above the theoretical amount required to remove the SiO_2. These samples should also be evaluated by ultrasonic imaging to obtain a more complete evaluation of the carbon inclusions.

2. Additional samples should be fabricated with intentional additions of coarse (>5 µm) particles in the green microstructure. These samples should then be hot-pressed and evaluated for density, hardness, and microstructural uniformity.

3. Samples exhibiting the highest density and greatest microstructural uniformity should be fabricated into tiles for ballistic testing.
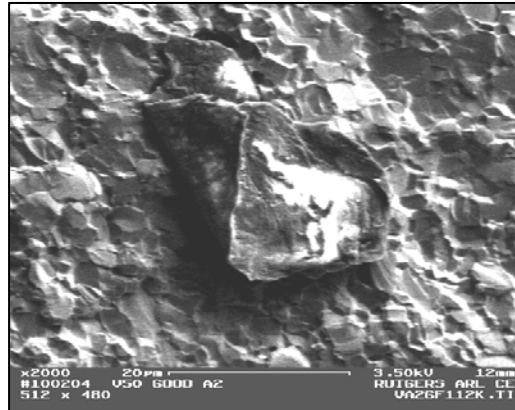
Figure 34. Potato-chip defect.
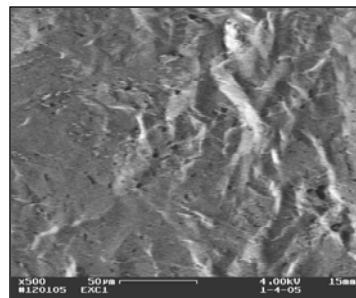
(A-0% Carbon)
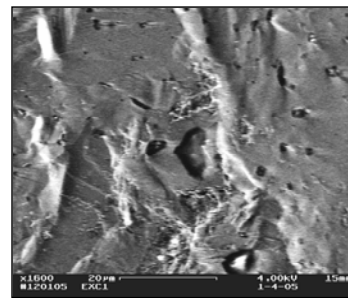
(B-1% Carbon)
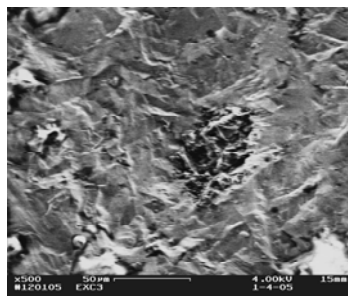
(C-2% Carbon)
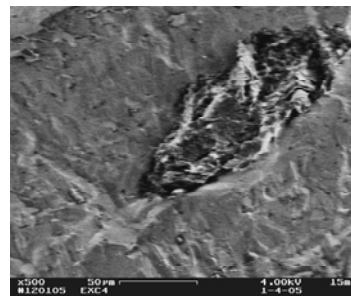
(D-4% Carbon)
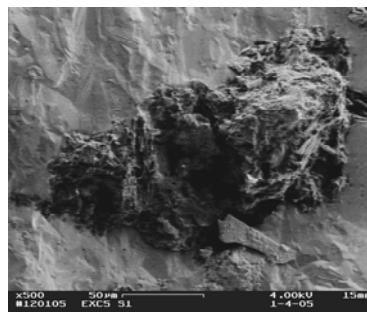
(E-5% Carbon)

Figure 35. SEMs of SiC with 1%–5% super additions of carbon.

7.6 References

1. Bakas, M. P.; Greenhut, V. A.; Niesz, D. E.; Quinn, G. D.; McCauley, J. W.; Wereszczak, A. A.; Swab, J. J. Anomalous Defects and Dynamic Material Properties in the Performance. *International Journal of Applied Ceramic Technology* **2004** *1* (3), 211.

2. Krell, A. Processing of High-Density Submicron Al_2O_3 for New Applications. *J. Am. Ceram. Soc.* **2003**, *86* (4), 546–553.

8. NDE of Ceramic Armor

(Project initiated March 2004, completed December 2005)

Core Faculty: R. Haber, D. Niesz

ARL Collaborators: J. McCauley, J. Adams

Graduate Student: R. Brennan

Undergraduate Student: E. Armstrong

8.1 Objectives

- Determine the feasibility of utilizing high frequency ultrasound C-scan imaging and quantitative analysis for NDE of high-density bulk ceramic armor

- Determine the limits and optimize the conditions necessary for nondestructively detecting micrometer-size and larger defects in bulk ceramic armor

- Develop a method for quantitative analysis of ultrasound data for evaluation and comparison of bulk ceramic armor material integrity

- Develop a method for using high-frequency ultrasound to establish a representative materials "fingerprint" that will describe microstructural features, including defect input data that can be quantified and applied to property, design, and performance modeling and simulation

8.2 Key Accomplishments

- Developed high-frequency ultrasound system at Rutgers University for pulse amplitude and time-of-flight (TOF) C-scan imaging and analysis of various defects in ceramic armor plates

- Established importance of ultrasound transducer frequency for detecting and locating defects and features of various size, shape, orientation, and acoustic impedance by demonstrating C-scan imaging capabilities at different frequency conditions

- Developed quantitative analysis technique for evaluating and comparing ceramic armor samples of various material integrity by utilizing normalized histograms to analyze amplitude and TOF distribution trends

8.3　Introduction

NDE techniques, such as ultrasound testing (*1–8*), have been commonly used in the medical field for noninvasive imaging of internal features. These ultrasound C-scans are conducted by using ultrasonic transducers, which transmit and receive acoustic waves at low frequencies, typically between 200 kHz and 10 MHz. The acoustic waves are transmitted in the form of an ultrasound beam into the sample. Variations in acoustic impedance between two materials in the sample cause reflection of the waves, with large mismatches leading to strong ultrasound scattering (*1–3*). As the impedance ratio of two dissimilar materials increases, the amount of sound coupled through the interface decreases (*1–3*). The reflections caused by acoustic impedance mismatch occur at material boundaries and can aid in detecting flaws such as pores and inclusions (*1–8*). Reflected and scattered signals are received by the same or a second ultrasound transducer, amplified, and converted into electrical pulses, which can be plotted as a function of voltage vs. time for further analysis. Differences in the intensity of the collected ultrasound signals (pulse amplitudes) or the transit time of ultrasound energy through the materials (time-of-flight TOF) are quantified (figure 36). An image map is constructed by plotting these differences spatially, using gray scale or a color scale. While TOF scans can be used to evaluate changes in thickness, acoustic wave velocity, density, and acoustic impedance, pulse amplitude scans can be used to analyze attenuation, or loss, through a sample, which can be caused by reflection, scattering, diffraction, or absorption of the waves (*1–3*). Since this characterization technique is capable of identifying material changes within bulk samples, including detection of internal defects and flaws, it can be studied as a means of NDE of ceramic armor.
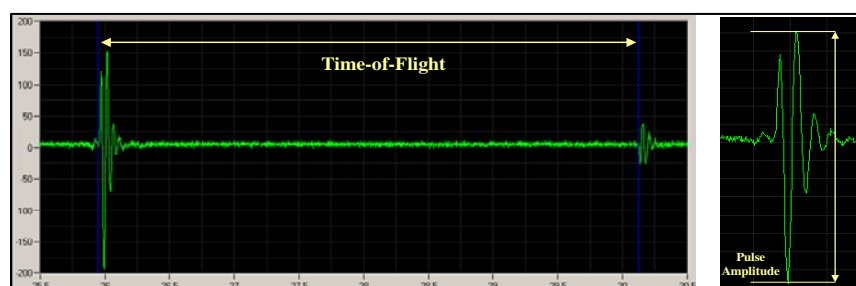
Figure 36. Actual signal generated from ultrasound beam through SiC sample.

By looking at ultrasound C-scans of various armor plates, the amplitude, attenuation, and TOF differences between samples can be compared and quantitatively analyzed to separate samples into categories based on defect volume percent, defect size, defect distribution, and defect location. Critical defect size limits should be set up by establishing correlations between quantitative studies and ballistic testing to determine the difference between "acceptable" and "unacceptable" armor plates.

8.4 Experimental Procedure

Ultrasound C-scan imaging incorporates the principles of point analysis and combines them with the use of a scanning system. This way, changes in signal amplitude and/or TOF can be analyzed over the entire sample rather than just a few points. In this case, an immersion tank is set up in order to contain the sample in a medium where the acoustic impedance mismatch is small enough to generate a strong signal. The transducer is mounted to the stage so that its position could be controlled in the x and y directions. A z-positioning device is also set up so that the position of the transducer can be manually adjusted relative to the sample. When the transducer is positioned at its optimum focal length (completely perpendicular to the surface of the sample at optimum tilt), the signal is maximized. As the transducer is rastered over the desired sample area, the transducer collects signals that are assigned to x and y coordinates. There are several inputs that are decided before the scan is conducted. The step size of the scan dictates the smallest increment over which a data point is collected. The gated region or regions dictate which signals are analyzed as the scan is run. Some examples of commonly gated signals used to study amplitude differences include the top surface signal, which is gated to study the amplitude difference at the surface of the sample, the bottom surface peak reflection, which is gated to study the density variations through the sample, and the region between the top and bottom signals, which is used to identify defects throughout the bulk of the sample. For TOF variation scanning, the top and bottom signals are gated separately and subtracted from each other to measure the variation in TOF over the sample area. The data is collected and pulse amplitude and TOF differences are assigned to a color scale, which represents variations in the amplitude over the scanned region. Depending on the assigned scale, one color shade difference represents a difference in voltage (in millivolts) or TOF (in microseconds). The data is mapped in relation to the assigned scale and the x and y positions of the points to produce a C-scan image of the sample over the gated region.

8.5 Accomplishments

Research on NDE of ceramic armor materials began in March 2004 with a literature search for previous work on high-frequency ultrasound (>10 MHz). Initial collaboration with Ultran Laboratories (*9*) in Boalsburg, PA concentrated on evaluating ceramic materials with acoustic impedance and material velocity values similar to armor materials such as Al_2O_3, SiC, and B4C (*10*). Commercial and experimental SiC samples were obtained from various companies for evaluation. The work began with point analysis of the samples to look for TOF values for the calculation of material velocities. Data from these samples was used to calculate various elastic properties in the materials. The groundwork was laid out to assemble a high-frequency ultrasound system that could be utilized at Rutgers University for point analysis and C-scan imaging of commercial and armor grade samples.

8.5.1 Initial Ultrasound C-Scan Imaging of SiC Samples

C-scan imaging was performed on a commercial SiC sample using a 50-MHz longitudinal-focused immersion transducer. The sample was placed into an immersion tank, and the z-position was adjusted until the maximum signal was obtained. The top and bottom surface signals were identified, and the bottom surface signal was gated so that the amplitude variation across the sample could be collected. The scan was initiated over the entire area of the sample. The SiC sample under investigation was previously determined to be highly dense, which was consistent with the C-scan map results. There were very minor amplitude variations in the image, as most of the C-scan was between 172–176 mV, representing a difference of ~12 dB of attenuation over the sample. After obtaining a C-scan image from the high-density SiC sample, two off-spec SiC samples were also scanned for comparison. An experimental SiC sample with a suspected lower-density region, as shown in figure 37, showed evidence of amplitude variations ranging from ~140 mV to low-density regions with ~120 mV, a ~26 dB attenuation loss for the lower-density areas. The low-amplitude regions demonstrated higher signal loss and greater microstructural changes in the lower-density SiC sample, which was the result of porosity or defects at these locations. Another experimental sample that was evaluated was a SiC plate fabricated by chemical vapor deposition (CVD). The sample had a known density gradient from end to end, and when the C-scan was performed, a color range representing the difference in amplitude from one side of the sample to the other was evident (figure 2). The scan went from a high amplitude (~180 mV) on the left side to a low amplitude (~40 mV) on the right side, a difference of ~43 dB. Other large defects were detected in various regions of the sample. The three SiC samples then underwent quantitative analysis to determine whether their differences could be identified from the C-scan image data.
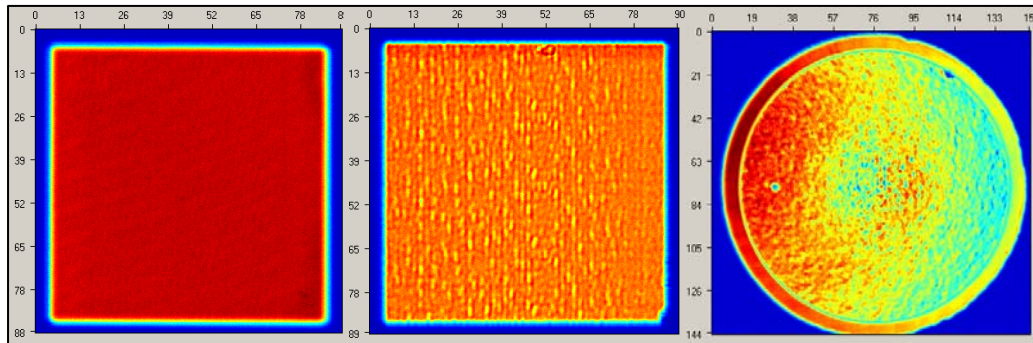
Figure 37. Ultrasound C-scan images of high density (left), lower density (middle), and density gradient (right) SiC samples.

8.5.2 Initial Quantitative Analysis Evaluation of SiC Samples

To study the scanned region, image data was incorporated into a normalized histogram detailing the number of occurrences of each color shade, which represented the distribution of amplitude values. The raw data of each selected scan area was normalized, and the data were plotted on a

histogram. The distribution of amplitudes for the high-density SiC sample showed a narrow distribution at a high range, since there were very few variations in microstructure. The normalized histogram for the lower-density SiC sample showed a broader distribution at a comparatively lower amplitude range due to the number of pores and defects of lower amplitude detected in the scan. The CVD-SiC sample, which contained large defects and a density gradient, showed the broadest range of values, since the gradient caused the amplitude to vary from very low to very high amplitude values. When observing a comparison of the normalized histograms for the three materials, it was evident that the higher-density samples showed lower-amplitude distributions over higher comparative amplitude ranges. This trend demonstrated a possible way of quantitatively evaluating and separating ceramic armor samples of varying material integrity into different categories.

8.5.3 Frequency Comparison of SiC Samples

C-scan imaging was also performed on three armor grade SiC samples to study the effect of frequency on defect detection. The transducers had initial frequencies of 5 MHz (WS25-5), 50 MHz (MDS25-50), and 125 MHz (MDS12-125). Sample A was a high-density armor grade SiC sample, sample B had a suspected region of lower density according to the manufacturer (as marked on the sample surface), and sample C had a single discolored region (as marked on the sample surface) that was believed to be a defect. Sample A was an example of an armor plate that would be sold commercially, while sample B and sample C did not meet standard specifications and would not be sold as armor materials. After gating the bottom surface peak reflections, each of the three samples was scanned at all three frequencies to identify density variations or other acoustically different features.

The SiC armor plate scans were compared based on sample type and frequency. Figure 38 shows the 5-MHz-amplitude C-scans for the three different SiC samples, which were very similar to one another, showing very minor amplitude changes represented by slight color variations across the samples. In figure 39, the 50-MHz C-scans were also uniform, but certain features were starting to become visible. For sample C, shown in figure 40, which contained the region believed to be a defect, the area corresponding to the circled region on the sample contained an amplitude variation in the C-scan that could not be detected at 5 MHz. Again, there were slight variations among the three samples at 50 MHz, but nothing drastic enough to establish a significant difference between A, B, and C.

At 125 MHz, the amplitude variations were very clear. While sample A, the armor grade SiC sample, was characterized by little variation in amplitude (~38-42 mV), sample B (~30-50 mV) and sample C (~32-48 mV) were characterized by large regions in which the amplitude was drastically different from the rest of the bulk. A large region of low amplitude (~30 mV) was identified within the region that was believed to have a lower density. Adjacent to the lower amplitude region was an area of much higher amplitude (~50 mV). The lower amplitude (higher attenuation) in the region indicated that there were patterns of small defects that could not be
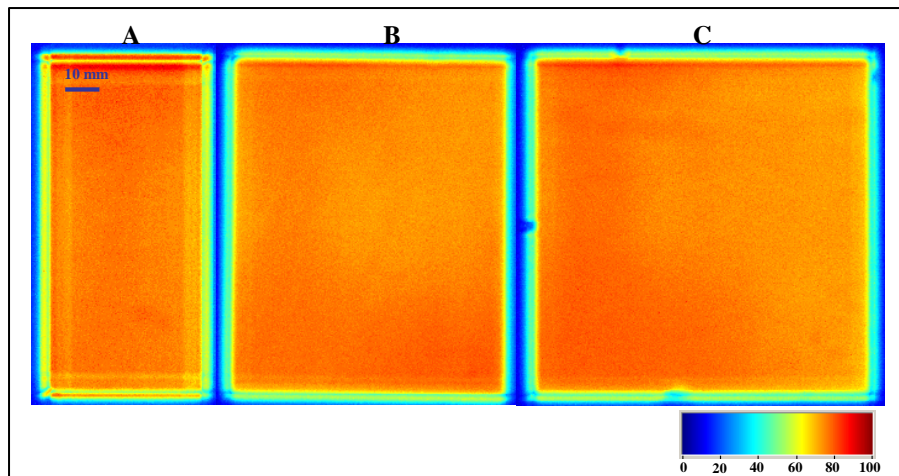
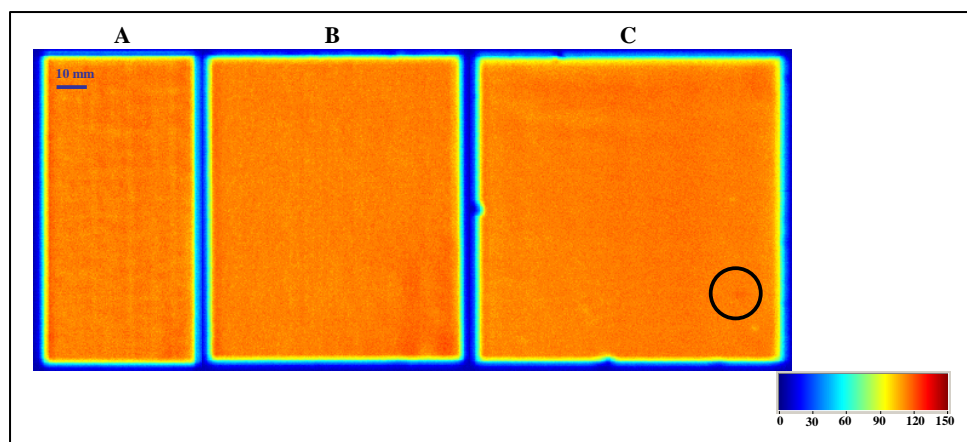Figure 38. The 10-MHz scans of A, B, and C SiC samples.

Figure 39. The 50-MHz scans of A, B, and C SiC samples showing defect region
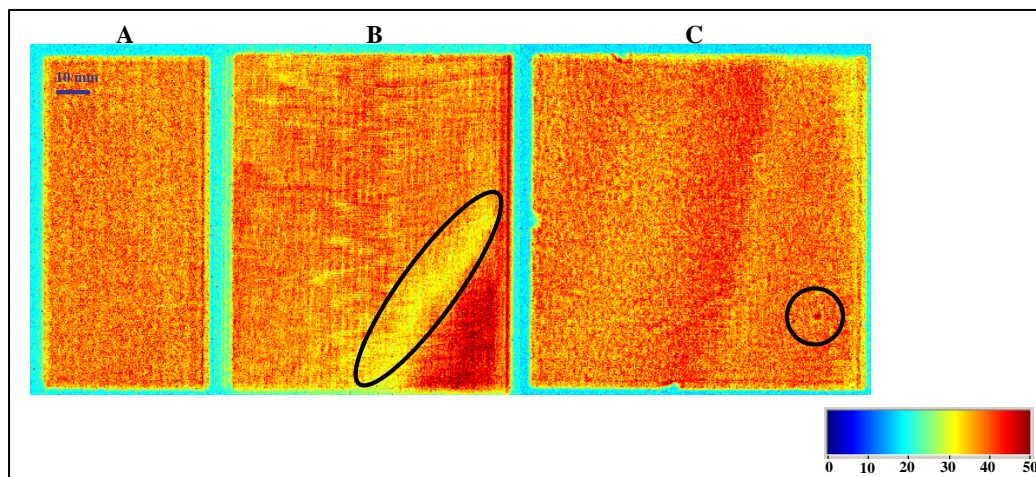(circled).

Figure 40. The 25-MHz scans of A, B, and C SiC samples showing low density and defect
regions (circled).

detected using the 5-and 50-MHz transducers. These defects caused additional scattering and resulted in lower amplitude in the region. Based on the sharp change from low amplitude to high amplitude (compared to the average amplitude of the bulk), it is possible that the low region was a result of a process-related issue, such as an inhomogeneous density distribution of the green SiC compact. This type of problem could be the result of poor die filling resulting from poor powder flow, and a nonuniform density in the hot-pressed SiC sample. In sample C, a nonuniform amplitude distribution was also detected, with alternating bands of high and low amplitudes across the sample. The presence of a specific defect was also detected in the same location that was identified by the manufacturer. The lower-amplitude values at this high frequency are consistent with the fact that there is a larger attenuation effect present.

The frequency comparison study of 5-, 50-, and 125-MHz ultrasound C-scan imaging of armor grade SiC armor samples demonstrated that ultrasound frequency is a critical parameter. While there were little to no observable differences between the two SiC samples of various material integrity at 5 and 50 MHz, 125-MHz scans showed drastic amplitude differences, representative of specific defects.

8.5.4 Quantitative Analysis Study of SiC Samples

The ultrasound C-scans of the three SiC samples were also evaluated quantitatively. Normalized-amplitude histograms of each sample at each frequency were produced to quantitatively compare samples with and without significant defect regions. After normalizing the amplitude data from each bottom surface scan, histograms were plotted by collecting the number of occurrences of each amplitude (y-axis) over the full amplitude range (x-axis) of each scan. In addition to plotting the normalized data, a curve (represented by a dashed line) was fit to each histogram based on a Gaussian distribution. The left side (or tail) of each curve, which represented the lower normalized-amplitude values, indicated the volume of defects and defect regions in the sample. The distribution of each curve indicated whether the range of normalized amplitudes for each scan was narrow or broad. A narrow curve represented a tight distribution of amplitudes and a small degree of change over the sample, whereas a broad distribution indicated a wide range of amplitudes, and a greater chance of defect and lower density regions.

The data were compared at each frequency (figure 41). For the 10-MHz amplitude histograms, the curves were very similar, all showing a relatively narrow distributions. This was to be expected, since there were few detectable differences among the samples at this lower frequency. At 50 MHz, there are more noticeable differences between the histograms. The highest-density armor-grade sample (A, indicated by the red curve) showed the most narrow distribution compared to the sample with the lower density region (B, green curve) and the sample with the known defect (C, blue curve). This difference indicated a greater range of amplitudes for the samples with greater material variance, which was to be expected since the amplitude ranges (and color ranges in the scans) were much broader for these samples. At 125 MHz, the
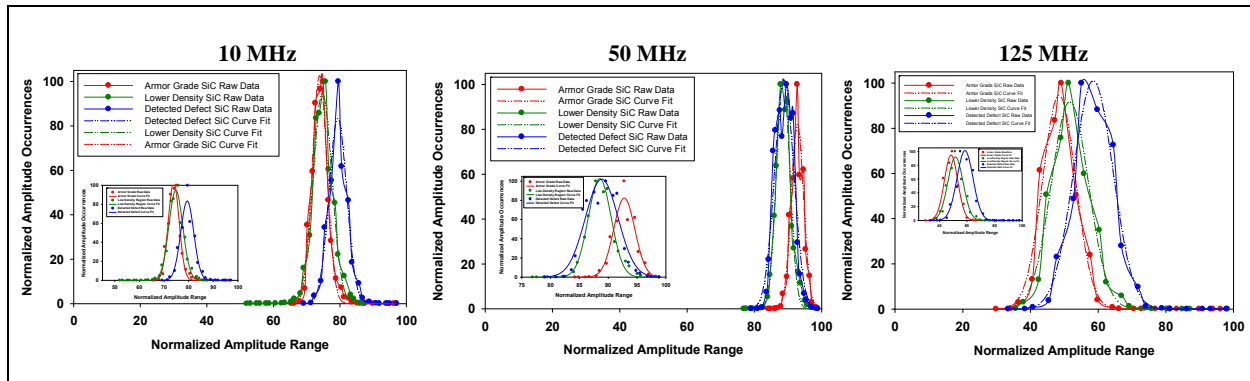
Figure 41. Normalized-amplitude histogram comparison of SiC samples at 10, 50, and 125 MHz.

difference among the curves is most apparent. The normalized-amplitude histogram curve from sample C (with the known defect) appeared to show the broadest comparative amplitude range, followed by sample B. The shapes of the curves were also changing to reflect minor changes in amplitude, indicative of specific defects and regions of varying density. The vast differences between the C-scans at this high frequency, shown in figures 38–40, were also apparent in the quantitative histogram data. In order to reinforce this point, the areas under the normalized histogram curves were collected and compared. The area-under-the-curve data were utilized to assign a single number to each histogram and test the theory that broader amplitude distributions reflected greater material changes, as shown in figure 42. For the 10-MHz scans, the area values did not follow the trend. It is believed that since the scans and curves were so similar to each other at this low frequency, one could not be distinguished from another. This reinforces the point that higher frequencies are required for bulk ceramic armor samples to distinguish material differences. At 50 MHz, the trend starts to follow suit: sample A shows the lowest area value, followed by sample B, and followed by sample C. The broadest amplitude distributions reflect the greatest material differences and the largest area values. The same trend follows for the 125-MHz histograms. The area-under-the-curve study is an intial comparitive quantitative analysis value, but there are other statistical parameters that must be studied.

8.5.5 Ultrasound Analysis of Armor Plates Provided by ARL

Three armor grade SiC samples from three different families of Ekasic materials (Ekasic F, Ekasic F-Plus, Ekasic T) were scanned at three separate frequencies. Each armor plate came from a single manufacturing lot in which other samples had been ballistically tested at ARL. Quantitative analysis of the three scanned samples were compared to the ballistic data to look for trends in the data. The samples were scanned at frequencies of 5, 50, and 125 MHz, as shown in figures 43–45. Just as in the study of the three SiC samples of various material integrity reported earlier, the lowest frequency of 5-MHz scans showed very few noticeable differences among the three materials. There was no strong evidence to separate one sample from the other at this frequency. The area-under-the-curve values from these scans, shown in figure 46 were also too similar to distinguish one from the other. There were some minor differences at 50 MHz, but
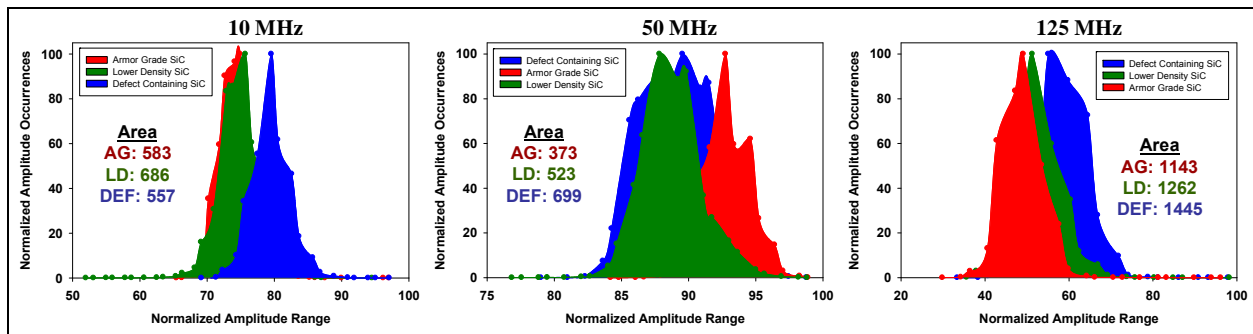
Figure 42. Area-under-the-curve comparison of SiC samples at 10, 50, and 125 MHz.
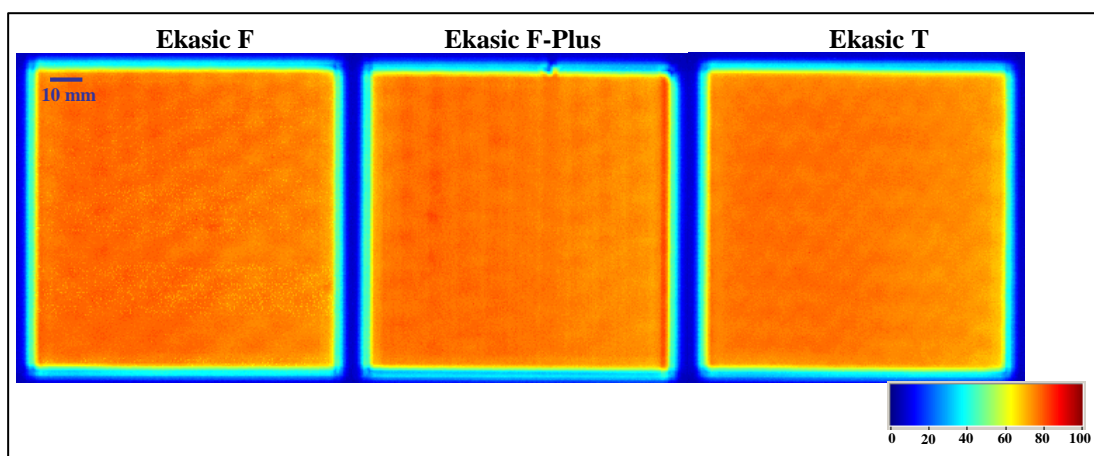
Figure 43. The 5-MHz scans of Ekasic F, F-Plus, and T SiC samples.
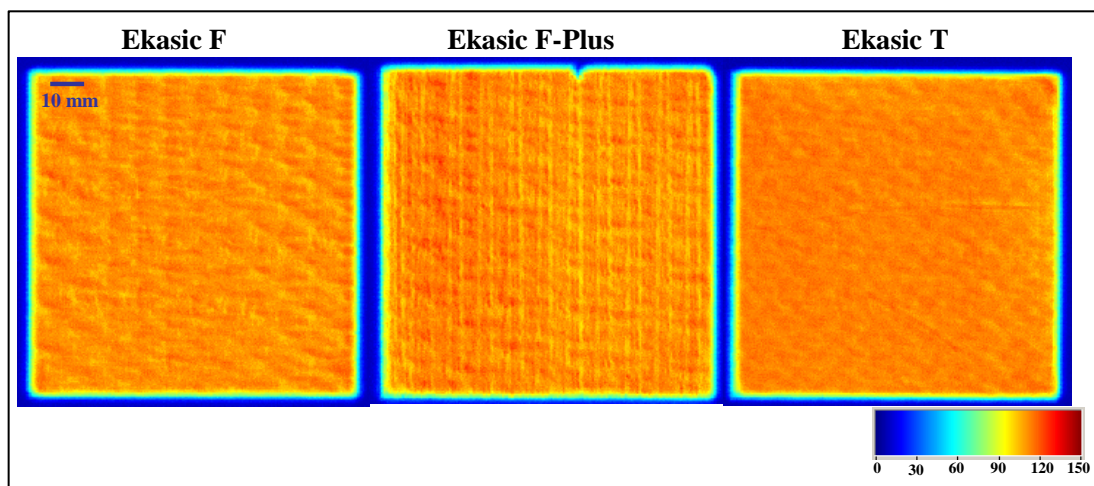
Figure 44. The 50-MHz scans of Ekasic F, F-Plus, and T SiC samples.
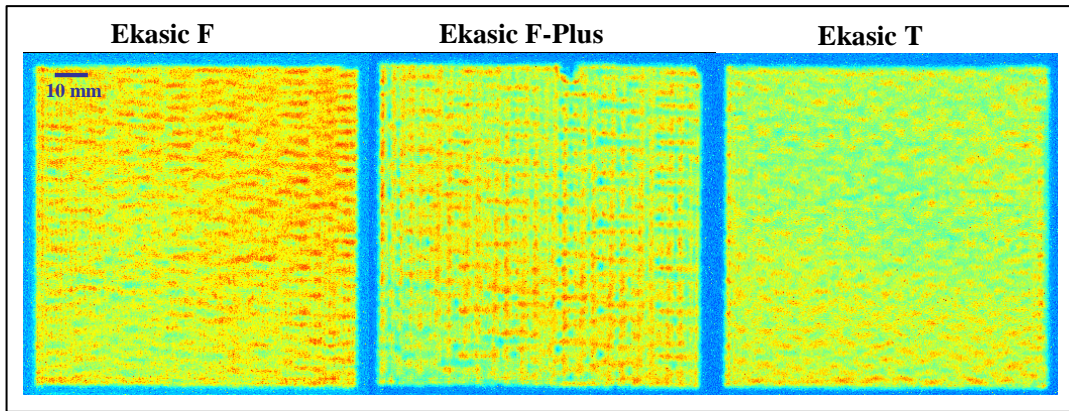
Figure 45. The 125-MHz scans of Ekasic F, F-Plus, and T SiC samples.
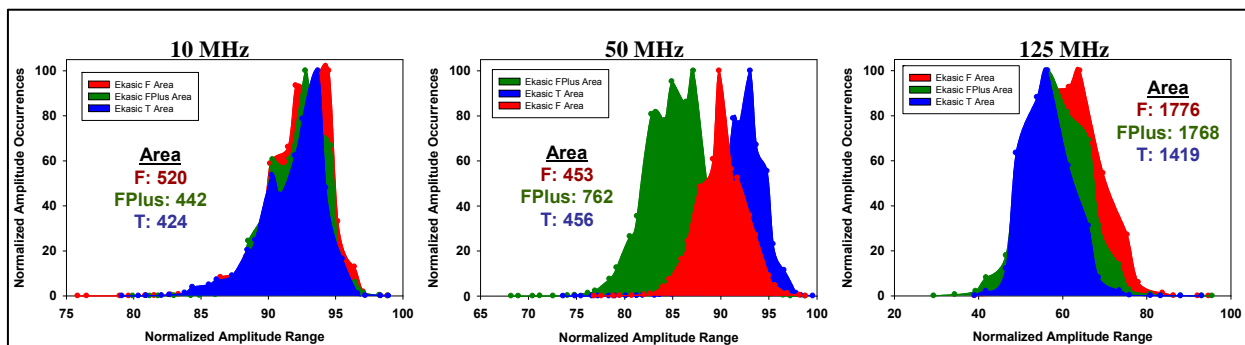
Figure 46. Area-under-the-curve comparison of SiC samples at 5, 50, and 125 MHz.

they also were not enough to draw conclusive evidence that the samples were significantly different from one another. The quantitative data showed that the Ekasic F and Ekasic T samples were almost identical as far as area-under-the-curve values, whereas the Ekasic F-Plus sample showed a much higher value (figure 46). Since the ultrasound scans of these samples were still quite similar at 50 MHz, the higher-frequency data were evaluated to study these trends further. At 125 MHz, the C-scans showed some major differences among samples. The quantitative data in this case showed a normalized-amplitude histogram for the Ekasic T sample with a more narrow distribution than the Ekasic F and F-Plus samples. The area-under-the-curve data, shown in figure 46, confirmed this finding: the Ekasic T area was 1419, compared to 1768 for F-Plus and 1776 for F. These results suggested that the Ekasic T sample was the most uniform and highly dense material and should give the best ballistic performance results.

The ballistic data for the three samples was obtained after generating the C-scan and quantitative analysis data for the Ekasic SiC samples. The Ekasic F sample had a V50 value of 625 m/s and a DOP of 27 mm. The Ekasic F-Plus sample had a V50 value of 700 m/s and a DOP of 16 mm. The Ekasic T sample had a V50 value of 725 m/s and a DOP of 12 mm. The ballistic data followed the same trend as the area-under-the-curve data—with the most narrow normalized-amplitude histogram distribution and smallest value of area corresponding to the sample with the highest V50 and lowest DOP. While the F and F-Plus samples also followed this trend, the area

75

values were much more similar to one another, suggesting that the ballistic data should also be more similar.

8.5.6 TOF Ultrasound C-scan Imaging

TOF is the time it takes for an ultrasound signal to be transmitted through a sample (*1*). By using a simple relationship of distance = rate × time, where time is the TOF and distance is the known thickness (t) of the sample, longitudinal and shear material velocities (c_l and c_s) can be determined from the following equations (*11*):

$$c_l = t / TOF_l \,, \tag{1}$$

and

$$c_s = t / TOF_s \,. \tag{2}$$

If the density (ρ) is known, the acoustic impedance (Z) can also be determined from the equation:

$$Z = \rho\, c \,. \tag{3}$$

In addition, the velocities can be used directly to calculate Poisson's ratio, elastic modulus, shear modulus, and bulk modulus. Poisson's ratio (v) can be calculated from c_s and c_l, using the following equation (*11*):

$$v = [1 - 2(cs/cl)]2 / [2 - 2(cs/cl)]2 \,. \tag{4}$$

Elastic, or Young's modulus (E), shear modulus (G), and bulk modulus (K) can also be calculated by the following equations (*11*):

$$E = [(c_l)^2(\rho)(1 - 2v)(1 + v)] / [g(1 - v)] \,, \tag{5}$$

$$G = (c_s)^2(\rho) \,, \tag{6}$$

and

$$K = E / [3(1 - 2\,v)] \,. \tag{7}$$

For this reason, the TOF value can be used to calculate a variety of important material properties, including elastic properties of ceramic armor.

TOF C-scan imaging was performed on the three armor grade SiC samples (A, B, and C) using a 50-MHz (MDS25-50) immersion transducer (*9*). After gating the top and bottom surface peak reflections, each of the three samples was scanned to identify TOF variations in the samples (figure 47). This allowed for a TOF image map and data set based on bulk differences with little influence from surface inhomogeneities.
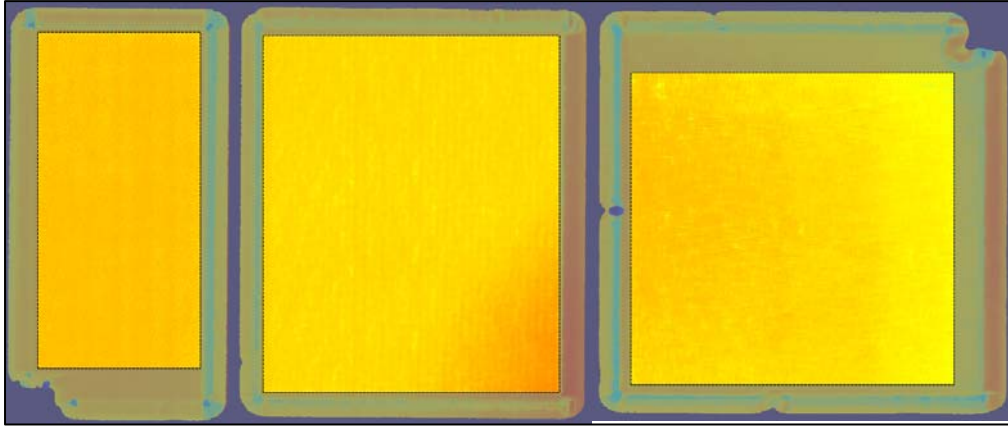
Figure 47. TOF C-scan images of samples A (left), B (middle), and C (right).

Sample A, the thickest of the three samples at 19.11 mm, had an average TOF value of 3.17 μs with a standard deviation of 0.00095. From these values, the average velocity of the sample was calculated as 12,060 m/s. The TOF variability was very small, with minimum and maximum values at 3.17 μs and 3.176 μs, respectively. The C-scan image (figure 47) shows the small degree of TOF variation over the sample area. Sample B was thinner than sample A, at 12.78 mm, and had an average TOF value of 2.13 μs with a standard deviation of 0.00384.

From these values, the average velocity of the sample was calculated as 12,000 m/s. The TOF range was from a minimum of 2.11 μs to a maximum of 2.15 μs. The bottom right corner of sample B stood out: there was an increase in TOF to approximately 2.15 μs, compared to the rest of the sample, which had regions with TOF values between 2.12 μs and 2.13 μs. This region was the same one identified by the manufacturer as being a possible low-density location, and the trend was consistent with the TOF results. A higher TOF and lower velocity indicated the presence of a region of lower acoustic impedance, most likely as a result of porosity, which increased the time for the ultrasound wave to travel through the sample. Sample C was approximately the same thickness as sample B at 12.79 mm and had an average TOF value of 2.14 μs with a standard deviation of 0.0031. From these values, the average velocity of the sample was calculated as 11,950 m/s. The range of TOF values for this sample was 2.122 μs to 2.148 μs. The TOF C-scan image showed the presence of two significant defects with much lower TOF values than the bulk of the sample. This region matched the area of the sample in which a distinct color variation could be seen on the surface.

This area was characterized by a sharp decrease in TOF, which showed that this region had a higher material velocity and, therefore, a higher acoustic impedance value than that of the bulk SiC material. Defects and regions of varying TOF gave sample C the lowest average velocity value. The trends from the TOF C-scan images were consistent with those previously determined from the pulse amplitude C-scans of the same samples, in which the lower-density region in sample A was identified as an area of lower pulse amplitude, and the defect in sample C was identified as a region with higher pulse amplitude.

In order to compare these TOF profiles better, the TOF range was normalized in figure 48. The histogram for sample A appeared to have the most narrow distribution, which was expected since it had the lowest TOF standard deviation value as well. One feature that stood out in the TOF histogram for sample B was the extended tail on the right side. This tail represented the higher TOF values from the low-density region in the bottom right corner of the sample. Sample C appeared to have a bimodal distribution in which there was a smaller mode on the right of the curve representing the higher TOF values in the upper part of the sample. When the C-scan image of this sample was observed, the higher TOF region (~2.14 μs) was larger than the lower TOF region (~2.13 μs) at the top of the sample. The areas and full-widths at half-maximum (FWHM) were evaluated for the normalized TOF histograms. Sample A had an area of 11.49 and a FWHM value of 0.075, compared to sample B's area of 22.88 and FWHM of 0.2 and sample C's area of 29.08 and FWHM of 0.28. Just as was the case for the normalized-amplitude histograms, the sample with the smallest area and FWHM was representative of the highest density and fewest number of detectable defects.
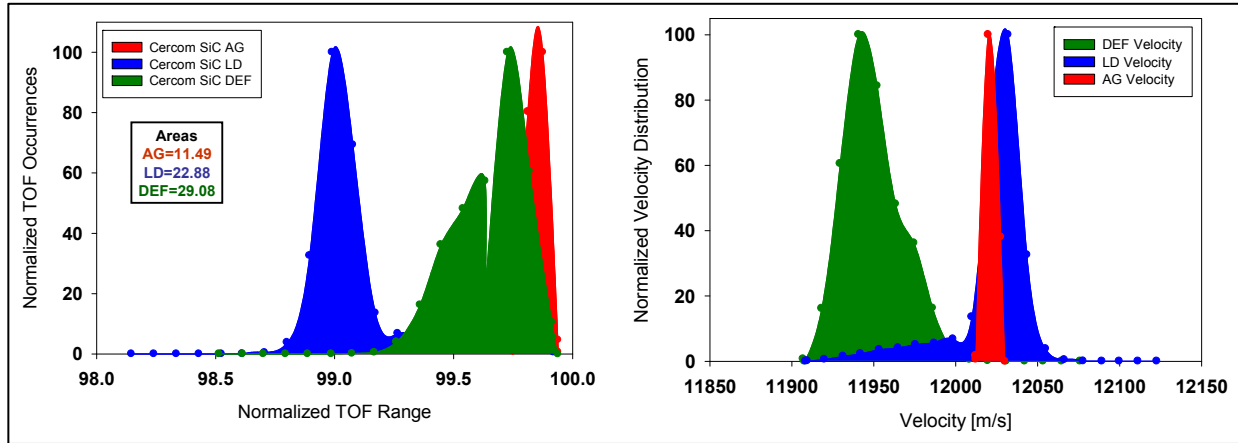
Figure 48. Longitudinal velocity histograms with normalized occurrences and range including areas.

The TOF values were also converted to longitudinal velocities for each of the samples (figure 49), and histograms were constructed. The velocities were plotted against the normalized number of velocity occurrences (figure 48). Since velocity is inversely proportional to TOF, the histogram trends were also reversed. Sample A had a velocity curve very similar to its TOF curve, with velocities ranging from ~12,010 to 12,030 m/s. Sample B showed a tail on the left side representing the lower-density region of lower velocity, with a range from ~11,910 to 12,220 m/s, as opposed to the tail on the right for the TOF profile. This was expected since a higher TOF value (time of travel) for the ultrasound signal through the sample represented a lower velocity (speed of travel) through the same sample at constant thickness. Sample C showed a lip on the right side of its velocity histogram in which the velocity values were higher. The velocity ranged from ~11,910 to 12,080 m/s for the sample. The areas of the velocity histograms were measured as 950 for sample A, 2815 for sample B, and 4121 for sample C. The FWHM values of the velocity histograms were measured as 16 m/s for sample A, 23 m/s for

sample B, and 34 m/s for sample C. Once again, the same trend followed: the best microstructural properties were correlated to the lowest area and FWHM values. The velocity histograms are more practical than the TOF histograms because samples are often compared based on their material velocities and the distributions are given in these curves.
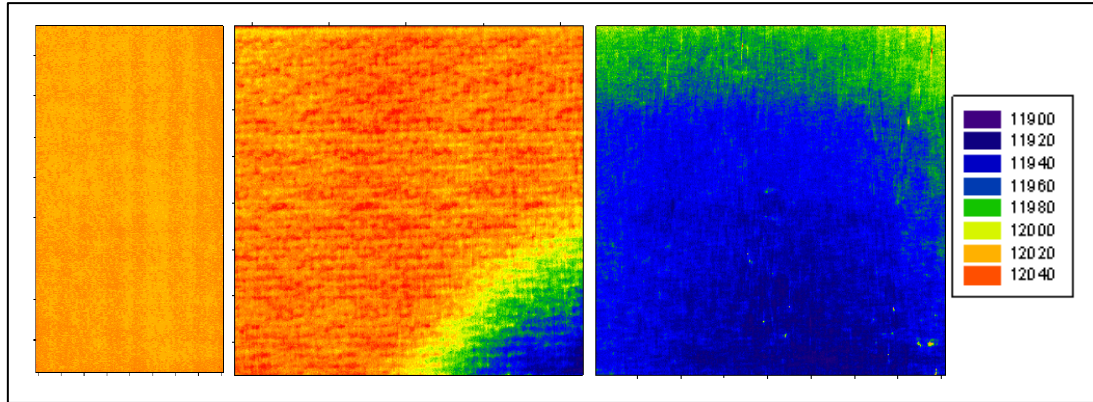
Figure 49. Longitudinal velocity maps of samples A (left), B (middle), and C (right).

For the normalized TOF and velocity histograms, each sample was characteristic of a different type of distribution based on its microstructural properties. Sample A was the most homogeneous, and its corresponding histogram had a near-perfect Gaussian distribution with the smallest area and FWHM values. Sample B had a distinctly different region of lower density, and its histogram had an extended tail with an area and FWHM larger than sample A's. Sample C had two large regions of slightly different material integrity and showed a bimodal distribution with the largest area and FWHM of the three samples. These trends are important for identifying and comparing material properties of samples based on their ultrasound fingerprints.

8.6   References

1. Mix, P. E. *Introduction to Nondestructive Testing*; John Wiley & Sons, Inc.: New York, NY, 1987.

2. Krautkramer, J.; Krautkramer, H. *Ultrasonic Testing of Materials*; Springer-Verlag: New York, NY, 1990.

3. Bray, D. E.; Stanley, R. K. *Nondestructive Evaluation: A Tool in Design, Manufacturing, and Service*; CRC Press, Inc.: Boca Raton, FL, 1997.

4. Schmerr, L. W. *Fundamentals of Ultrasonic Nondestructive Evaluation*; Plenum Press: New York, NY, 1998.

5. Ensminger, D. *Ultrasonics: Fundamentals, Technology, Applications*; Marcel Dekker, Inc.: New York, NY, 1988.

6. Papadakis, E. P., Ed. *Ultrasonics Instruments and Devices*; Academic Press: San Diego, CA, 1999.

7. Vary, A. *Materials Analysis by Ultrasonics: Metals, Ceramics, Composites*; Noyes Data Corporation: Park Ridge, NJ, 1987.

8. Bhardwaj, M. C. Evolution, Practical Concepts and Examples of Ultrasonic NDC. *Ceramic Monographs – Handbook of Ceramics* 1992, *41*, 1–7.

9. The Ultran Group Website. http://www.ultrangroup.com (accessed 2003).

10. Engineered Materials Handbook vol. 4: Ceramics and Glasses; ASM International, 1991.

11. Brown, A. Rationale and Summary of Methods for Determining Ultrasonic Properties of Materials at Lawrence Livermore National Laboratory. http://www.llnl.gov/tid/lof /documents/pdf/225771.pdf (accessed 2003).

9. Relation of Quasi-Static Properties to Ballistic Performance of Armor Ceramics

(Project initiated September 2005, completed March 2006)

(Project co-funded by the Ceramic Armor Subgroup
of the Ceramic and Composite Materials Center)

Core Faculty: W. R. Cannon, D. Niesz

NIST Collaborator: D. Quinn

Post-Doctoral Associate: T. E. Wilantewicz

9.1 Objectives

- Determine if indentation hardness, as well as other aspects of hardness testing (e.g., the indentation size effect [ISE], plastic deformation, elastic deformation, cracking, and partition of indentation energy) correlate with ballistic performance

- Determine if other intrinsic quasi-static material properties (possibly in combination with indentation hardness, i.e., a combined property index) correlate with ballistic performance

- Establish a technique primarily based on indentation testing that can accurately assess the ballistic impact resistance of ceramic materials, particularly in regards to different processing variations of the same basic material (e.g., SiC, Al_2O_3, B_4C)

9.2 Key Accomplishments

- Determined that Knoop hardness load characterization ISE can better distinguish between the hardness of materials than hardness at a single indentation load

- Determined that pressureless sintered SiC exhibited a much larger hardness variability than hot-pressed SiC

- Determined that cracking around and under Knoop indents must be considered a contribution to the overall variability observed in hardness testing

- Demonstrated that variability in Knoop hardness can be determined that is purely material and microstructure dependent and can not be attributed to operator or instrument error

9.3 Introduction

The indentation technique offers a simple and cost-effective approach to characterizing a "brittle" material's response to deformation and fracture (*1*). It is possible that understanding and characterizing the hardness of ceramic materials, as well as the deformation and fracture modes activated around an indentation site, may yield insight into the ballistic performance of candidate and current armor ceramic materials. Lankford et al. (*2*) have shown that when materials can be made flaw-free, compressive fracture under high strain rates using SHPB and flyer-plate impact tests occurs not from preexisting flaws in the material, but from plasticity-induced microcrack nucleation. That is, in the absence of pre-existing flaws in the material, the plasticity behavior of the material represents the ultimate limiting compressive strength. Thus, since the sharp indentation hardness test is essentially a confined compression test that can readily induce plastic deformation and microcracking in materials, the hardness of a material may be an indicator of its intrinsic compressive strength and its potential as an effective armor material. The hardness of a material and the cracking damage around indentation sites may be related to the onset of plasticity and cracking that takes place in dynamic plate impact experiments when the material is stressed above its Hugoniot elastic limit (HEL) (*3*). The HEL is the maximum compressive stress that a material can withstand and still remain linear elastic in a uniaxial strain (shock loading) experiment (*3*). The data of Sternberg (*4*) show good agreement between Vickers hardness and dynamic yield strength for several ceramic materials, as shown in figure 50. Such correlations appear promising for predicting dynamic yield strength for ceramic materials that have very different hardness. However, the situation is likely more complex when trying to predict Y_D for materials that have similar hardness but possibly different microstructures or mechanical properties, which may also affect Y_D and ballistic performance. Flinders et al. (*5*) found good correlation between the quasi-static Knoop hardness measured at 1-kg load (HK_1) and the ballistic mass efficiency (E_m) for six different hot-pressed silicon-carbide materials; however, there was no correlation between the ballistic mass efficiency and the V_{50} measured on the same materials.

Complications arising from cracking around Vickers indentations in highly covalent brittle ceramic materials, which can obscure the indentation diagonals and the variation of hardness with load (ISE) (*1*, *6–9*), add further uncertainty to the determination of a reliable hardness number that is appropriate, or meaningful, to ballistic performance. In addition, since it is not only plastic deformation that accompanies the onset of strength degradation in a ballistic impact experiment above the HEL, but also microcracking, the nature of the cracking and damage present around and below indentation sites may be as equally informative as the hardness number when trying to correlate with ballistic performance. All of these issues led to the need for a study that would carefully examine hardness vs. load (i.e., the ISE) for different ceramic materials. The study would use a diamond indenter geometry that would alleviate some of the problems associated with cracking, interrogate larger volumes of material than conventional Vickers microhardness testing at 200-g load, and examine the indentation damage.
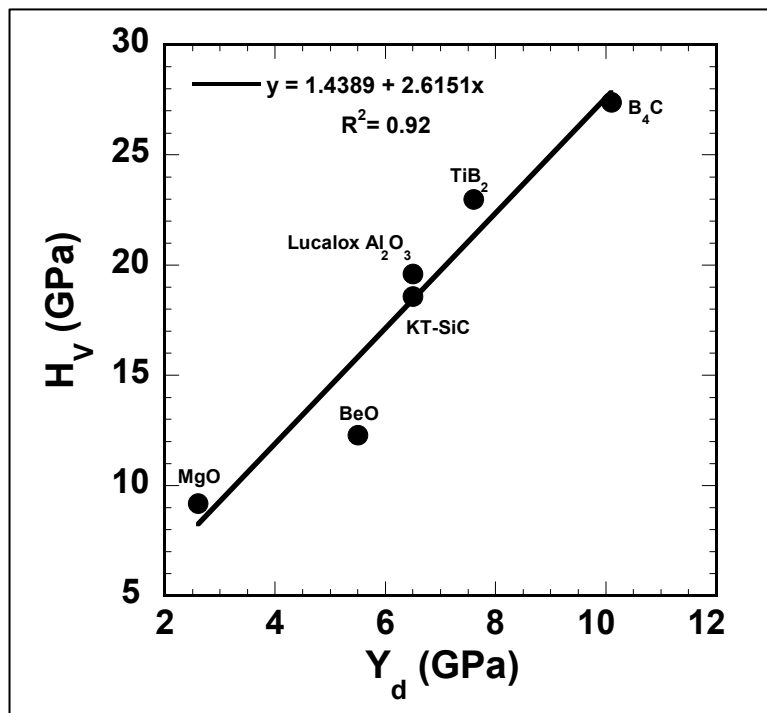
Figure 50. Vickers hardness as a function of the dynamic yield
strength for the materials examined by Sternberg (*4*). Data
from Sternberg (*4*).

9.4   Experimental Procedure

The indentation size effect was examined for five ceramic materials with a Knoop diamond
indenter in the load range from 0.49 to 137.3 N, with a 10-s hold time under load, at ambient
conditions. The geometry of this indenter lends itself to producing indentations at high loads
with little interference from cracking, which can cause unreadable indentations when using a
sharper diamond (e.g., Vickers).

The materials examined were (1) aluminum oxynitride (AlON), (2) AD995 CAP3 Al_2O_3, (3)
pressureless sintered alpha silicon carbide (Hexoloy SA), (4) hot-pressed silicon carbide
(SiC-N), and (5) hot-pressed silicon carbide (SiC-B). A minimum of 10 readable indentations
was used to calculate an average hardness number at each load. A Zwick 3212 hardness tester
was used. It must be emphasized that great care was taken to ensure the accuracy of these
measurements. This was achieved by checking the accuracy of the hardness tester with the U.S.
National Institute of Standards and Technology (NIST) standard reference material SRM 2830
(*10*), as well as that of the digital filer measuring system. The latter was accomplished by
measuring the NIST-produced indentations on the standard reference material (SRM) material
and comparing these values to the NIST-measured values. In addition, a stage micrometer was
used to check the accuracy of the measuring system at all magnifications used. The same
measuring system was used to measure all indentations. Less than a 1% difference was found
when compared with the NIST SRM Knoop hardness value and with the NIST SRM Knoop

83

diagonal size. Specimens were mounted in epoxy and supported by a leveling device that ensured the specimens were perpendicular to the indenter and did not move during testing.

In addition, an instrumented indentation tester, utilizing a load cell and capacitance displacement gauges, was used to simultaneously monitor the load and displacement of a Vickers diamond indenter that was pushed into the materials. A maximum load of 1 kg was reached using an indenter displacement rate of 0.2 μm/s. Five test runs per sample were performed. The AlON material was not tested; however, a hot-pressed B_4C material was tested in its place. This testing format, similar to the one proposed by Milman and Chugunova (*11*), allowed for the direct determination of a plasticity characteristic. Also, by integrating the loading and unloading curves from these tests, the total indentation energy, the elastically recovered energy, and the work of indentation were determined. The Vickers hardness was also determined while the materials were under maximum load.

9.5 Accomplishments

9.5.1 Knoop Hardness

The Knoop hardness is shown as a function of load for the five materials in figure 51 and a function of diagonal length in figure 52. The Knoop hardness does not show a distinct plateau to a constant hardness value at high loads. The data of Li et al. (*6*) on a pressureless sintered silicon carbide also showed no plateau for Knoop hardness as a function of load. On the other hand, Vickers hardness data as a function of load for ceramic materials shows a distinct plateau (transition) to constant hardness (*1*, *6–9*). This suggests that a saturation in the elastic-plastic-fracture response of the material is reached sooner (at a lower load) under a Vickers indenter than a Knoop indenter. Thus is possibly related to the more severe cracking seen around Vickers indentations than the Knoop indentations (*1*, *6*, *9*). Another significant finding, however, was that the pressureless sintered silicon carbide showed more variability in its hardness and a greater decrease in hardness beyond 2-kg load than the hot-pressed SiC materials (SiC-N and SiC-B). Variability in hardness may possibly be an indicator of variability in ballistic performance (or of ballistic performance itself), which necessitates making accurate hardness measurements in order to separate operator and/or instrument errors from true variability of hardness in the material. In addition, the Knoop hardness of the pressureless sintered SiC was similar to the hot-pressed SiCs at loads of 1 kg and below; however, as the load was increased to 2 kg and greater, the hardness, relative to the hot-pressed SiCs, decreased considerably. Tables 4 and 5 show the raw Knoop hardness and diagonal length data, respectively. As seen from table 6, as the indentation load increased, the variability in the sizes of the indentations increased. The increased degree of cracking with increasing load that was seen for all materials may be the reason for this. That is,
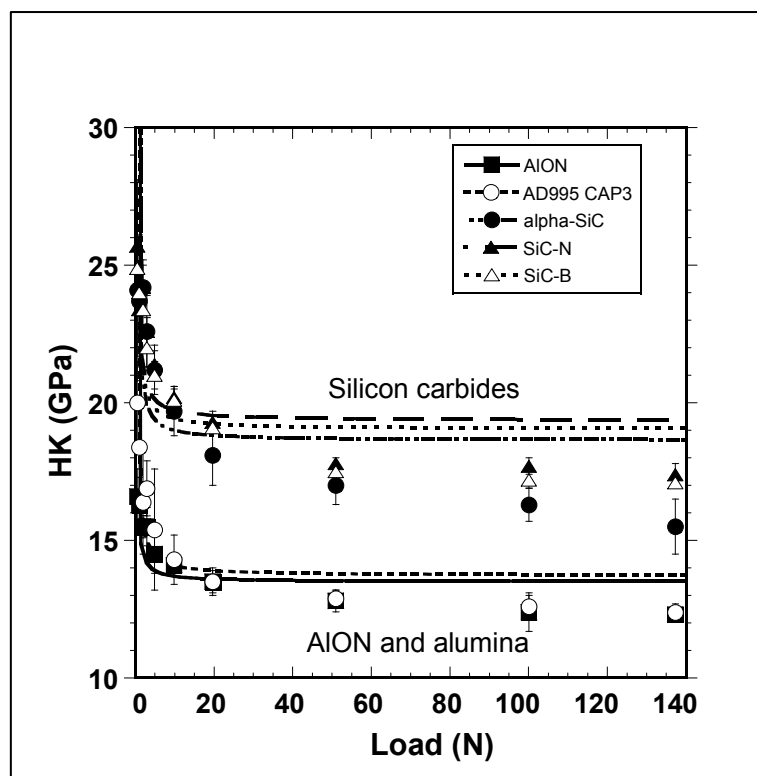
Figure 51. The variation of Knoop hardness as a function of
indentation load for the five ceramic materials. Data was
fit to an equation of the form: $HK = a/F + b$, where a and
b are constants and F is the indentation load (uncertainties
are ±1 standard deviation).

increased cracking may lead to increased variability in diagonal size. An analysis of variance (ANOVA) was carried out on the Knoop hardness and diagonal length data. A measure of the overall variability within the treatment means from the ANOVA is shown in the last row in tables 4 and 5, given by $SS_E/N-a$. Since care was taken to ensure the accuracy to which the Knoop long diagonals were measured, it is believed that a large portion of the variability is due to actual variability of hardness from location-to-location in the material, and only a small portion is due to measurement error. It is assumed the measurement error is constant for each material. Ten repeated diagonal length measurements on the same indentation in the SRM material showed the standard deviation was 0.4 μm, which is smaller than the standard deviations of the diagonal lengths shown in table 5. Hence, it is reasonable to conclude that measurement error could contribute, at most, 0.4 μm to the standard deviations in diagonal sizes shown in table 5. The pressureless sintered SiC showed much greater overall variability in hardness and diagonal size than the two hot-pressed materials. Presumably, the wider distribution in grain size of the α-SiC material compared to the hot-pressed materials contributed to this variability. If there is a significant distribution in pore size and/or clustering of pores in this material, this would presumably further contribute to the variability.
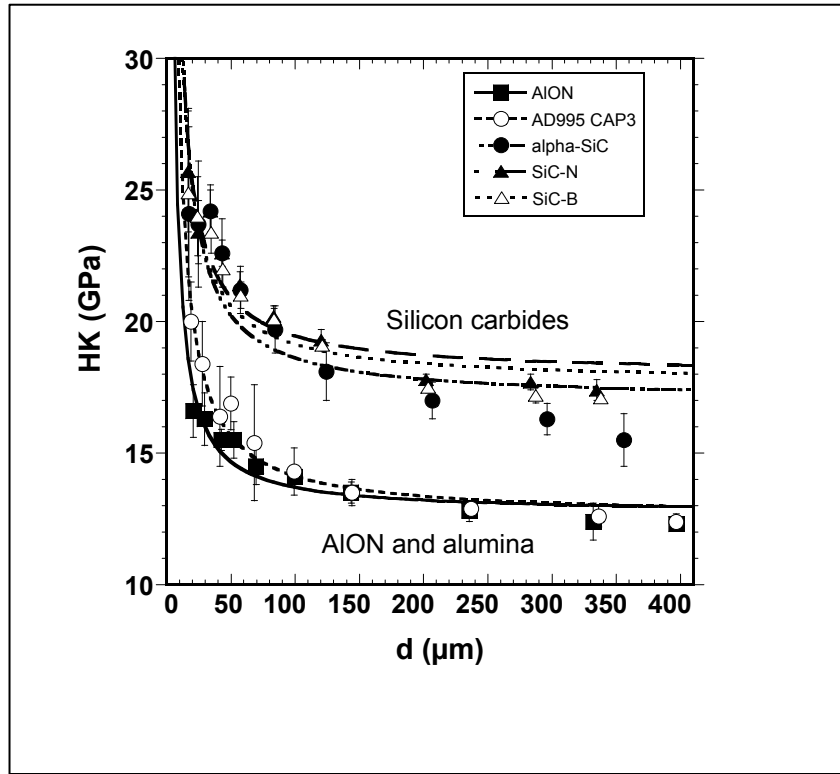
Figure 52. The variation of Knoop Hardness with indentation diagonal size for the five ceramic materials. Data was fit to an equation of the form: HK = $a_1'/d + a_2'$, where a_1' and a_2' are constants and d is the indentation diagonal length (uncertainties are ±1 standard deviation).

Table 4. Knoop hardness (uncertainties are ±1 standard deviation).

Load (N)	A1ON HK (GPa)	AD995 CAP3 HK (GPa)	α SiC-N HK (GPa)	SiC-N HK (GPa)	SiC-B HK (GPa)
0.49	16.6 ± 1.0	20.0 ± 1.5	24.1 ± 1.5	25.7 ± 2.3	24.9 ± 3.2
0.98	16.3 ± 1.0	18.4 ± 1.6	23.7 ± 2.4	23.4 ± 1.2	24.0 ± 1.5
1.96	15.5 ± 0.4	16.4 ± 1.9	24.2 ± 1.0	24.2 ± 0.8	23.4 ± 0.8
2.94	15.5 ± 0.7	16.9 ± 1.0	22.6 ± 1.3	22.6 ± 0.5	22.0 ± 0.7
4.90	14.5 ± 0.7	15.4 ± 2.2	21.2 ± 0.9	21.4 ± 0.5	21.0 ± 0.5
9.81	14.1 ± 0.4	14.3 ± 0.9	19.7 ± 0.9	20.2 ± 0.4	20.1 ± 0.4
19.61	13.5 ± 0.4	13.5 ± 0.5	18.1 ± 1.1	19.3 ± 0.4	19.1 ± 0.2
50.99	12.8 ± 0.4	12.9 ± 0.3	17.0 ± 0.7	17.8 ± 0.2	17.5 ± 0.2
100.03	12.4 ± 0.7	12.6 ± 0.4	16.3 ± 0.6	17.7 ± 0.3	17.2 ± 0.3
137.29	12.3 ± 0.2	12.4 ± 0.3	15.5 ± 1.0	17.4 ± 0.4	17.1 ± 0.1
SS_E/N-a (GPa^2)	0.4	1.8	2.4	0.8	1.2

86

Table 5. Knoop indentation diagonal length (uncertainties are ±1 standard deviation).

Load (N)	A1ON (μm)	AD995 CAP3 (μm)	α SiC (μm)	SiC-N (μm)	SiC-B (μm)
0.49	20.50 ± 0.6	18.7 ± 0.7	17.1 ± 1.30	16.5 ± 0.8	16.80 ± 1.2
0.98	29.30 ± 0.9	27.6 ± 1.4	24.4 ± 1.30	24.4 ± 0.6	24.10 ± 0.8
1.96	42.40 ± 0.6	41.4 ± 2.5	34.0 ± 0.70	34.0 ± 0.5	34.50 ± 0.6
2.94	52.10 ± 1.2	49.8 ± 1.5	43.1 ± 1.30	43.0 ± 0.5	43.70 ± 0.7
4.9	69.40 ± 1.6	68.0 ± 7.4	57.3 ± 1.20	57.1 ± 0.6	57.70 ± 0.7
9.81	99.70 ± 1.5	99.1 ± 3.2	84.3 ± 2.10	83.1 ± 0.9	83.40 ± 0.8
19.61	143.7 ± 2.2	144.1 ± 2.6	124.3 ± 3.70	120.2 ± 1.2	121.0 ± 0.7
50.99	235.6 ± 5.1	237.1 ± 2.3	206.6 ± 4.10	201.9 ± 1.1	203.7 ± 1.0
100.03	332.0 ± 3.8	336.3 ± 5.4	296.1 ± 5.50	283.3 ± 2.3	287.3 ± 2.4
137.29	396.7 ± 6.0	396.7 ± 4.7	356.0 ± 11.4	334.9 ± 3.6	338.1 ± 1.0
SS_E/N-a (μm^2)	9.9	15.8	16.2	1.7	1

9.5.2 Cracking and Hardness

It was observed for the three SiC materials and AD995 CAP3 alumina that, in general, indentations which were more severely cracked had lower Knoop hardness than less cracked indentations. This should not be surprising since more damaged material facilitates greater indentation penetration. Although in general it was found that lower hardness could be associated with increased cracking around indentation sites, it should be pointed out that some indentation sites, which appeared to be more cracked on the surface, had the same, or higher, Knoop hardness than less cracked sites. This might be because looking at just the surface damage around indentation sites may not accurately assess the full extent of damage in all cases; some damage exists below the surface. That is, the subsurface damage may not always be accurately reflected in the surface damage surrounding the indentation site, and it may be the reason for such discrepancies. Some of the cracking may have occurred during indenter withdrawal as well. There was less indication of cracking affecting hardness for the AION material. However, since the grains of this material are very large compared to the sizes of the indentations, hardness anisotropy effects may mask or nullify any affect of cracking on hardness. This part of the work is discussed in more detail in a paper by Wilantewicz et al. (*12*).

9.5.3 Deformation and Fracture Characterization

An optical microscope was used to examine all of the Knoop indentation sites. Some degree of cracking was observed around all indentation sites. Extensive lateral and radial cracks were seen around the AlON material. Radial and lateral cracks were apparent around the AD995 CAP3 material, but they were reduced in size and number compared to AlON. In addition, the surfaces of the indentation sites appeared relatively smooth for the AlON and AD995 CAP3 materials, indicating that plasticity was most likely a major component of the permanent deformation.

For the hot-pressed SiC-N and SiC-B materials, extensive intergranular fracture was observed around the midpoints of the indentations. Subsurface lateral cracks and chipped material at the

surface from grain pop-out was also seen. Small radial cracks were also apparent near the tips of the indentations as well as near the midsection of the indentations. Indentions in the α-SiC material showed little intergranular fracture and grain pop-out but more signs of shear faulting within the indentation. Small radial cracks also surrounded the indentations, similar to the hot-pressed SiC. Despite the cracking seen around the Knoop indentations, the tips of most of the diagonals were readable, the exceptions being if a tip landed in a pore or, for AlON, if the bright subsurface reflections from lateral cracks were intense enough to render the tip indistinguishable from the background. If the tips were not readable, the indentation was rejected and not used in the determination of hardness. Occasionally, slender cracks that would extend from exactly the tips of the diagonal would render an indent unreadable.

Indentations were also made with a Vickers diamond at 2-kg load in order to compare to the Knoop indentation sites. In general, the cracking was much more severe. The extensive cracking rendered most of the indentation diagonals unreadable at 2 kg for the SiC materials and AD995 CAP3 alumina. There was a slightly higher number of readable indents for the AlON material. Also, the difference in fracture mode between the α-SiC (primarily transgranular) and hot-pressed SiC materials (primarily intergranular) was noticeable.

9.5.4 Instrumented Indentation Testing

Sharp discontinuities on the loading cycle were noted in the B_4C material for all test runs, indicating some type of massive failure beneath the indenter causing a sudden redistribution of the load. An example of such a test run for B_4C is shown in figure 53. Such failure under an indenter may be related to the relatively poor ballistic performance of B_4C observed under very high shock loading pressures, which is believed to be caused by a sudden and drastic loss in shear strength of the material when stressed above its HEL (*13*). The maximum penetration, percent permanent deformation, and hardness under maximum load (LVH_{max}) for all materials are shown in table 6. The percent permanent deformation is analogous to the plasticity characteristic of Milman and Chugunova (*13*). Also shown in table 6 is the work of indentation (WOI), which was the area bound by the loading and unloading curves and which represents the energy consumed in permanently deforming and fracturing the materials under the indenter.

Table 6. Instrumented indentation testing data (uncertainties are ±1 standard deviation).

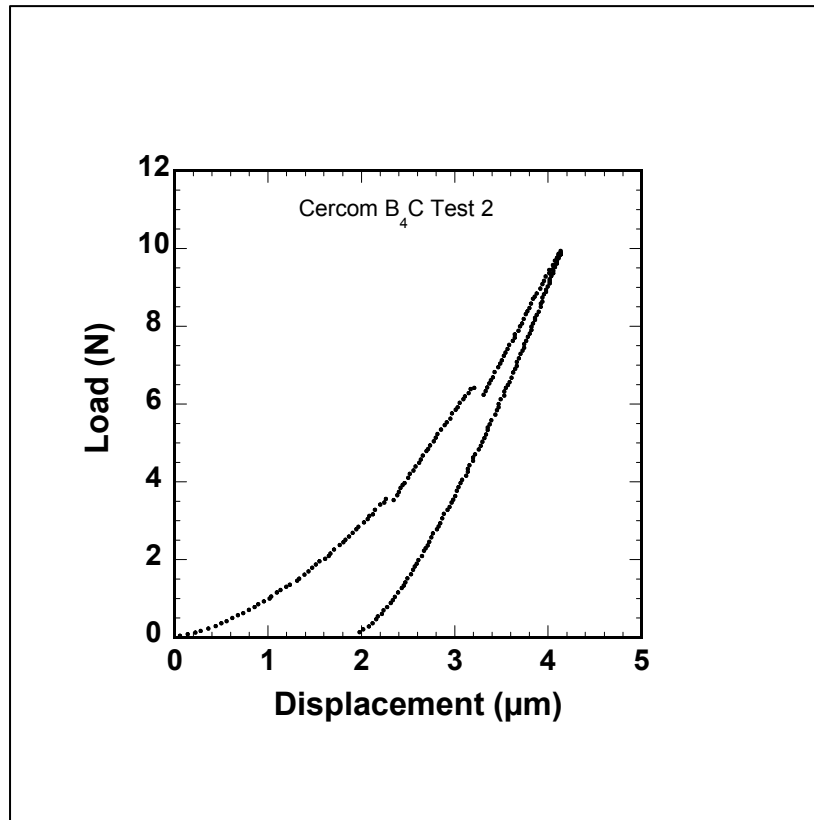| Sample	Max. Pen. (μm)	Percent Permanent Deformation (%)	LVH Max. (GPa)	WOI (μm)	WOI-Percent
SiC-N	4.3 ± 0.2	47.8 ± 1.2	20.1 ± 1.6	7.5 ± 0.3	44.1 ± 1.2
SiC-B	4.5 ± 0.1	50.7 ± 0.8	18.2 ± 0.8	7.7 ± 0.4	46.6 ± 1.2
α-SiC	4.3 ± 0.2	50.0 ± 3.5	20.3 ± 1.6	8.4 ± 0.4	41.8 ± 2.0
AD-995 CAP3 Al_2O_3	5.1 ± 0.3	62.7 ± 1.7	14.4 ± 1.4	11.6 ± 0.4	59.5 ± 0.8
B_4C	4.1 ± 0.1	49.4 ± 3.5	21.8 ± 0.5	6.3 ± 0.5	41.7 ± 2.9

Figure 53. Load-displacement trace for hot-pressed B4C material showing
sharp discontinuities on the loading cycle, presumably due to
failure, causing a redistribution of the load.

All three silicon-carbide materials and boron carbide had similar values of maximum penetration. The indenter penetrated the most in the alumina material, which was consistent with its lower hardness value than the carbide materials. The percent permanent deformation of the four carbide materials was very similar—roughly 50% for the 1-kg tests. This means that about half the deformation beneath the indenter was plastic, and half was elastic. This is in strong contrast to the alumina material, where the percent permanent deformation was 63%, indicating that the majority of deformation beneath the indenter was plastic. Since, according to Lankford et al. (*2*), plasticity-induced microcracking represents the ultimate limiting strength of many ceramic materials, the plasticity in the alumina material (greater than the SiCs) is consistent with the poorer performance (compared to the SiC materials) of alumina ceramics as a whole. Unfortunately, no strong differences in plasticity characteristic were seen between the hot-pressed and pressureless sintered silicon carbides. However, more tests may be necessary to reveal any differences.

Within the experimental error, the WOI was similar for SiC-N and SiC-B; however, it was slightly lower for the pressureless sintered SiC (α-SiC). Since the maximum penetration depth was essentially the same for the hot-pressed and α-SiC materials, the difference was due to the shapes of the load-displacement curves. For the α-SiC material the load-displacement curve was

89

slightly more concave in the initial part of loading than the hot-pressed SiCs. The presence of pores in this material may facilitate indenter penetration at low loads. This would result in a slightly lower area under the loading curve and, hence, less total energy consumption than the hot-pressed SiCs. The last column in table 6 shows the WOI expressed as a percentage of the total energy. The α-SiC material has a slightly lower WOI- percent than the hot-pressed materials. This means that the percentage of the total indentation energy that was permanent deformation was slightly lower for this material than for the hot-pressed SiCs.

When compared to the SiC materials, the AD995 CAP3 alumina material was penetrated more by the indenter. Consequently, a greater amount of energy was put into this material than into the SiC materials for the same maximum load. The elastic recovered energy was less than the SiCs; consequently, the WOI was considerably greater than the SiC materials. The WOI-percent was ~60% for this material, which means the majority of indentation energy goes to permanently deforming the alumina. This is opposite for the SiC materials, where the majority (>50%) of energy is elastically recovered. The B_4C material had total, recovered, and WOI energies similar to the α-SiC material. However, it must be recalled that all test runs for B_4C showed sharp discontinuities on the loading cycle; hence, the areas under the loading curves are somewhat uncertain.

9.6 Conclusions

Several conclusions were drawn from this work. First, Knoop hardness-load characterization (ISE) is more informative than hardness at a single load, because the hardness of materials may be similar at one load range, and differ at another. This occurred for the pressureless sintered and hot-pressed silicon-carbide materials examined. Second, much larger hardness (diagonal size) variability was seen in the pressureless sintered SiC than the two hot-pressed SiCs. This may be an important parameter in regards to variability in ballistic performance (or ballistic performance itself), particularly when the average hardness of materials is similar. Third, since cracking is an unavoidable and inherent response of brittle ceramic materials to sharp indentation testing, it must be viewed as another contribution to the ISE and part of the overall variability of hardness. Fourth, by making accurate hardness measurements, variability in hardness that is not due to operator or instrument errors can be detected. In this regard, particular attention must be given to the measurement of the diagonal sizes and to the condition of the diamond indenter tip and should ensure a level and secure specimen that does not move during testing. Finally, instrumented indentation testing allowed the determination of the elastic and plastic deformation response of the materials under an indenter. All three SiC materials showed similar plasticity behavior, although the pressureless sintered SiC consumed slightly less energy (smaller WOI) than the two hot-pressed SiCs for the same indentation load. A greater proportion of the indentation energy for AD995 CAP3 alumina material was due to plastic deformation than was due to elastic recovery, which was opposite the behavior of the SiC and B_4C materials.

9.7   References

1. Quinn, J. B.; Quinn, G. D. Indentation Brittleness of Ceramics: A Fresh Approach. *J. Mat. Sci.* **1997**, *32*, 4331–4346.

2. Lankford, J.; Predebon, W. W.; Staehler, J. M.; Subhash, G.; Pletka, B. J.; Anderson, C. E. The Role of Plasticity as a Limiting Factor in the Compressive Failure of High Strength Ceramics. *Mechanics of Materials* **1998**, *29*, 205–218.

3. Kanel, G. I.; Bless, S. J. Compressive Fracture of Brittle Solids Under Shock-Wave Loading. In *Ceramic Armor Materials By Design.* McCauley, J. W.; Crowson, A.; Gooch, W. A.; Jr.; Rajendran, A. M.; Bless, S. J.; Logan, K. V.; Normandia, M.; Wax, S., Eds. The American Ceramic Society: Westerville, OH, 2002; pp. 197–216.

4. Sternberg, J. Material Properties Determining the Resistance of Ceramics to High Velocity Penetration. *J. Appl. Phys.* **1989**, *65* (9), 3417–3424.

5. Flinders, M.; Ray, D.; Anderson, A.; Cutler, R. A. High-Toughness Silicon Carbide as Armor. *J. Am. Ceram. Soc.* **2005**, *88* (8), 2217–2226.

6. Li, Z.; Ghosh, A.; Kobayashi, A. S.; Bradt, R. C. Indentation Fracture Toughness of Sintered Silicon Carbide in the Palmqvist Crack Regime. *J. Am. Ceram. Soc.* **1989**, *72* (6), 904–911.

7. Taniguchi, T.; Akaishi, M.; Yamaoka, S. Mechanical Properties of Polycrystalline Translucent Cubic Boron Nitride as Characterized by the Vickers Indentation Method. *J. Am. Ceram. Soc.* **1996**, *79* (2), 547–549.

8. Berriche, R.; Holt, R. T. Effect of Load on the Hardness of Hot Isostatically Pressed Silicon Nitride. *J. Am. Ceram. Soc.* **1993**, *76* (6), 1602–1604.

9. Swab, J. J. Recommendations for Determining the Hardness of Armor Ceramics. *Int. J. Appl. Ceram. Technol.* **2004**, *1* (3), 219–225.

10. SRM 2830. Knoop Hardness of Ceramics, Standard Reference Materials Office, NIST: Gaithersburg, MD, 20899, **1995**.

11. Milman, Yu. V.; Chugunova, S. I. Mechanical Properties, Indentation and Dynamic Yield Stress of Ceramic Targets. *International Journal of Impact Engineering* **1999**, *23*, 629–638.

12. Wilantewicz, T. E.; Cannon, W. R.; Quinn, G. D. The Intentiation Size Effect (ISE) for Knoop. In *Advances in Ceramic Armor II, Ceramic Engineering and Science Proceeding, Cocoa Beach*; Wereszczak, A.; Lara-Curzio, E.; Prokurat-Franks, L., Eds.; John Wiley and Sons, Inc.: Hoboken, NJ, 2007 and the American Ceramics Society: Westerville, OH, 2006; pp 237–250.

10. Directionally Textured Boron Carbide by Controlled-Shear Processing

(Project initiated September 2005, completed December 2005)

Core Faculty: R. Haber, M. Chhowalla, D. E. Niesz

ARL Collaborator: J. McCauley, R. McCuiston

Graduate Student: D. Maiorano

10.1 Long-Range Objectives

- Investigate the effect of aligned crystallographic texture on the mechanical and ballistic properties of fine-grained boron carbide

- Develop the ability to produce dense boron-carbide microstructures with a high degree of grain orientation using controlled shear as the orientation mechanism

- Compare the properties of textured boron carbide along different crystal axes to the properties of randomly oriented boron-carbide bodies to determine axes of greatest and least hardness and elastic modulus, and to compare to crystal lattice axes

10.2 Accomplishments

- Optimized a tape-casting process that can create a dense, uniform microstructure of highly oriented grains

- Determined the relationship between processing parameters, such as shear and solids loading, and fired grain-orientation in boron carbide

- Develop a hot-pressing protocol using carbon as a sintering aid to produce 99+% dense boron carbide

10.3 Introduction

Boron carbide is widely used as an armor material. However, its use under high-impact loading is limited because it undergoes a pressure-induced phase transformation, which is believed to be due to the creation of an amorphous phase during failure. There has been no conclusive proof for an explanation of the origin or mechanism of formation of the amorphous phase (*1*). One possible explanation is this amorphous phase is caused by the substantial modulus anisotropy that exists in boron carbide grains, and it is responsible for low ballistic performance caused by increased intergranular fracture. By orienting the grains within a microstructure, the elastic mismatch between grains would be reduced. This is expected to increase the fracture toughness of the textured body, especially when the stress is applied along specific planes of interest in the body. Nycz and Haber (*2*) have shown that controlled-shear processing can induce texture in

92

slightly anisotropic alumina bodies, as shown in figure 54 (*3*). Hot-pressing has also been shown to induce texture in bodies, as grains orient perpendicular to the applied pressure during sintering. Therefore, hot-pressing of 10-μm powder obtained from UK Abrasives, Inc. (figure 55) was initiated with the goal of determining a protocol for pressing dense samples. Tape-casting parameters were researched, and because there was a minimum of prior work in tape-casting of boron carbide, a series of experiments was established to determine ideal tape composition and casting.
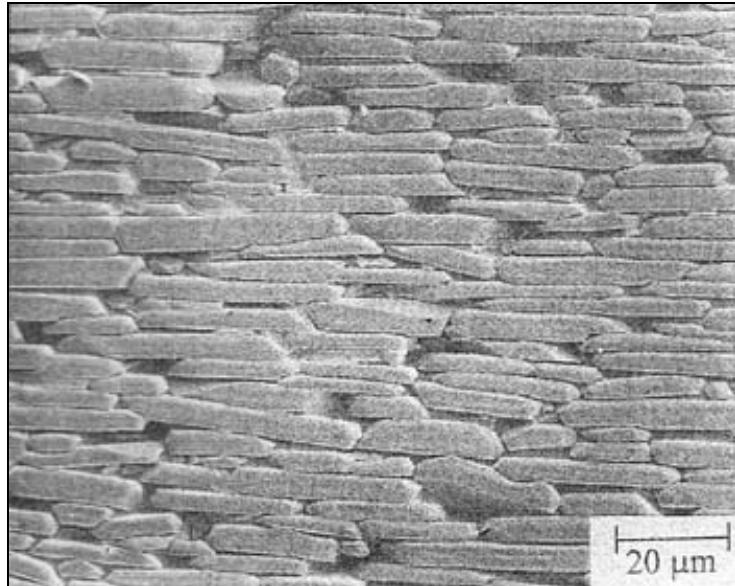

Figure 54. Example of a highly textured alumina microstructure (*3*).

10.4 Accomplishments

Though this project had limited research time, it focused on casting of boron carbide and optimizing a hot-pressing protocol. Upon successive casts at varying compositions, an ideal working composition of 70.5% ceramic, 1.5% carbon sintering aid, 4.5% dispersant, and 23.5% binder/plasticizer was selected, and a 50% solids loading was used for casting. The tapes were formulated by mixing the ceramic, sinter aid, and dispersant in deionized water on a ball mill for 24 hr. At this point, the binder was added, and the slip was milled for another hour before casting at 7.3 cm/s. After casting, tapes were laminated into monoliths approximately 1 in thick by pressing at 96 MPa in a dry press, and the binder was removed by heating to 450 °C. When hot-pressing samples, the press was operated successfully for samples at 38 MPa at varying temperatures in an attempt to achieve theoretical density. Runs at 2000 °C resulted in pieces of 90% theoretical density. Samples were then pressed at 38 MPa and temperatures of 2050 °C and 2075 °C. The samples pressed at 2050 °C resulted in densities of approximately 96% of theoretical density, and those pressed at 2075 were 98% of theoretical density.

To study the effect of hold time at temperature, samples were then pressed at 2075 °C. Two samples were produced at 2075 °C, one with a hold time of 15 min and the other with a hold time of 1 hr. When density measurements were taken, the sample held at temperature for
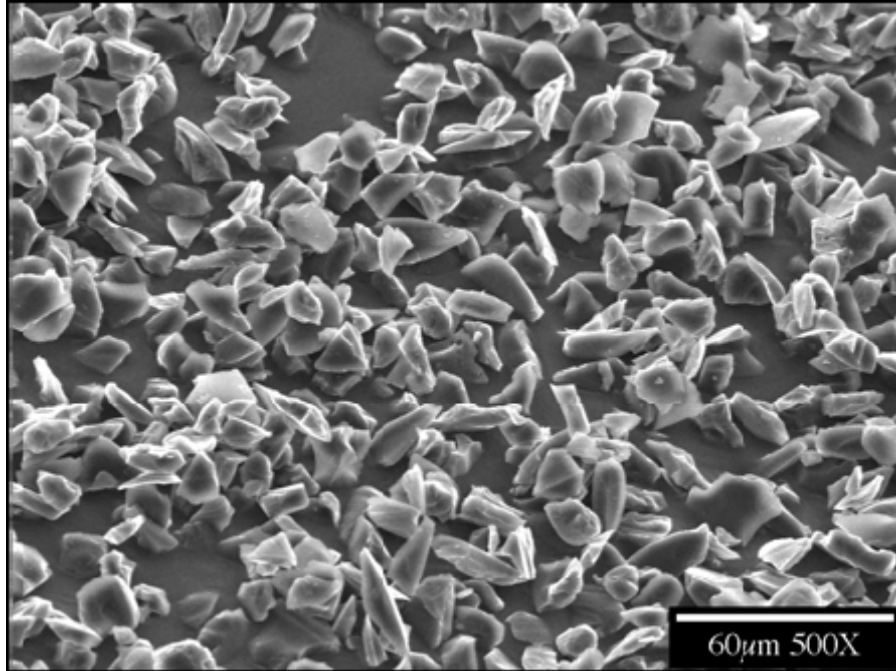
Figure 55. SEM micrograph of boron carbide showing platy morphology
(courtesy of UK abrasives).

1 hr had a slightly higher density, but when it was examined under optical microscopy after polishing, it exhibited a much greater degree of surface porosity than the sample held at temperature for 15 min. This difference in porosity was attributed to the presence of free graphite in the sample—present through the excess carbon in the original working powder and the additive Huntsman surfactant additive. This excess graphite would have been pulled out from the sample during grinding and polishing, resulting in the porosity seen when optically examined. The porosity also adversely affected hardness data taken on samples of hot-pressed powder created to assist in determining pressing protocols. Determining indent size was made difficult by the great degree of porosity present upon polished sections from surface and interior faces of the sample. These samples exhibited Knoop hardness values (at a 0.1-kg load) two orders of magnitude below values normally experienced in dense parts. In recent communications with Dr. McCuiston of ARL, these densification problems were discussed, and a new composition and firing cycle were selected for hot-pressing.

Tape-cast samples were examined for induced texture. Several methods for evaluating texture exist, including x-ray diffraction through the Lotgering method (4), rocking curves/pole figures, neutron diffraction, and optical transmission. It has been shown that when polarized light is transmitted through a textured anisotropic material, the resulting birefringence in the sample will cause a change in transmitted light under cross-polarization. Because optical methods have greater sensitivity than x-ray diffraction, the optical technique was selected to determine if texture was induced in the tapes. Because boron carbide scatters light strongly, samples had to be mounted on optical slides and polished to an appropriate thickness. When examined under

optical microscopy (figure 56), the samples exhibited a change in intensity of transmitted light indicative of textured anisotropic crystals. Since texture was observed in the tapes, it is now possible to use x-ray diffraction to assess more quickly the texture induced in the tapes.
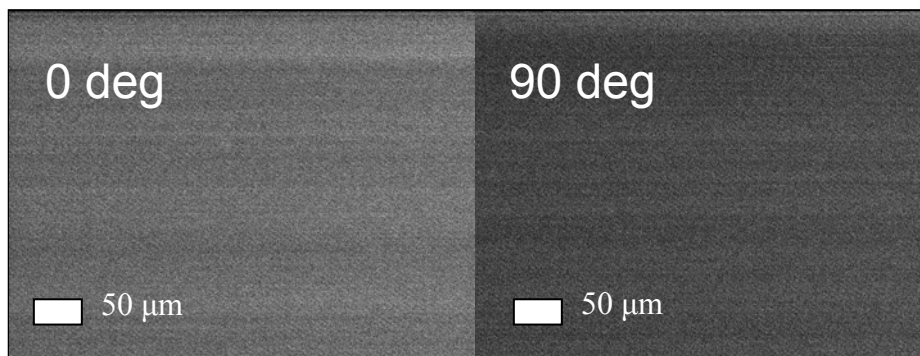

Figure 56. Optical micrographs of tape-cast samples showing variance in transmitted light upon polarization of incident light.

Hot-pressed samples were also examined by Raman spectroscopy. Figure 57 displays the intensity patterns obtained using a 785-nm incident beam. These patterns depict a fairly clean boron-carbide pattern with disorder peaks around 300 cm^{-1}. The cause of disorder and what information can be obtained from the disorder peaks have yet to be fully identified. The Raman spectra show a small but noticeable amount of free carbon present in the sample, with D and G peaks for carbon present at 1300 and 1600 cm^{-1}, respectively, shown in figure 57c. The relative intensities of the D and G peaks are slightly stronger when the sample is examined perpendicular to the direction of hot-pressing than when examined parallel to the hot-pressing direction. As graphite tends to have a stronger Raman signal when vibrating in plane, the stronger relative intensities show that the excess carbon in the sample experienced some alignment perpendicular to the direction of hot-pressing. Similarly, the boron-carbide spectra itself were slightly stronger perpendicular to the direction of hot-pressing than parallel to the direction of hot-pressing, showing alignment of grains of the boron carbide merely from the press. This is encouraging as it can be used to predict that hot-pressing of tape-cast samples will merely reinforce the texture induced through the shear of casting.

10.5 Future Studies

Now that texture has been shown in the samples, x-ray diffraction studies utilizing the Lotgering method and rocking curves can be employed to show quickly texture in tape-cast samples. Reduction of carbon additive will make adjustments to excess carbon content. The level of free carbon present in the manufacturer's powder will be analyzed to compare with other commercially available powders and determine if there is enough to influence sintering so as to produce the degree of free carbon observed in the hot-pressed sample. Aluminum, administered as a powder (aluminum nitride or aluminum oxide), may be investigated as a sintering aid to help
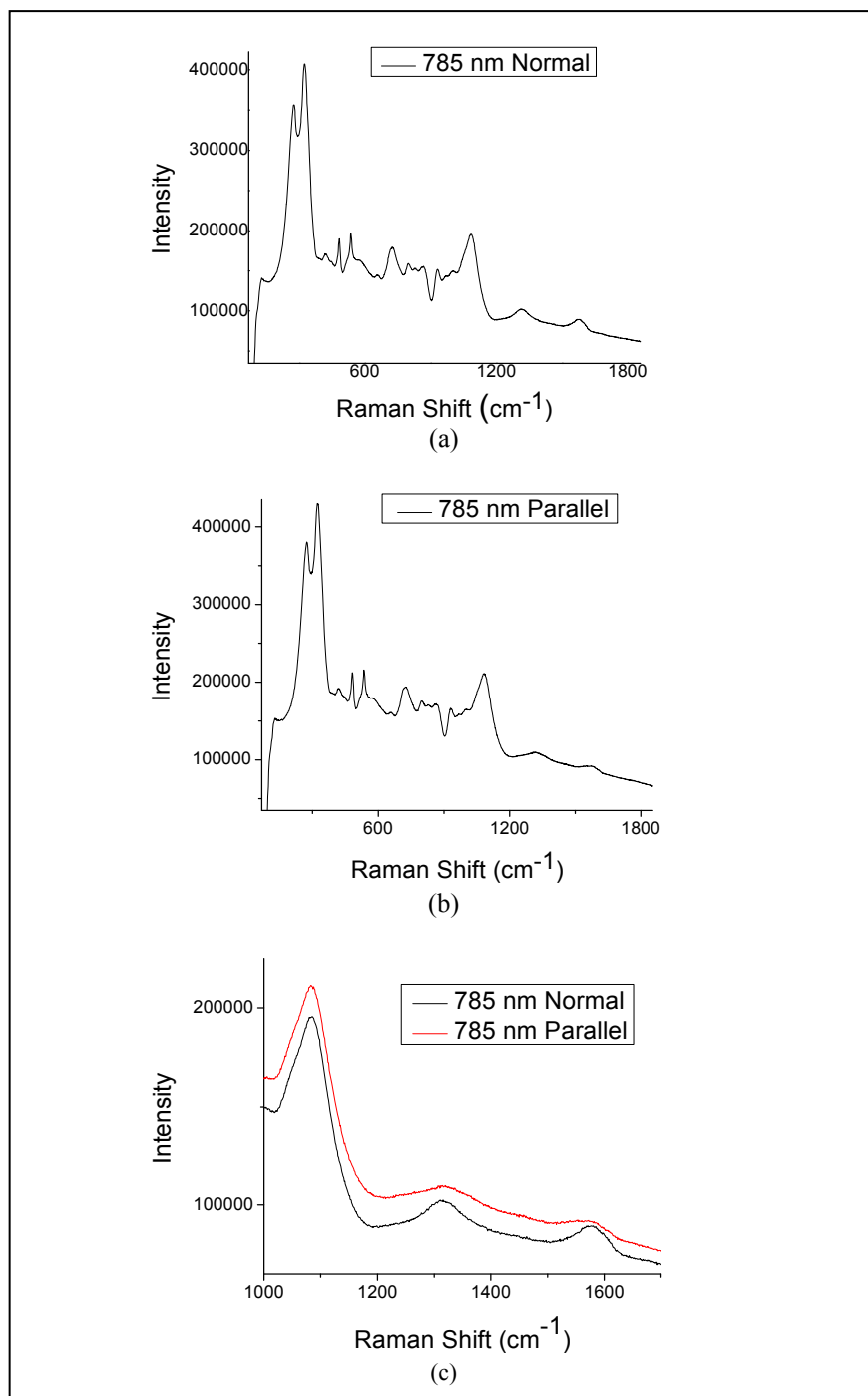
Figure 57. Raman spectra for hot-pressed boron carbide (a) perpendicular to the
direction of hot-pressing, (b) parallel to the direction of hot-pressing,
and (c) the free carbon peaks compared between directions of study.

obtain theoretical density. Once a dense, carbon-free textured sample is obtained, hardness will be taken parallel and perpendicular to the axis of casting and pressing. Elastic modulus will be calculated through ultrasonic analysis of samples upon the two aforementioned axes, and samples will be submitted to ARL for ballistic testing. Possible future work also includes examining the effect of hot-pressing powdered boron carbide with a textured tape present at the edges of the sample to template grain growth preferentially.

10.6 References

1. Chen, M.; McCauley, J.; Hemker, K. Shock-Induced Localized Amorphization in Boron Carbide. *Science* **2003**, *299*, 1563.

2. Nycz, S.; Haber, R. Controlling Microstructural Anisotropy During Forming. *Ceramic Engineering and Science Proceedings*, submitted for publication, 2005.

3. Seabaugh, M. M.; Kerscht, I. H.; Messing, G. L. Texture Development by Templated Grain Growth in Liquid-Phase-Sintered a-Alumina. *J. Am. Ceram. Soc.* **1997**, *80* (5), 1181–1188.

4. Lotgering, F. K. Topotactical Reactions With Ferrimagnetic Oxides Having Hexagonal Crystal. *J. Inorg. Nucl. Chem* **1959**, (9), 113–123.

11. Education and Outreach

11.1 Objectives

- Education Components— as determined

- Outreach Component—national and international activities

11.2 Key Accomplishments

- Established a CAWG involving over 20 member organizations

- Conducted five armor research projects, selected by member organizations, three of which were jointly funded by the MCOE

- Linked ARL researchers with university researchers

- Supported six graduate student and two post-doctoral associate research projects

- Twenty-nine publications and 44 presentations were generated by the research

11.3 Accomplishments

A very successful CAWG was established. The group was set up within the CCMC, an NSF Industry/University Cooperative Research Center, with three purposes:

- To establish a forum for the ceramic armor community to hold workshops on topics selected by the member organizations as the most relevant for improving their mutual understanding of key issues in ceramic armor materials

- To conduct precompetitive research on ceramic armor materials that is selected by the member organizations as the most relevant research needed to improve the fundamental understanding of the relation of ceramic armor materials science to armor performance

- To provide a mechanism to distribute quickly the results of the MCOE to the ceramic armor community

This CAWG has grown to over 20 member organizations, and nine very productive workshops were held. The organizations that participated in the CAWG during the 5-year period of this investigation were:

Alanx, ARL, Ceradyne, Cercom, CoorsTek, Harrop, Dow Chemical, Honeywell, Kennametal, M-Cubed, Northwest Metttech, MER, Microabrasives, Natick, NIST, Picatinny Arsenal, PPG Industries, Protective Materials Inc., Saint Gobain, Simula, Spinks Clay Co., Superior Graphite, TARDEC, United Technology, UK Abrasives, Ultran Laboratories, and Umicore.

The CAWG supported five ceramic armor research projects, three of which were jointly funded by the MCOE. The jointly funded projects were NDE of Ceramic Armor, Directionally Textured Boron Carbide by Controlled Shear and Relation of Quasi-Static Properties to Ballistic Performance of Armor Ceramics. These projects are described elsewhere in this report. One of the projects funded entirely by the CAWG investigated the effect of low levels of porosity and its associated pore distribution on armor performance. This research showed that the hardness variability for armor materials that are over 95% dense is related to the porosity in the area of the hardness indent. This hardness variability may be related to the variability in ballistic performance results. The other project funded entirely by the CAWG investigated the fundamental reason for the change in ballistic performance of B_4C above a threshold impact pressure. This project focused on understanding the root cause for the development of amorphous planes in B_4C above the threshold pressure, as reported by Chen et al. (*1*). This research identified the B_4C polytype with C-C-C chains as the probable cause of the threshold pressure, since this polytype has much lower activation energy for collapse into B_{12} and amorphous carbon than the polytype with C-B-C chains. Ab initio calculations showed that the C-C-C polytype becomes metastable at 7 GPa, and the C-B-C polytypes do not become metastable until above 40 GPa. The C-C-C polytype is a minor polytype in hot-pressed B_4C, which points a direction for improving the ballistic performance of B_4C.

In addition, the MCOE has linked ARL researchers with the researchers at Rutgers and Johns Hopkins. At Rutgers, three graduate students completed Ph.D.s with ARL researchers being outside thesis advisors. Four additional students are completing their Ph.D. studies with ARL researchers as thesis committee members for each of these students. This collaboration has extended to the CAWG where the two graduate students currently working on ceramic armor programs have ARL researchers on their thesis committees, and the two postdoctoral fellows have ARL scientists in their technical advisory groups. Twenty-nine publications (five joint presentations with ARL researchers), one patent, and 44 presentations (10 joint presentations with ARL researchers) have resulted from this program. Six students have held summer internships, and Professor Niesz spent a 6-month sabbatical at ARL, further contributing to the joint collaboration.

11.4 Reference

1. Chen, M.; McCauley, J.; Hemker, K. Shock-Induced Localized Amophization in Boron Carbide. *Science* **2003**, 299, 1563–1566.

12. Publications From the Program

12.1 Written Publications

The following are the 29 written publications from the program:

1. McCuiston, R. C.; Danforth, S. C.; Niesz, D. E. Processing and Characterization of Al_2O_3 and Al_2O_3/Cu Alloy Composites. Published in *Mat. Res. Soc. Symp. Proc.*, MRS Fall 2001; Vol. 698.

2. Molinari, J.-F.; Zhou, F. 3-D Finite Element Analysis of Impact Damage in Metallic and Ceramic Targets. *Ceramic Armor Materials by Design, Ceramic Transactions* **2002**, *134*, 317–328.

3. Jiang, B.; Weng, G. J. A Composite Model for the Grain-Size Dependence of Yield Stress of Nano-Grained Materials. *Metallurgical and Materials Transactions* **2003**, *34A*, 765–772.

4. Jiang, B.; Weng, G. J. A Theory of Compressive Yield Strength of Nano-Grained Ceramics. *International Journal of Plasticity* **2004**, *20*, 2007–2026.

5. Jiang, B.; Weng, G. J. A Generalized Self-Consistent Polycrystal Model for the Yield Strength of Nanocrystalline Materials. *Journal of the Mechanics and Physics of Solids* **2004**, *52*, 1125–1149.

6. Chen, M.; McCauley, J. W.; Hemker, K. J. Shock-Induced Localized Amorphization in Boron Carbide. *Science* **2003**, *299*, 1563–1566.

7. Bakas, M.; Niesz, D. E.; Greenhut, V. A.; Adams, J.; McCauley, J. Relationship Between Defects and Dynamic Failure in Silicon Carbide. *Ceram. Eng. and Sci. Proc.* **2003**, *24* (3), 351–358.

8. Zhou, F.; Molinari, J.-F. Three Dimensional Dynamic Crack Propagation Using Cohesive Elements: A Methodology to Address Mesh Dependency. *International Journal for Numerical Methods in Engineering* **2004**, *59* (1), 1–24.

9. Wang, H.; Ramesh, K. T. Dynamic Strength and Fragmentation of Hot-Pressed Silicon Carbide Under Uniaxial Compression. *Acta Materialia* **2004**, *52*, 355–367.

10. Hu, N.; Molinari, J.-F. Shear Bands in Dense Metallic Granular Materials. *Journal of Mechanics and Physics of Solids* **2004**, *52*, 499–531.

11. Zhou, F.; Molinari, J.-F. Stochastic Fracture of Ceramics under Dynamic Tensile Loading. *International Journal of Solids and Structures* **2004**, *41*, 6573–6596.

12. Jiao, T.; Li, Y.; Ramesh, K. T.; Wereszczak, A. High Rate Response and Dynamic Failure of Structural Ceramics. *International Journal of Applied Ceramic Technology* **2004**, *1* (3), 243–253.

13. Zhou, F.; Molinari, J.-F. On The Rate-Dependency of Dynamic Tensile Strength of a Model Ceramic System. *Computer Methods in Applied Mechanics and Engineering* **2005** *194* (12–16), 1693–1709.

14. Zhou, F.; Molinari, J.-F.; Shioya, T. A Rate-Dependent Cohesive Model for Simulating Dynamic Crack Propagation in Brittle Materials. *Engineering Fracture Mechanics* **2005**, *72* (9), 1383–1410.

15. Zhou, F.; Molinari, J.-F.; Ramesh, K. T. A Cohesive-Model Based Fragmentation Analysis: Effects of Strain Rate and Initial Defects Distribution. *International Journal of Solids and Structures*, in press, 2005.

16. Zhou, F.; Molinari, J.-F.; Ramesh, K. T. Effects of Material Properties and Strain Rate on the Fragmentation of Brittle Materials. *Journal of the Mechanics and Physics of Solids*, submitted for publication, 2005.

17. Zhou, F.; Ramesh, K. T.; Molinari, J.-F. Characteristic Fragment Size Distribution of Dynamically Expanding Rings. *Physical Review Letters*, submitted for publication, 2005.

18. McEnerney, B. W.; Quinn, G.; Greenhut, V. A.; Sadangi, R. K.; Shukla, V.; Kear, B.; Niesz, D. E. Processing and Hardness of an Al_2O_3-$MgAl_2O_4$ Nanocomposite. *Cer. Sci. and Eng. Proc.*, in press, 2004.

19. Bakas, M. P.; Greenhut, V. A.; Niesz, D. E.; Quinn, G. D.; McCauley, J. W.; Wereszczak, A. A.; Swab, J. J. Anomalous Defects and Dynamic Failure of Armor Ceramics. *International Journal of Applied Ceramic Technology* **2004**, *1* (3), 211–18.

20. McCuiston, R. C.; Danforth, S. C.; Matthewson, M. J.; Niesz, D. E. Solid Freeform Fabrication of Advanced Armor Concepts: Opportunities for Design and Manufacture. *Ceramic Armor Materials by Design*, *Ceramic Transactions*; McCauley, J. W., Crowson, A., Gooch, W. A., Jr., Rajendran, A. M., Bless, S. J., Logan, K. V., Normandia, M., Wax, S., Eds. **2002**, *134*, 473–481. (Subsequently republished in *Progress in Ceramic Armor*, American Ceramic Society, 2004.)

21. Brennan, R.; Haber, R.; Niesz, D.; McCauley, J.; Bhardwaj, M. Non-Destructive Evaluation (NDE) of Ceramic Armor: Fundamentals. *Proceedings of the 29th International Conference and Exposition on Advanced Ceramics and Composites*; submitted January 2005.

22. Brennan, R.; Haber, R.; Niesz, D.; McCauley, J. Non-Destructive Evaluation (NDE) of Ceramic Armor: Testing. *Proceedings of the 29th International Conference and Exposition on Advanced Ceramics and Composites*; submitted January 2005.

23. Chen, M. W.; McCauley, J. W.; LaSalvia, J. C.; Hemker, K. J. Microstructural Characterization of Commercial Hot-Pressed Boron Carbide Ceramics. *Journal of the American Ceramic Society* **2005**, *8* (7), 1935–1942.

24. Chen, M. W.; McCauley, J. W. Synthesis of Boron Nitride Nanowires by Mechanical Scratching. *Journal of Applied Physics* **2006**, *100*, 123517.

25. Chen, M.; McCauley, J. W.; Dandekar, D. P.; Bourne, N. K. Plastic Deformation and Fracture of Brittle Ceramic Under Shock Loading; in preparation.

26. Zhou, F.; Molinari, J.-F.; Ramesh, K. T. A Finite Difference Analysis of the Brittle Fragmentation of an Expanding Ring. *Computational Material Sciences*, submitted for publication, 2005.

27. Brennan, R.; Haber, R.; Niesz, D.; McCauley, J.; Bhardwaj, M. Defect Engineering of Samples for Non-Destructive Evaluation (NDE) Ultrasound Testing. *The 107th Annual Meeting of the American Ceramic Society*, Baltimore, MD, 11 April 2005.

28. Ziccardi, C.; Gonzalez, N.; Haber, R.; Niesz, D.; McCauley, J. Determining Effect of Anomalous Defects on SiC Armor. *The 29th Annual Cocoa Beach Conference on Advanced Ceramics and Composites*, Cocoa Beach, FL, January 2005.

29. Demirbas, M. V.; Haber, R. A. Defining Microstructural Tolerance Limits of Defects for SiC Armor. *Proceedings of the 107th Annual Meeting and Exposition of the American Ceramic Society*, Baltimore, MD, submitted April 2005.

12.2 Oral Presentations

The following are the 44 presentations from the program:

1. Molinari, J.-F.; Zhou, F. 3D Finite Element Analysis of Impact Damage in Metallic and Ceramic Targets, Ceramic Armor Materials by Design Symposium, PAC RIM IV, 5–7 November 2001.

2. McCuiston, R. C.; Danforth, S. C.; Niesz, D. E. Processing and Characterization of Al_2O_3 and Al_2O_3/Cu Alloy Composites; Materials Research Society: Boston, MA, 2001.

3. McCuiston, R. C.; Danforth, S. C.; Matthewson, M. J.; Niesz , D. E. Solid Freeform Fabrication of Advanced Armor Concepts: Opportunities for Design and Manufacture. PAC RIM IV, 2001.

4. Zhou, F.; Molinari, J.-F. Numerical Simulations of Dynamic Fracture Process in Brittle Materials. 14th US National Congress of Theoretical and Applied Mechanics, Blacksburg, VA, 23–28 June 2002.

5. Zhou, F.; Molinari, J.-F. 3D Simulations for Dynamic Crack Propagation in Brittle Materials Using Rate Dependent Cohesive Models. *Society of Engineering Science Conference*, Penn State University: Philadelphia, PA, 15 October 2002.

6. McEnerney, B. W.; Sadangi, R. K.; Shukla, V.; Niesz, D. E.; Kear, B. H. Fabrication of Dense Al_2O_3 - $MgAl_2O_4$ Nanocomposites, *The 6th International Conference on Nanostructured Materials*, Orlando, FL, 2002.

7. Zhou, F.; Jiao, T.; Wang, H.; Molinari, J.-F.; Ramesh, K. T. Mechanical Behavior of Ceramics Under Impact Loading, *ASME Winter Meeting*, New Orleans, LA, 22 November 2002.

8. Chen, M. W.; McCauley, J. W.; Hemker, K. J. Microstructural Characterization of Hot-Pressed Boron Carbide. *Presented at TMS fall meeting*, Cincinnati, OH, 2002.

9. Zhou , F.; Molinari, J.-F. Numerical Investigation of Dynamic Compressive Loading. American Ceramics Society Cocoa Beach Meeting, Cocoa Beach, FL, 2002.

10. Molinari, J.-F. Numerical Simulations of Dynamic Crack Propagation. Invited Seminar; U.S. Army Research Laboratory: Aberdeen Proving Ground, MD, 6 June 2002.

11. Molinari, J.-F. Understanding Failure: Numerical Simulations of Dynamic Crack Propagation. Invited Seminar, Civil Engineering Department, Johns Hopkins University: Baltimore, MD, 9 March 2002.

12. McEnerney, B. W.; Sadangi, R. K.; Shukla, V.; Kear, B. H.; Niesz, D. E. Mechanical Behavior of Nanocomposite Structure. *The 105th Annual Meeting of the American Ceramic Society*, Nashville, TN, 2003.

13. McCuiston, R. C.; Danforth, S. C.; Niesz, D. E. Fabrication of Al_2O_3/WC-Co Macrostructured Composites. *The 105th Annual Meeting of the American Ceramic Society*, Nashville, TN, 2003.

14. Bakas, M.; Niesz, D. E.; Greenhut, V. A.; Adams, J.; McCauley, J. Relationship Between Defects and Dynamic Failure in Silicon Carbide. *The 105th Annual Meeting of the American Ceramic Society*, Nashville, TN, 2003.

15. McEnerney, B. W.; Sadangi, R. K.; Shukla, V.; Niesz, D. E.; Kear, B. H. Nanocomposite Materials for High-Strain Rate Applications. *The 27th Annual Cocoa Beach Conference and Exhibition on Advanced Ceramics and Composites*, Cocoa Beach, FL, 2003.

16. McCuiston, R. C.; Niesz, D. E.; Danforth, S. C. Fabrication of Al_2O_3 Containing Randomly and Periodically Placed WC-Co Inclusions. *The 27th Annual Cocoa Beach Conference and Exhibition on Advanced Ceramics and Composites*, Cocoa Beach, FL, 2003.

17. Chen, M. W.; McCauley, J. W.; Hemker, K. J. Shock Induced Nanoscaled Amorphization of Boron Carbide. *The 27th Annual International Conference and Exposition on Advanced Ceramics and Composites*, Cocoa Beach, FL, 2003.

18. Bakas, M.; Niesz, D. E.; Greenhut, V. A.; Adams, J.; McCauley, J. Relationship Between Defects and Dynamic Failure in Silicon Carbide. 27th Annual Cocoa Beach Conference and Exhibition on Advanced Ceramics and Composites, Cocoa Beach, FL, 2003.

19. Chen, M.; McCauley, J. W.; Hemker, K. J. Recent TEM Characterization of Boron Carbide. Presented at Boron Carbide Workshop, Rutgers University: Trenton, NJ, January 2003.

20. Ramesh, K. T. *The High Strain Rate Response of Engineering and Armor Ceramics*. Beijing Institute of Technology: Beijing, China, 14 October 2003.

21. Zhou, F.; Molinari, J.-F.; Ramesh, K. T. Fragmentation of a Dynamically Expanding Brittle Ring. Presented at the SES Annual Meeting, Lincoln, NE, 2004.

22. Zhou, F.; Molinari, J.-F.; Ramesh, K. T. The Dynamic Fragmentation of Brittle Materials. Presented at the *International Workshop on Computational Mechanics of Materials*, Goa, India, 2004.

23. McEnerney, B. W.; Sadangi, R. K.; Shukla, V.; Kear, B. H.; Niesz, D. E. Mechanical Behavior of Nanocomposite Ceramic Structures. The *7th International Conference on Nanostructured Materials*, Wiesbaden, Germany, 2004.

24. McCuiston, R. C.; Molinari, J.-F.; Niesz, D. E.; Danforth, S. C. Fabrication and Computer Simulation of Al_2O_3/WC-Co Macrostructures. Annual Meeting of the American Ceramic Society, Indianapolis, IN, 2004.

25. McEnerney, B. W.; Sadangi, R. K.; Shukla, V.; Kear, B. H.; Niesz, D. E. Behavior of Dense Nanocomposite Structures. *The 28th Annual Cocoa Beach Conference and Exhibition on Advanced Ceramics and Composites*, Cocoa Beach, FL, 2004.

26. McCuiston, R. C.; Molinari, J.-F.; Niesz, D. E.; Danforth, S. C. Fabrication and Modeling of Al_2O_3/WC-Co Macrostructures. *The 28th Annual Cocoa Beach Conference and Exhibition on Advanced Ceramics and Composites*, Cocoa Beach, FL, 2004.

27. Zhou, F.; Molinari, J.-F.; Ramesh, K. T. Dynamic Fragmentation Investigation: Strain Rate Effects on Fragment Size and Fragment Size Distributions. *The 28th Annual Cocoa Beach Conference and Exposition*, Cocoa Beach, FL, 25–30 January 2004.

104

28. Bakas, M.; Greenhut, V. A.; Niesz, D. E.; Adams, J.; LaSalvia, J.; McCauley, J.; Quinn, G. Identification of Fundamental Dynamic Failure Mechanisms in Armor Ceramics. *The 28th International Conference on Advanced Ceramics and Composites*, Cocoa Beach, FL, 2004.

29. Brennan, R.; Haber, R.; Niesz, D.; McCauley, J.; Bhardwaj, M. Defect Engineering of Samples for Non-Destructive Evaluation (NDE) Ultrasound Testing. *The 107th Annual Meeting of the American Ceramic Society*, Baltimore, MD, 11 April 2005.

30. Bakas, M. P.; Greenhut, V. A.; Niesz, D. E.; Quinn, G. D.; Wereszczak, A. A.; McCauley, J. W.; Swab, J. J. Analysis of Defect Populations in Silicon Carbide Ballistic Test Targets. *American Ceramic Society 29th Annual Conference on Advanced Ceramics and Composites*, Coca Beach, FL, January 2005.

31. McEnerney, B. W.; Sadangi, R. K.; Paliwal, B. S.; Shukla, V.; Ramesh, K. T.; Greenhut, V. A.; Kear, B. H.; Niesz, D. E. Mechanical Behavior of Al_2O_3 - $MgAl_2O_4$ Nanocomposites. *The 29th Annual Cocoa Beach Conference and Exhibition on Advanced Ceramics and Composites*, Cocoa Beach, FL, January 2005.

32. Ziccardi, C.; Demirbas, M. V.; Haber, R. A.; Niesz, D. E.; McCauley, J. Means of Using Advance Processing to Eliminate Anomalous Defects on SiC Armor. *American Ceramic Society 29th International Conference on Advanced Ceramics and Composites*, Cocoa Beach, FL, January 2005.

33. McCuiston, R.; Azriel, E.; Sadangi, R.; Danforth, S.; Haber, R.; Niesz, D.; Molinari, J.-F. Fabrication and Simulation of Random and Periodic Macrostructures. *The 29th Annual Cocoa Beach Conference and Exhibition on Advanced Ceramics and Composites*, Cocoa Beach, FL, January 2005.

34. Brennan, R.; Haber, R.; Niesz, D.; McCauley, J.; Bhardwaj, M. Non-Destructive Evaluation (NDE) of Ceramic Armor: Fundamentals. *The 29th International Conference and Exposition on Advanced Ceramics and Composites*, Cocoa Beach, FL, January 2005.

35. Paliwal, B.; Ramesh, K. T.; McCauley, J. W.; Patel, P. Dynamic Failure of AlON Under Uniaxial Compression. *The 29th International Conference and Exposition on Advanced Ceramics and Composites*, Cocoa Beach, FL, January 2005.

36. Chen, M.; Bourne, N. K.; Dandekar, D. P.; McCauley, J. W. Microstructural Characterization of Shock Recovered AD 995 Alumina. *The 29th International Conference and Exposition on Advanced Ceramics and Composites*, Cocoa Beach, FL, January 2005.

37. Chhowalla, M.; McCauley, J. W.; Niesz, D. E. Review of Available Literature on Boron Carbide. *The 29th International Conference and Exposition on Advanced Ceramics and Composites*, Cocoa Beach, FL, January 2005.

38. Brennan, R.; Haber, R.; Niesz, D.; McCauley, J. Non-Destructive Evaluation (NDE) of Ceramic Armor Materials. *The 107th Annual Meeting and Exposition of the American Ceramic Society*, Baltimore, MD, 11–13 April 2005.

39. Chen, M.; Vogler, T. J.; Ding, Y.; McCauley, J. W. Importance of Dynamic Loading on the Amorphization of Boron Carbide. *The 107th Annual Meeting and Exposition of the American Ceramic Society*, Baltimore, MD, 11–13 April 2005.

40. Paliwal, B.; Ramesh, K. T.; McCauley, J. W.; Patel, P. Dynamic Failure of AlON under Uniaxial and Biaxial Compression. *The 107th Annual Meeting and Exposition of the American Ceramic Society*, Baltimore, MD, 11–13 April 2005.

41. Chen, M.; Bourne, N. K.; McCauley, J. W.; Dandekar, D. P. Microstructural Characterization of Shock Recovered AD995 Alumina, APS, 2005 Meeting, Baltimore, MD, 1–5 August 2005.

42. McEnerney, B. W.; Sadangi, R. K.; Shukla, W.; Kear, B. E.; Niesz, D. E. Mechanical Behavior of Al_2O_3 - $MgAl_2O_4$ Nanocomposites. PAC RIM VI: A World of Science and Technology, Maui, HI, 2005.

43. Kaza, A.; Matthewson, J. M.; Niesz, D. E. Removal of SiO2 from Green SiC Compacts. *The 106th Annual Meeting, American Ceramic Society*, Indianapolis, IN, 2004.

44. Demirbas, M. V.; Haber, R. A. Defining Microstructural Tolerance Limits of Defects for SiC Armor. *The 107th Annual Meeting and Exposition of the American Ceramic Society*. Baltimore, MD, 11–13 April 2005.

12.3 Patents

The following is the patent from the program:

1. Kear, B. H.; McEnerney, B.; Niesz, D. E.; Sadangi, R. K. Nanocomposite Ceramic Armor and Method for Production of Same. Registration no. 48,897, provisional patent application filed, 11 April 2005.

12.4 Theses

The following are the theses from the program:

1. McEnerney, B. W. On the Fabrication of Al_2O_3-$MgAl_2O_4$ Nanocomposites Produced from Metastable Feedstock Material. Ph.D. Thesis. Rutgers, The State University of New Jersey, Piscataway, NJ, May 2005.

2. McCuiston, R. C. Fabrication and Simulation of Random and Periodic Composites for Reduced Stress Wave Propagation. Ph. D. Thesis. Rutgers, The State University of New Jersey, Piscataway, NJ, October 2005.

3. Bakas, M. P. Analysis of Inclusion Distributions in Silicon Carbide Armor Ceramics. Ph.D. Thesis. Rutgers, The State University of New Jersey, Piscataway, NJ, October 2005.

1   COMMANDER
US ARMY MATERIEL CMD
AMXMI INT
9301 CHAPEK RD
FT BELVOIR VA 22060-5527

1   COMMANDER
US ARMY TACOM
PM HBCT
SFAE GCS HBCT S (MS 506)
6501 ELEVEN MILE RD
WARREN MI 48397-5000

1   COMMANDER
US ARMY TACOM
AMSTA SF
WARREN MI 48397-5000

1   OFC OF NAVAL RSRCH
J CHRISTODOULOU
ONR CODE 332
800 N QUINCY ST
ARLINGTON VA 22217-5600

1   COMMANDER
US ARMY TACOM
PM SURVIVABLE SYSTEMS
SFAE GCSS W GSI H
M RYZYI
6501 ELEVEN MILE RD
WARREN MI 48397-5000

1   COMMANDER
US ARMY TACOM
CHIEF ABRAMS TESTING
SFAE GCSS W AB QT
J MORAN
6501 ELEVEN MILE RD
WARREN MI 48397-5000

1   COMMANDER
WATERVLIET ARSENAL
SMCWV QAE Q
B VANINA
BLDG 44
WATERVLIET NY 12189-4050

2   HQ SFSJM CDL
US ARMY JOINT MUNITIONS CMD
AMSIO SMT
R CRAWFORD
W HARRIS
1 ROCK ISLAND ARSENAL
ROCK ISLAND IL 61299-6000

2   COMMANDER
US ARMY AMCOM
AVIATION APPLIED TECH DIR
J SCHUCK
FT EUSTIS VA 23604-5577

1   NAVAL SURFACE WARFARE CTR
DAHLGREN DIV CODE G06
DAHLGREN VA 22448

1   USA SBCCOM PM SOLDIER SPT
AMSSB PM RSS A
J CONNORS
KANSAS ST
NATICK MA 01760-5057

3   AIR FORCE ARMAMENT LAB
AFATL DLJW
W COOK
D BELK
J FOSTER
EGLIN AFB FL 32542

3   DPTY ASSIST SCY FOR R&T
SARD TT
ASA (ACT)
C CHABALOWSKI
T KILLION
J PARMENTOLA
THE PENTAGON RM 3E479
WASHINGTON DC 20310-0103

2   DARPA
W COBLENZ
L CHRISTODOULOU
3701 N FAIRFAX DR
ARLINGTON VA 22203-1714

1   DIRECTOR
US ARMY ARDEC
AMSRD AAR AEE W
E BAKER
BLDG 3022
PICATINNY ARSENAL NJ
07806-5000

110

1	SAIC J FURLONG MS 264 1710 GOODRIDGE DR MCLEAN VA 22102
2	SIMULA INC V HORVATICH V KELSEY 10016 51ST ST PHOENIX AZ 85044
3	UNITED DEFENSE LP E BRADY R JENKINS J JOHNSON PO BOX 15512 YORK PA 17405-1512
1	CERADYNE INC ARMOR DEVELOPMENT M NORMANDIA 3169 REDHILL AVE COSTA MESA CA 92626

ABERDEEN PROVING GROUND

75 DIR USARL
    AMSRD ARL WM
      S KARNA
      J SMITH
      T WRIGHT
    AMSRD ARL WM B
      M ZOLTOSKI
    AMSRD ARL WM EG
      E SCHMIDT
    AMSRD ARL WM BC
      J NEWILL
    AMSRD ARL WM M
      R DOWDING
      S MCKNIGHT
    AMSRD ARL WM MC
      R SQUILLACIOTI

AMSRD ARL WM MD
  E CHIN (6 CPS)
  G GAZONAS
  J LASALVIA
  J MONTGOMERY
  P PATEL
  J SANDS
AMSRD ARL WM T
  P BAKER
  B BURNS
AMSRD ARL WM TA
  P BARTKOWSKI
  M BURKINS
  W GOOCH
  D HACKBARTH
  T HAVEL
  C HOPPEL
  E HORWATH
  T JONES
  M KEELE
  D KLEPONIS
  H MEYER
  J RUNYEON
  N RUPERT
  D RUSIN
  S SCHOENFELD
AMSRD ARL WM TB
  A GUPTA
AMSRD ARL WM TC
  R COATES
  T FARRAND
  K KIMSEY
  L MAGNESS
  D SCHEFFLER
  R SUMMERS
  W WALTERS
AMSRD ARL WM TD
  T BJERKE
  J CLAYTON
  D DANDEKAR
  M GREENFIELD
  H MEYER
  K IYER
  J MCCAULEY (20 CPS)
  E RAPACKI
  M SCHEIDLER
  S SEGLETES
  T WEERASOORIYA

INTENTIONALLY LEFT BLANK.